



Universiteit
Leiden
The Netherlands

Investigating the impact of metallicity on star formation in the outer galaxy: I. VLT/KMOS survey of young stellar objects in Canis Major

Itrich, D.; Karska, A.; Sewiło, M.; Kristensen, L.E.; Herczeg, G.J.; Ramsay, S.; ... ; Dekaszymankiewicz, B.

Citation

Itrich, D., Karska, A., Sewiło, M., Kristensen, L. E., Herczeg, G. J., Ramsay, S., ... Dekaszymankiewicz, B. (2023). Investigating the impact of metallicity on star formation in the outer galaxy: I. VLT/KMOS survey of young stellar objects in Canis Major. *The Astrophysical Journal Supplement Series*, 267(2). doi:10.3847/1538-4365/acdd55

Version: Publisher's Version
License: [Creative Commons CC BY 4.0 license](https://creativecommons.org/licenses/by/4.0/)
Downloaded from: <https://hdl.handle.net/1887/3719214>

Note: To cite this publication please use the final published version (if applicable).



Investigating the Impact of Metallicity on Star Formation in the Outer Galaxy. I. VLT/KMOS Survey of Young Stellar Objects in Canis Major

Dominika Itrich^{1,2,3} , Agata Karska^{1,4} , Marta Sewiło^{5,6,7} , Lars E. Kristensen⁸ , Gregory J. Herczeg^{9,10} , Suzanne Ramsay², William J. Fischer¹¹ , Benoît Tabone^{12,13} , Will R. M. Rocha¹⁴ , Maciej Koprowski¹ , Ngân Lê¹ , and Beata Deka-Szymankiewicz¹

¹ Institute of Astronomy, Faculty of Physics, Astronomy and Informatics, Nicolaus Copernicus University, Grudziądzka 5, 87-100 Toruń, Poland; agata.karska@umk.pl

² European Southern Observatory, Karl-Schwarzschild-Str. 2, D-85748 Garching bei München, Germany

³ Universitäts-Sternwarte, Ludwig-Maximilians-Universität, Scheinerstrasse 1, D-81679 München, Germany

⁴ Max-Planck-Institut für Radioastronomie, Auf dem Hügel 69, D-53121, Bonn, Germany

⁵ Exoplanets and Stellar Astrophysics Laboratory, NASA Goddard Space Flight Center, Greenbelt, MD 20771, USA

⁶ Center for Research and Exploration in Space Science and Technology, NASA Goddard Space Flight Center, Greenbelt, MD 20771, USA

⁷ Department of Astronomy, University of Maryland, College Park, MD 20742, USA

⁸ Niels Bohr Institute, Centre for Star and Planet Formation, University of Copenhagen, Øster Voldgade 5-7, DK-1350 Copenhagen K, Denmark

⁹ Kavli Institute for Astronomy and Astrophysics, Peking University, Yiheyuan 5, Haidian Qu, 100871 Beijing, People's Republic of China

¹⁰ Department of Astronomy, Peking University, Yiheyuan 5, Haidian Qu, 100871 Beijing, People's Republic of China

¹¹ Space Telescope Science Institute, 3700 San Martin Dr., Baltimore, MD 21218, USA

¹² Leiden Observatory, Leiden University, PO Box 9513, 2300 RA Leiden, The Netherlands

¹³ Institut d'Astrophysique Spatiale, Université Paris-Saclay, CNRS, Bâtiment 121, F-91405 Orsay Cedex, France

¹⁴ Laboratory for Astrophysics, Leiden Observatory, Leiden University, PO Box 9513, 2300 RA Leiden, The Netherlands

Received 2021 December 21; revised 2023 June 7; accepted 2023 June 8; published 2023 August 10

Abstract

The effects of metallicity on the evolution of protoplanetary disks may be studied in the outer Galaxy where the metallicity is lower than in the solar neighborhood. We present the VLT/KMOS integral field spectroscopy in the near-infrared of ~ 120 candidate young stellar objects (YSOs) in the CMa- $\ell 224$ star-forming region located at a Galactocentric distance of 9.1 kpc. We characterize the YSO accretion luminosities and accretion rates using the hydrogen Br γ emission and find a median accretion luminosity of $\log(L_{\text{acc}}) = -0.82^{+0.80}_{-0.82} L_{\odot}$. Based on the measured accretion luminosities, we investigate the hypothesis of star formation history in the CMa- $\ell 224$. Their median values suggest that Cluster C, where most of YSO candidates have been identified, might be the most evolved part of the region. The accretion luminosities are similar to those observed toward low-mass YSOs in the Perseus and Orion molecular clouds, and they do not reveal the impact of lower metallicity. Similar studies in other outer Galaxy clouds covering a wide range of metallicities are critical to gain a complete picture of star formation in the Galaxy.

Unified Astronomy Thesaurus concepts: [Star-forming regions \(1565\)](#)

1. Introduction

Stars form as a result of complex physico-chemical processes initiated by the gravitational collapse of a dense and cold molecular cloud. The formation of a rotating envelope and the embedded disk is associated with the ejection of jets and disk winds, together responsible for the removal of the angular momentum (e.g., Frank et al. 2014). The interaction between jets/winds and the envelope leads to the formation of outflow cavities and the dispersion of some mass reservoir (van Kempen et al. 2010; Visser et al. 2012). Shock waves at the outflow/envelope interface compress and heat the envelope material to hundreds or thousands of kelvin, even around low-mass protostars (Kristensen et al. 2017; Karska et al. 2018).

The net mass growth of a young star is a balance between the mass accretion from the envelope–disk system and the mass ejection by jets and winds. The main accretion phase occurs during the earliest evolutionary stages of a young stellar object (YSO; Class 0 and Class I), accompanied by collimated H₂ jets

(Davis & Eisloffel 1995; Stanke et al. 2002; Kristensen et al. 2007) and more extended molecular outflows (van der Marel et al. 2013; Tobin et al. 2016; Mottram et al. 2017). Once the protostar evolves into Class II, the envelope mass reservoir is mostly depleted, the accretion rate decreases, and the outflow opening angle widens (Offner et al. 2011; Agra-Amboage et al. 2014). The gradual decrease of accretion rates (Manara et al. 2012; Ansdell et al. 2017; Testi et al. 2022) is accompanied by decreasing mass-loss rates and a transition from mostly molecular to atomic/ionic outflows (Nisini et al. 2015; Bally 2016).

The location of a star-forming region in the Galaxy may influence the process of mass assembly. In the outer Galaxy, the gas surface density in molecular clouds is known to be lower than those in the solar neighborhood (Roman-Duval et al. 2010). The decrease of metallicity with Galactocentric radius, traced by Fe or O abundance gradients, also translates to lower dust and molecular gas abundances (Sodroski et al. 1997; Lépine et al. 2011; Hawkins 2023). Additionally, lower cosmic-ray fluxes and the interstellar UV radiation field reduce the amount of gas and dust heating (Bloemen et al. 1984). These factors may affect physical and chemical conditions in star-forming regions and result in *globally* lower star formation

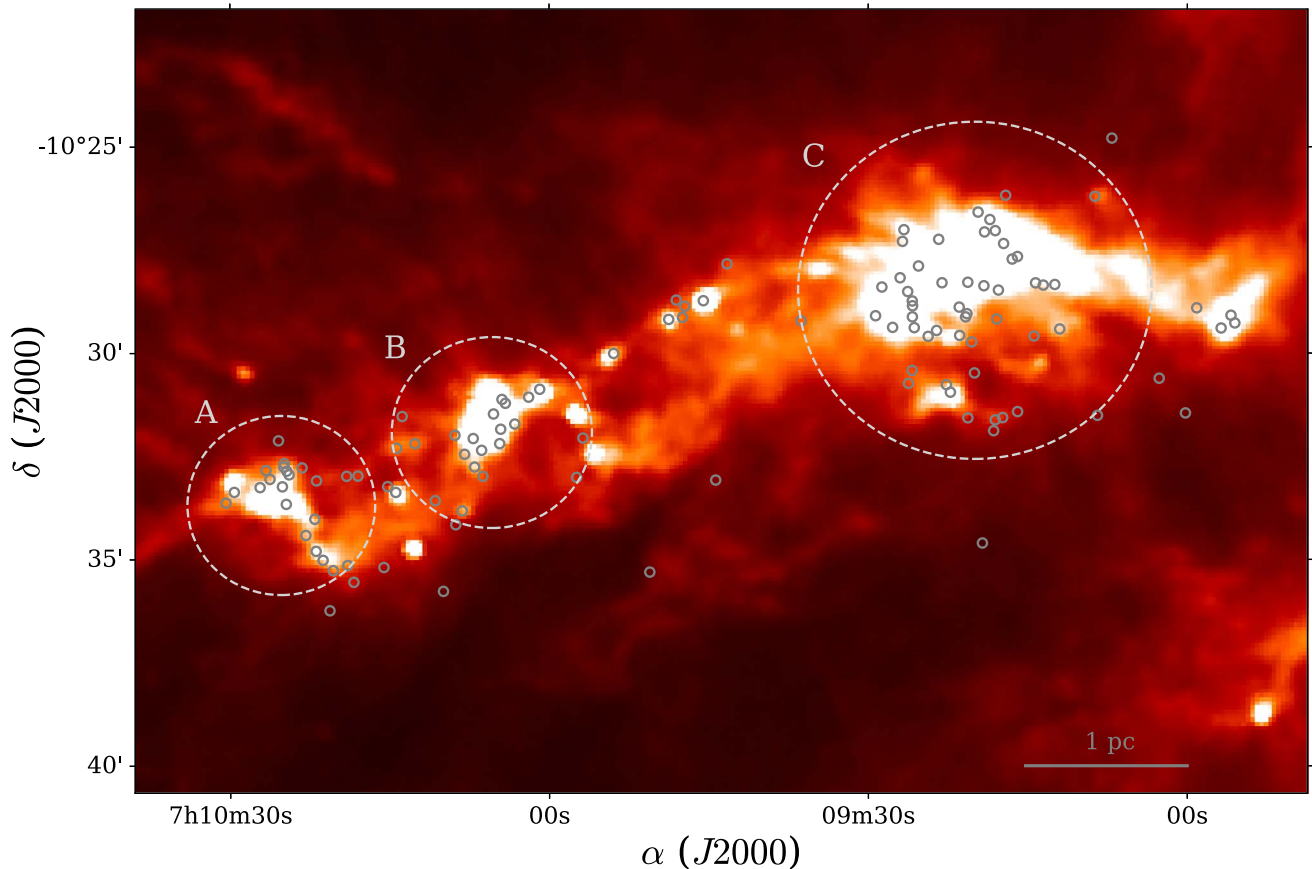


Figure 1. Herschel/SPIRE 250 μm image of the main filament in the CMa- ℓ 224 star-forming region. Gray circles show the positions of YSO candidates observed with VLT/KMOS, while light gray dashed ellipses indicate regions hosting clusters of sources with the extended 4.5 μm emission (most likely tracing outflows) defined in Sewilo et al. (2019), Clusters A, B, and C. North is up, and east is to the left.

rates and efficiencies in the outer Galaxy (Kennicutt & Evans 2012; Heyer & Dame 2015; Djordjevic et al. 2019).

Recent infrared studies revealed significant star formation activity in the Canis Major star-forming region in the outer Galaxy (Fischer et al. 2016; Sewilo et al. 2019). The $2^\circ.5 \times 1^\circ.4$ region in Canis Major dubbed CMa- ℓ 224, centered on $(l, b) = (224^\circ.5, -0^\circ.65)$, is particularly interesting because it hosts clusters of sources with extended 4.5 μm emission (likely tracing outflows), many of which were identified as YSOs (Sewilo et al. 2019). CMa- ℓ 224 is located at a distance of 0.92 kpc from the Sun and 9.1 kpc from the Galactic Center (e.g., Claria 1974), where a subsolar metallicity is predicted by the O/H Galactocentric radial gradients determined based on the observations of H II regions ($Z \sim 0.55\text{--}0.73 Z_\odot$; Balsa et al. 2011; Fernández-Martín et al. 2017; Esteban & García-Rojas 2018). CMa- ℓ 224 corresponds to a local peak of the H_2 column density and the lowest dust temperatures in the far-infrared observations of the outer Galaxy by the Herschel infrared Galactic Plane Survey (Hi-GAL; Molinari et al. 2010). The region contains a complex network of star-forming filaments (Figure 1; Elia et al. 2013; Schisano et al. 2014) and a widespread emission in CO and its isotopologues, tracing dense, molecular gas (Olimi et al. 2016; Benedettini et al. 2020; Lin et al. 2021).

Sewilo et al. (2019) identified 294 YSO candidates in CMa- ℓ 224 based on the photometric data from the near- and mid-infrared catalogs: Spitzer’s “GLIMPSE360: Completing the Spitzer Galactic Plane Survey” (PI: B. Whitney), the Two Micron All Sky Survey (2MASS; Skrutskie et al. 2006), and

the AllWISE catalog that combines the Wide-field Infrared Survey Explorer (WISE; Wright et al. 2010) and NEOWISE (Mainzer et al. 2011) data. Some YSO candidates in CMa- ℓ 224 are associated with the extended 4.5 μm emission (extended green objects; Cyganowski et al. 2008), likely dominated by the H_2 line emission from outflow shocks (e.g., Cyganowski et al. 2011). The spectral energy distribution (SED) fitting with the Robitaille (2017) YSO models identified 37 sources with envelopes, i.e., Class 0/I YSOs. Thus, CMa- ℓ 224 offers an opportunity to evaluate how metallicity affects the ongoing star formation in a region that is significantly closer than, for example, the Magellanic Clouds.

In this paper, we address the following questions: What are the mass accretion rates in YSOs in CMa- ℓ 224? How are they connected to the star formation scenarios in this region? Does the reduced gas metallicity have any impact on the accretion properties of YSOs in CMa- ℓ 224?

To this end, we present the results of the integral field spectroscopy of 124 YSO candidates in the CMa- ℓ 224 star-forming region using the K -band Multi Object Spectrograph (KMOS; Sharples et al. 2013) on the Very Large Telescope (VLT). VLT/KMOS provides $2''.8 \times 2''.8$ spectral maps in rovibrational H_2 lines, hydrogen $\text{Br}\gamma$, and CO bandhead at 2.3 μm . At the distance of CMa- ℓ 224, we obtained $\sim 2580 \times 2580$ au maps at a physical resolution of 184 au.

The paper is organized as follows. In Section 2, we describe our sample selection, KMOS observations, and data reduction. In Section 3, we present the continuum and line emission maps, provide the statistics on line detections, discuss gas spatial

distribution and describe calculations of the mass accretion rates. In Section 4, we discuss the results in the context of the star formation scenarios in CMa- ℓ 224, and in Section 5, we present a summary and our conclusions.

This paper is the first in a series presenting the multi-wavelength spectroscopy of YSO candidates in the CMa- ℓ 224 star-forming region. Two forthcoming papers will discuss the ^{13}CO and C^{18}O 2-1 observations of YSO candidates in the main filament in CMa- ℓ 224 with the Atacama Large Millimeter/submillimeter Array (ALMA; M. Koprowski et al. 2023, in preparation), and the spectral types and excess continuum measurements toward YSO candidates in the second brightest filament in the region using the SpeX instrument at the NASA Infrared Telescope Facility (IRTF; N. Le et al. 2023, in preparation).

2. KMOS Observations and Data Reduction

We used VLT/KMOS to observe YSO candidates in the CMa- ℓ 224 star-forming region as part of the ESO program 0102.C-0914(A) (PI: A. Karska). The sources were selected from the catalog of YSO candidates from Sewilo et al. (2019) based on their 2MASS K -band brightness and location within two KMOS patrol fields.

Targets were selected from the K -band magnitude range of 9.515 to ensure a sufficient signal-to-noise ratio (S/N) without saturation for a single integration time applied to all exposures.

KMOS is a second-generation instrument operating in the near-infrared (near-IR) at the Nasmyth B focus of the VLT Unit Telescope 1 on Paranal in Chile, in operation since 2012 November (Sharples et al. 2013). It performs integral field spectroscopy for up to 24 targets simultaneously. Each of the 24 pick-off arms is connected to one of three identical spectrographs and detectors. KMOS arms are allocated in two planes (“top” and “bottom”) to avoid interference between them. The patrol field is $7''.2$ in diameter, the size of each integral field unit (IFU) is $2''.8 \times 2''.8$, and the spatial sampling (spaxel size) is $0''.2 \times 0''.2$.

Observations were prepared using the KMOS Arm Allocator (KARMA¹⁵) and p2,¹⁶ a web-based tool for preparation of the Phase 2 material. The observations were performed in 2018 October and December.

We used the K grating with the spectral range from 1.93 to $2.50 \mu\text{m}$ and resolving power R of ~ 4000 , with a spectral sampling $\Delta\lambda$ of $\sim 2.8 \text{ \AA}$ per spectral element, corresponding to $\sim 39.7 \text{ km s}^{-1}$ at $2.1218 \mu\text{m}$. The total integration time for each pointing was 1300 s, with five single exposures of 260 s, dithered by $0''.2$.

The nod-to-sky mode was used to observe sources in both the “science” and “sky” pointings. The arms originally observing targets were next directed to the sky area, while those observing the sky were capturing science objects in the “sky” pointing, usually offset by a few arcmin. One of the pick-off arms was broken during semester 102, which resulted in a lack of observations for six sources.

Table 1 shows the summary of the atmospheric conditions during our KMOS observations. The amount of precipitable water vapor (PWV) was in the range from ~ 2.5 to 4 mm, and the sky was covered with thin cirrus (TN). Seeing measured at

Table 1
Atmospheric Conditions

OB	Date	Seeing ($''$)	Airmass ^a		PWV (mm)	Sky	Grade
			SCI	STD			
1	23.10.2018	~ 1.5	1.20	1.70	< 2.5	TN	B
2	24.10.2018	~ 0.5	1.18	1.15	~ 2.5	TN	B
3	25.10.2018	~ 0.6	1.25	1.83	~ 2.5	TN	B
4	11.12.2018	~ 1.0	1.34	1.20	~ 4.0	TN	B
5	11.12.2018	< 0.6	1.13	1.20	~ 4.0	TN	B
6	11.12.2018	~ 0.5	1.05	1.20	> 3.0	TN	B

Note.

^a A mean airmass during the integration made for one of the targets per OB (SCI) and for a standard star used for telluric correction (STD).

the observatory site was typically below $1''$, with the point-spread function (PSF) of the data in the $0''.4$ – $0''.7$ range.

Data reduction was performed using the ESO Recipe Execution Tool (esorex, version 2.0.2 of the KMOS pipeline), the terminal-based software. The standard procedure included the processing of the raw calibration data: dark, flat-field, illumination, and sky subtraction (a single sky observation per science target). The wavelength calibration was done using the argon–neon lamp.

We used a standard procedure for the telluric correction and flux calibration by observing a standard star, one per each of the three detectors, and comparing observations to the stellar model. The standard pipeline does not account for the difference in the airmass between the science and standard star observations, which might lead to under- or overestimation of the telluric lines by up to 10%. Additionally, each of the 24 arms has a slightly different spectral resolution, resulting in different line shapes. It is possible to account for these effects by modeling the telluric lines using the science or the standard star spectrum (Coccatto et al. 2019). However, for our science data with the median S/N measured on the featureless parts of the spectra of less than 50, the differences between the standard method we used and modeling are negligible because the noise dominates any uncertainty coming from the telluric standard (Coccatto et al. 2019).

The imperfect telluric correction is a source of the unknown uncertainty, especially in the red part of the K band (above $2.4 \mu\text{m}$), where some of the H_2 lines are located. Also, other telluric features are poorly corrected, e.g., near $2 \mu\text{m}$. All spectral regions particularly affected by the telluric lines are marked on the figures.

The reduced single exposures were collapsed into the final data cubes. The entire process of creating the 3D KMOS science data cubes is described in Davies et al. (2013). For the analysis of sources observed multiple times, we used the data cubes combined with the KMOS pipeline task `combine`.

The K -band continuum fluxes are calculated by fitting a seventh-order Chebyshev polynomial to the spectrum in each spaxel (spatial pixel) of the data cube. The continuum level is defined as the value of the fit at $2.12 \mu\text{m}$, near the middle of the Johnson K -band and the rest wavelength of the 1-0 S(1) H_2 line. The noise of the spectrum is calculated as the rms of deviations from the continuum in the line-free parts of the spectrum: 2.076 – $2.106 \mu\text{m}$, 2.125 – $2.143 \mu\text{m}$, 2.179 – $2.187 \mu\text{m}$, 2.198 – $2.201 \mu\text{m}$, and 2.268 – $2.274 \mu\text{m}$. In four cases of faint

¹⁵ <https://www.eso.org/sci/observing/phase2/SMGuidelines/KARMA.html>

¹⁶ <https://www.eso.org/sci/observing/phase2/p2intro.html>

Table 2
Catalog of Sources in CMA-*l*224 Detected with VLT/KMOS

No.	IRAC Designation ^a SSTGLMA	R.A. (^h ^m ^s)	Decl. (deg ^{''})	Continuum near 2.12 μm (10^{-17} erg s ⁻¹ cm ⁻² \AA^{-1})	Class	YSO ^b	Remarks
1	G224.2025-00.8569	07 09 07.09	-10 24 47.50	08.27 \pm 0.12	II	d	
2	G224.2265-00.8620	07 09 08.69	-10 26 12.22	26.40 \pm 0.13	II	e+d	ext. H ₂ emission
3	G224.2420-00.8313	07 09 17.08	-10 26 10.67	13.05 \pm 0.14	II	d	
4	G224.2449-00.9307	07 08 55.89	-10 29 04.97	07.02 \pm 0.21	I	null	ext. H ₂ emission
5	G224.2470-00.9334	07 08 55.53	-10 29 16.20	38.74 \pm 0.60	I	e	
6	G224.2483-00.9176	07 08 59.12	-10 28 54.25	11.22 \pm 0.14	II	d	
7	G224.2512-00.9297	07 08 56.82	-10 29 23.57	07.49 \pm 0.29	I	null	
8	G224.2530-00.8250	07 09 19.67	-10 26 35.06	07.84 \pm 0.15	II	d	
9	G224.2535-00.8306	07 09 18.56	-10 26 45.89	10.17 \pm 0.10	II	d	
10	G224.2567-00.8346	07 09 18.06	-10 27 02.03	11.21 \pm 0.13	II	d	near edge ^d
11 ^c	G224.2591-00.8305	07 09 19.19	-10 27 03.71	2.52 \pm 0.57	I	null	integrated cont.
12	G224.2598-00.8398	07 09 17.27	-10 27 20.77	28.52 \pm 0.13	II	d	near edge
13	G224.2621-00.8470	07 09 15.97	-10 27 39.63	13.70 \pm 0.08	I	d	near edge
14 ^c	G224.2638-00.8456	07 09 16.47	-10 27 43.32	2.88 \pm 0.38	I	null	integrated cont.
15	G224.2652-00.8647	07 09 12.46	-10 28 20.32	13.27 \pm 0.12	I	d	ext. H ₂ emission
16	G224.2674-00.8609	07 09 13.54	-10 28 21.20	31.76 \pm 0.17	II	d	
17	G224.2680-00.8578	07 09 14.27	-10 28 17.95	3.29 \pm 0.12	II	null	
18	G224.2697-00.8168	07 09 23.38	-10 27 14.62	5.29 \pm 0.07	II	null	
19	G224.2724-00.8032	07 09 26.64	-10 27 00.62	3.11 \pm 0.11	I	d	near edge, ext. H ₂ emission
20	G224.2769-00.8049	07 09 26.78	-10 27 17.65	20.18 \pm 0.10	II	d	near edge
21A	G224.2778-00.8465	07 09 17.76	-10 28 28.62	0.85 \pm 0.13	I	null	on edge
21B	G224.2778-00.8465	07 09 17.83	-10 28 29.02	0.44 \pm 0.12			separation 1073au
22	G224.2784-00.8408	07 09 19.14	-10 28 21.54	11.88 \pm 0.06	II	null	near edge
23	G224.2800-00.8346	07 09 20.64	-10 28 17.05	25.24 \pm 0.14	I	null	
24	G224.2802-00.8747	07 09 12.00	-10 29 25.00	15.79 \pm 0.35	II	d	
25	G224.2802-00.9179	07 09 02.64	-10 30 36.58	13.07 \pm 0.31	II	null	
26 ^c	G224.2828-00.8148	07 09 25.28	-10 27 53.42	1.07 \pm 0.08	I	d	integrated cont.
28	G224.2872-00.8673	07 09 14.41	-10 29 35.21	24.28 \pm 0.40	II	d	
29	G224.2881-00.9333	07 09 00.17	-10 31 27.03	20.35 \pm 0.28	II	null	
30	G224.2882-00.8515	07 09 17.92	-10 29 10.51	13.91 \pm 0.10	II	d	near edge
31	G224.2903-00.8108	07 09 27.00	-10 28 10.52	2.08 \pm 0.14	II	null	
32	G224.2905-00.8364	07 09 21.45	-10 28 53.19	68.62 \pm 0.10	II	d	
33	G224.2914-00.8402	07 09 20.72	-10 29 02.78	6.02 \pm 0.09	II	d	
34	G224.2928-00.8403	07 09 20.84	-10 29 07.42	11.50 \pm 0.07	II	null	
35	G224.2939-00.8157	07 09 26.29	-10 28 30.56	13.85 \pm 0.21	II	e+d	
36A	G224.2965-00.8191	07 09 25.86	-10 28 44.29	98.54 \pm 0.41	II	d	separation 1086au
36B	G224.2965-00.8191	07 09 25.94	-10 28 44.29	6.51 \pm 0.04			on edge
38A	G224.2983-00.8203	07 09 25.84	-10 28 51.25	12.54 \pm 0.10	I	null	
38B	G224.2983-00.8203	07 09 25.78	-10 28 52.25	2.84 \pm 0.09			separation 1178 au
39	G224.3005-00.8417	07 09 21.41	-10 29 34.38	193.49 \pm 0.67	II	d	ext. H ₂ emission
40	G224.3006-00.8470	07 09 20.27	-10 29 43.74	680.28 \pm 15.78	II	d	
41	G224.3022-00.8221	07 09 25.85	-10 29 07.35	23.01 \pm 0.10	I	null	
42	G224.3028-00.8329	07 09 23.58	-10 29 27.12	14.65 \pm 0.29	II	d	
43	G224.3044-00.9038	07 09 08.45	-10 31 30.57	14.57 \pm 0.17	II	d	
44	G224.3057-00.8247	07 09 25.68	-10 29 23.07	131.32 \pm 0.67	I	null	
45	G224.3063-00.8310	07 09 24.37	-10 29 35.76	17.46 \pm 0.55	II	d	
46	G224.3083-00.8093	07 09 29.31	-10 29 05.72	113.91 \pm 0.13	II	d	ext. H ₂ emission
47	G224.3095-00.8172	07 09 27.71	-10 29 22.66	3.73 \pm 0.08	I	e	ext. H ₂ emission
48	G224.3112-00.8536	07 09 20.01	-10 30 28.89	41.21 \pm 0.05	II	d	
49	G224.3159-00.7490	07 09 43.27	-10 27 50.24	13.38 \pm 0.12	I	d	near edge
50	G224.3173-00.8757	07 09 15.96	-10 31 25.09	12.63 \pm 0.07	II	d	
51	G224.3204-00.8462	07 09 22.65	-10 30 45.91	29.36 \pm 0.50	II	null	
52A	G224.3215-00.8319	07 09 25.88	-10 30 25.24	08.71 \pm 0.02	II	null	
52B	G224.3215-00.8319	07 09 25.83	-10 30 25.24	6.85 \pm 0.02			separation 552 au
53	G224.3222-00.8717	07 09 17.36	-10 31 33.78	19.90 \pm 0.46	II	d	
54	G224.3225-00.8490	07 09 22.28	-10 30 56.90	702.81 \pm 1.86	I	null	ext. H ₂ emission
55A	G224.3233-00.7848	07 09 36.31	-10 29 12.99	33.38 \pm 0.13	II	d	
55B	G224.3233-00.7848	07 09 36.27	-10 29 13.19	27.61 \pm 0.08			separation 582 au
56	G224.3243-00.8696	07 09 18.06	-10 31 37.05	11.24 \pm 0.22	II	d	
57	G224.3268-00.8331	07 09 26.22	-10 30 44.05	10.33 \pm 0.06	II	null	
58	G224.3285-00.8597	07 09 20.64	-10 31 34.20	134.72 \pm 1.35	II	d	
59	G224.3286-00.8709	07 09 18.21	-10 31 52.88	21.39 \pm 0.09	II	d	
60	G224.3333-00.7476	07 09 45.51	-10 28 43.81	33.59 \pm 0.13	I	e	ext. H ₂ emission
61	G224.3379-00.7384	07 09 48.05	-10 28 42.87	29.73 \pm 0.31	II	d	near edge
62	G224.3386-00.7425	07 09 47.25	-10 28 51.88	08.02 \pm 0.27	II	d	near edge
63	G224.3430-00.7437	07 09 47.47	-10 29 08.11	18.24 \pm 0.30	II	d	near edge
64	G224.3462-00.7394	07 09 48.76	-10 29 10.99	5.18 \pm 0.12	I	e+d	near edge, ext. H ₂ emission
65	G224.3684-00.7267	07 09 53.94	-10 30 00.37	152.96 \pm 1.71	II	e+d	
66	G224.3710-00.8882	07 09 19.27	-10 34 36.14	07.37 \pm 0.14	II	null	near edge
68	G224.3955-00.7851	07 09 44.35	-10 33 04.55	67.11 \pm 0.99	II	d	
69 ^c	G224.3986-00.7060	07 10 01.84	-10 31 02.49	00.08 \pm 0.14	I	null	integrated cont.

Table 2
(Continued)

No.	IRAC Designation ^a SSTGLMA	R.A. (^h ^m ^s)	Decl. (deg ^{''})	Continuum near 2.12 μm (10^{-17} erg s ⁻¹ cm ⁻² Å ⁻¹)	Class	YSO ^b	Remarks
70	G224.4042-00.7319	07 09 56.84	-10 32 03.40	08.36 ± 0.08	II	d	
71	G224.4047-00.6971	07 10 04.45	-10 31 07.18	16.38 ± 0.26	II	d	
72	G224.4055-00.6989	07 10 04.13	-10 31 12.79	14.10 ± 0.34	II	null	uncorr. H ₂ emission ^c
73	G224.4111-00.7059	07 10 03.25	-10 31 42.93	10.08 ± 0.04	I	d	
74	G224.4114-00.6969	07 10 05.25	-10 31 28.33	3.29 ± 0.15	II	null	
75	G224.4157-00.7023	07 10 04.57	-10 31 50.47	6.83 ± 0.15	II	d	
76	G224.4195-00.7372	07 09 57.43	-10 33 00.55	11.10 ± 0.33	II	d	
77	G224.4210-00.7045	07 10 04.67	-10 32 11.44	2.83 ± 0.03	I	e+d	
78	G224.4238-00.6944	07 10 07.16	-10 32 04.00	13.27 ± 0.05	II	null	uncorr. H ₂ emission
79	G224.4259-00.6877	07 10 08.87	-10 31 59.31	6.82 ± 0.16	II	d	
80	G224.4266-00.6996	07 10 06.37	-10 32 21.11	35.91 ± 0.22	II	null	uncorr. H ₂ emission
81	G224.4285-00.6662	07 10 13.83	-10 31 31.86	25.17 ± 0.75	II	d	
82A	G224.4309-00.6943	07 10 07.97	-10 32 26.94	08.97 ± 0.11	II	e+d	
82B	G224.4309-00.6943	07 10 08.00	-10 32 26.34	07.96 ± 0.25			separation 663 au
83	G224.4338-00.7003	07 10 07.03	-10 32 45.39	4.11 ± 0.21	I	e+d	ext. H ₂ emission?
84	G224.4356-00.7049	07 10 06.25	-10 32 59.03	67.02 ± 1.28	II	e	
85	G224.4361-00.6756	07 10 12.64	-10 32 11.47	26.07 ± 0.07	II	null	
86A	G224.4404-00.7799	07 09 50.55	-10 35 18.30	08.66 ± 0.08	II	d	
86B	G224.4404-00.7799	07 09 50.55	-10 35 19.30	5.73 ± 0.08			separation 920 au
87A	G224.4410-00.6702	07 10 14.35	-10 32 18.18	1.89 ± 0.11	I	d	ext. H ₂ emission?
87B	G224.4410-00.6702	07 10 14.42	-10 32 18.38	1.58 ± 0.17			separation 938 au
88	G224.4514-00.7054						not det., uncorr. H ₂ emission
89A	G224.4528-00.6930	07 10 10.73	-10 33 34.32	4.21 ± 0.03	II	null	
89B	G224.4528-00.6930	07 10 10.76	-10 33 34.32	4.27 ± 0.05			hardly resolved, sep. 368 au
90	G224.4564-00.6744	07 10 15.20	-10 33 13.83	09.90 ± 0.15	I	null	
91A	G224.4567-00.6781	07 10 14.44	-10 33 22.29	91.33 ± 1.19	I	null	ext. H ₂ emission
91B	G224.4567-00.6781	07 10 14.43	-10 33 21.49	22.22 ± 0.10			ext. H ₂ emission, sep. 759 au
92	G224.4577-00.7046	07 10 08.80	-10 34 09.34	17.79 ± 0.57	null	d	
93	G224.4578-00.6621	07 10 18.00	-10 32 58.47	16.30 ± 0.06	II	d	
94	G224.4593-00.6284	07 10 25.47	-10 32 07.09	17.32 ± 0.36	II	d	
95	G224.4599-00.6582	07 10 19.06	-10 32 58.73	6.80 ± 0.14	II	d	
96	G224.4649-00.6415	07 10 23.25	-10 32 46.55	42.58 ± 1.03	II	e	
97	G224.4664-00.6346	07 10 24.93	-10 32 40.28	78.36 ± 0.87	II	d	
98	G224.4669-00.6489	07 10 21.89	-10 33 05.39	14.29 ± 0.16	II	d	
99	G224.4677-00.6351	07 10 24.98	-10 32 45.19	12.05 ± 0.10	I	null	
100	G224.4687-00.6368	07 10 24.70	-10 32 51.26	12.85 ± 0.37	I	null	ext. H ₂ emission
101	G224.4697-00.6386	07 10 24.48	-10 32 56.56	10.41 ± 0.11	II	null	near edge
102	G224.4721-00.6296	07 10 26.65	-10 32 50.22	94.01 ± 0.93	II	d	
103	G224.4746-00.6328	07 10 26.27	-10 33 03.10	16.35 ± 0.16	I	null	
104	G224.4751-00.6383	07 10 25.10	-10 33 14.00	54.74 ± 0.42	II	d	
105	G224.4793-00.6309	07 10 27.20	-10 33 15.10	3.60 ± 0.05	II	d	
106	G224.4806-00.6430	07 10 24.74	-10 33 39.50	1.94 ± 0.23	I	null	
108	G224.4838-00.7128	07 10 09.97	-10 35 46.15	14.17 ± 0.04	II	d	
109	G224.4856-00.6229	07 10 29.63	-10 33 22.03	08.77 ± 0.20	I	e+d	ext. H ₂ emission
110	G224.4859-00.6880	07 10 15.56	-10 35 11.36	07.41 ± 0.07	II	d	
111	G224.4883-00.6555	07 10 22.90	-10 34 24.70	33.94 ± 0.12	II	d	ext. H ₂ emission
112A	G224.4908-00.6223	07 10 30.41	-10 33 37.50	2.25 ± 0.06	I	d	
112B	G224.4908-00.6223	07 10 30.36	-10 33 37.50	2.14 ± 0.06			separation 736 au
113	G224.4916-00.6754	07 10 18.97	-10 35 08.47	07.11 ± 0.13	II	d	
114	G224.4921-00.6620	07 10 21.94	-10 34 47.82	9.08 ± 0.04	II	d	ext. H ₂ emission
115	G224.4942-00.6660	07 10 21.28	-10 35 00.91	19.05 ± 0.21	II	e+d	uncorr. H ₂ emission ^c
116	G224.4959-00.6715	07 10 20.33	-10 35 15.87	23.58 ± 0.15	II	d	
117	G224.4965-00.6805	07 10 18.39	-10 35 32.83	47.41 ± 0.58	II	d	
118	G224.5109-00.6777	07 10 20.64	-10 36 14.23	13.32 ± 0.09	II	d	

Notes. Resolved binary candidates are marked with “A” and “B” for the brighter and fainter source, respectively. The separation between the two binary components is given in au in the Remarks column for component “B.” The pixel size ($0''.2$) corresponds to 184 au.

^a GLIMPSE360 IRAC designations are “SSTGLMA” followed by the names listed in this column; IRAC designations are based on Galactic coordinates (Meade et al. 2016).

^b The YSO classification from Sewilo et al. (2019); the YSO class and components (an envelope and/or a disk) identified based on the SED fitting with the Robitaille (2017) YSO models (e—envelope, e+d—envelope and disk, d—disk-only); “null” indicates that the SED fitting results are not provided in Sewilo et al. (2019).

^c Equatorial coordinates obtained from the integrated continuum maps in units of 10^{-18} erg s⁻¹ cm⁻². See text for details.

^d The “near edge” label is given to sources located off-center (less than $0''.8$ from the map’s edge).

^e The “uncorr. H₂ emission” note indicates the presence of the extended H₂ emission in the field that is unrelated to the studied source.

objects (Nos. 11, 14, 26, and 69), we integrate the continuum emission over the full spectral range in each spaxel to detect these sources at a $>3\sigma$ level and verify their coordinates; the spectral analysis remained unchanged.

The spectra of single sources were extracted using an aperture centered on the continuum peak with a radius of 3 pixels, typically containing $\sim 70\%$ of the total flux. For the binary candidates, different aperture sizes were used depending

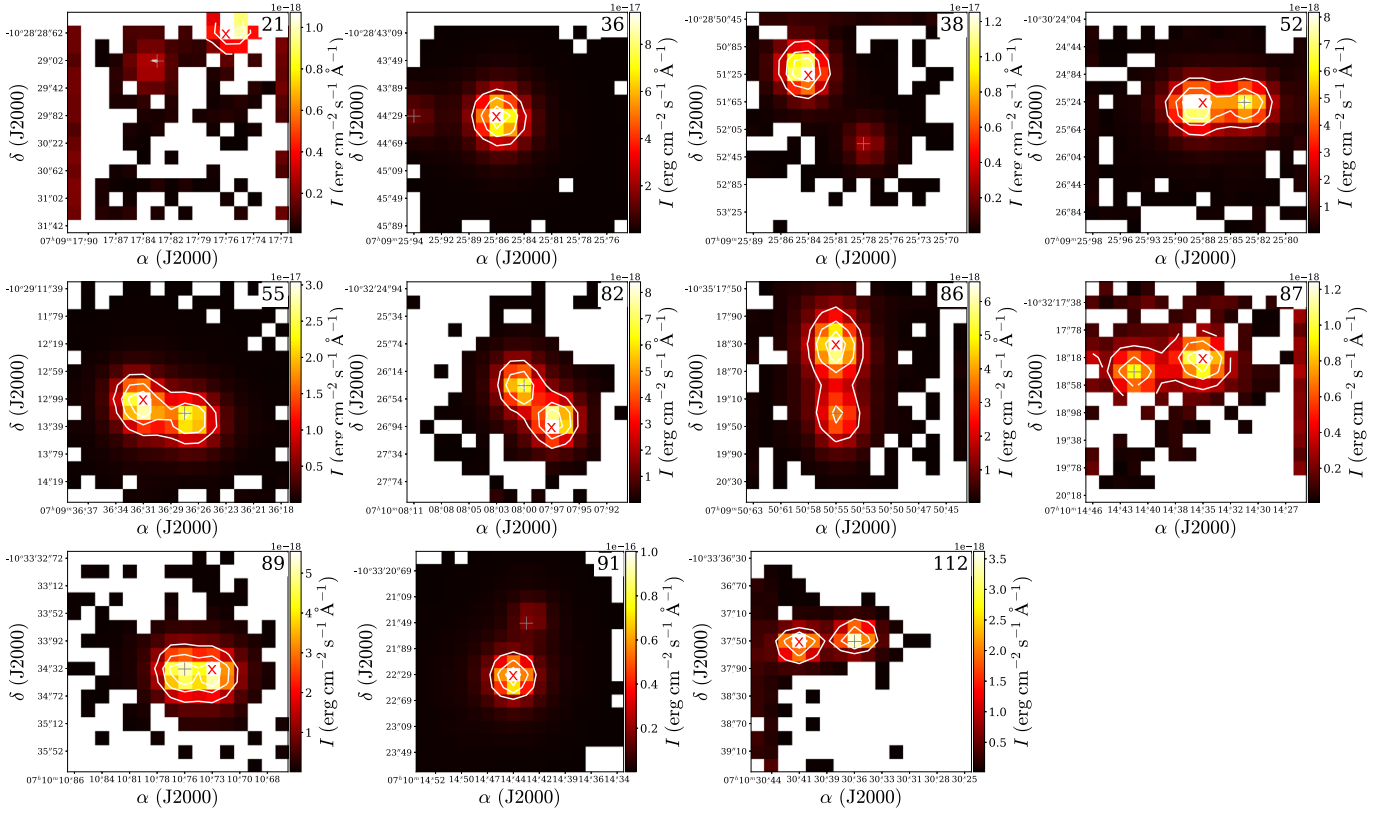


Figure 2. KMOS *K*-band continuum maps of YSO candidates with possible stellar companions. Only spaxels with the continuum flux above 3σ are shown. White contours correspond to 25%, 50%, and 75% of the *K*-band continuum peak. The position of the brighter source in each map is indicated with a red “x” symbol (the “A” component in Table 2), and the fainter one with a gray “+” symbol (the “B” component). The size of the pixel ($0''.2$) corresponds to 184 au.

on the separation between the stars. The spectra were subsequently aperture-corrected using the ratio of the continuum emission within the aperture to that in the entire field of view; see Appendix B for details.

Since KMOS is a moderate-resolution spectrograph, we assume a simplified shape of a spectral line and calculate integrated fluxes using Gaussian fits. The spectral line maps are constructed based on line fluxes estimated separately for each spaxel by fitting a Gaussian function to the emission line 50 times with randomly generated input parameters and choosing the fit with the lowest relative error. All fits were visually confirmed. The same approach is applied to fitting the spectral lines in the extracted spectra.

3. Data Analysis and Results

Out of 118 Spitzer YSO candidates observed with KMOS, five were not detected and 11 were resolved into two near-IR sources. In total, our KMOS observations provide the *K*-band data for 124 sources.

The IFU observations deliver both the spectral and spatial information. The *K*-band continuum emission allows us to identify all the continuum components and determine their positions and *K*-band fluxes. The spatial extent of the atomic and molecular emission hints at the underlying physical mechanisms and their characteristics. The hydrogen Br γ emission is correlated with the UV continuum excess diagnostic of mass accretion. The CO rovibrational bandhead traces the inner disk. The H $_2$ emission lines, including the bright 1-0 S(1) line at $2.12 \mu\text{m}$, trace jets, and shocks.

In this section, we discuss the spatial distribution of gas and dust, and summarize the line detections and kinematic information.

3.1. *K*-band Continuum Emission

All the *K*-band continuum sources detected with VLT/KMOS in CMa- ℓ 224 are listed in Table 2. The table provides the sources’ GLIMPSE360 catalog names and assigned KMOS IDs, their equatorial coordinates corresponding to the position of the *K*-band continuum peak, the *K*-band continuum fluxes estimated near $2.12 \mu\text{m}$, the YSO classification from Sewilo et al. (2019), and remarks on pointing, multiplicity, and the association with extended H $_2$ emission. Two *K*-band continuum components have been detected toward 11 fields centered on single Spitzer YSO candidates (see Figure 2); the brighter source is listed in Table 2 as source “A” and the fainter one as source “B.”

Selected *K*-band continuum maps are shown in Figure 2 (11 fields with the detection of two sources) and Appendix A (the remaining fields).

We consider the possibility that two sources detected in a single KMOS field are two components of a binary star/YSO. The median separation between the two components of the “binary star candidates” in CMa- ℓ 224 is 760 au (see Table 2), with a range from 370 au (source No. 89) to 1180 au (source No. 38). All but three pairs of visual binary star candidates have spectra typical of accreting young stars: emission of Br γ and/or H $_2$. Two more pairs have CO bandhead in absorption typical for cool stars. Given the

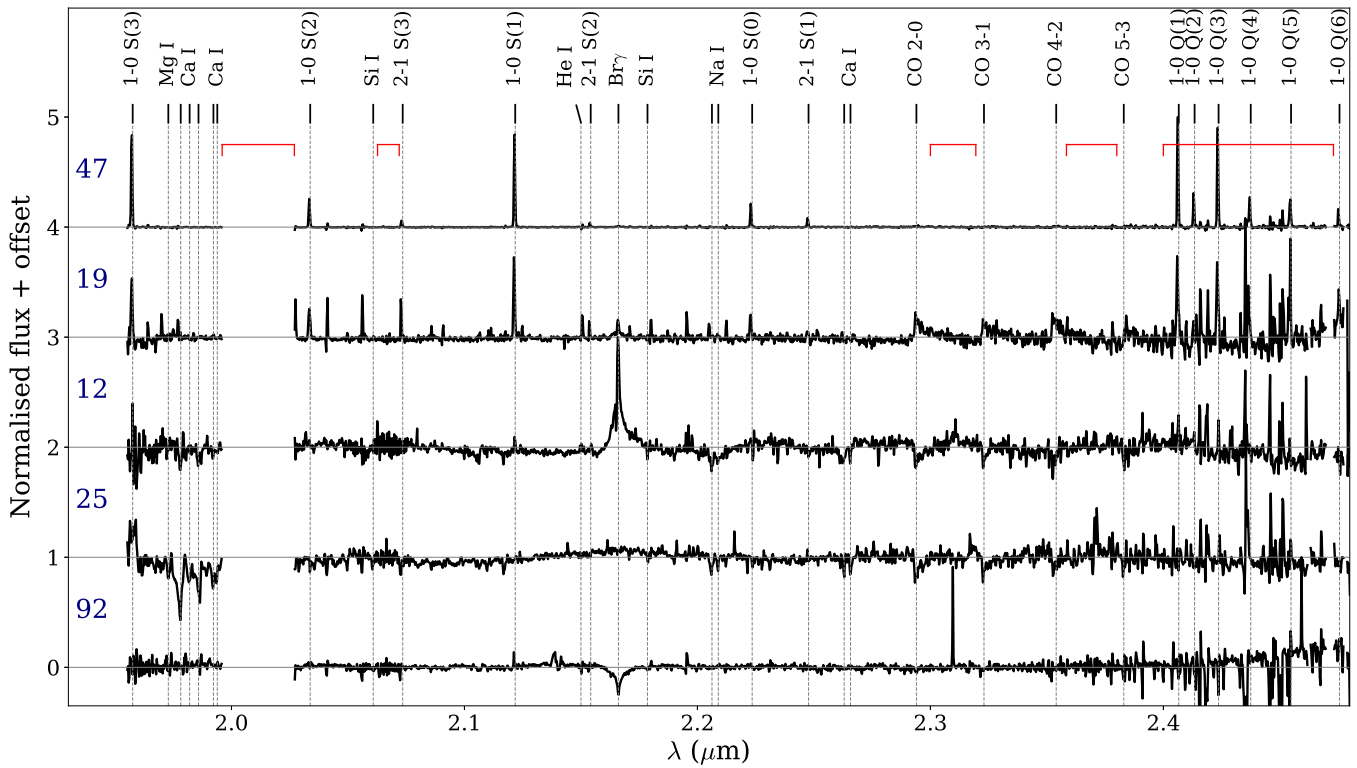


Figure 3. Example spectra of YSOs in CMa-ℓ224. Source names from Table 2 (No.) are provided on the left side of the respective spectra. All spectra are normalized to the continuum peak flux density in the wavelength range from 1.97 to 2.47 μm . The red horizontal lines show spectral ranges most affected by telluric lines; the wavelength range around 2.0 μm has been removed for clarity of the plot.

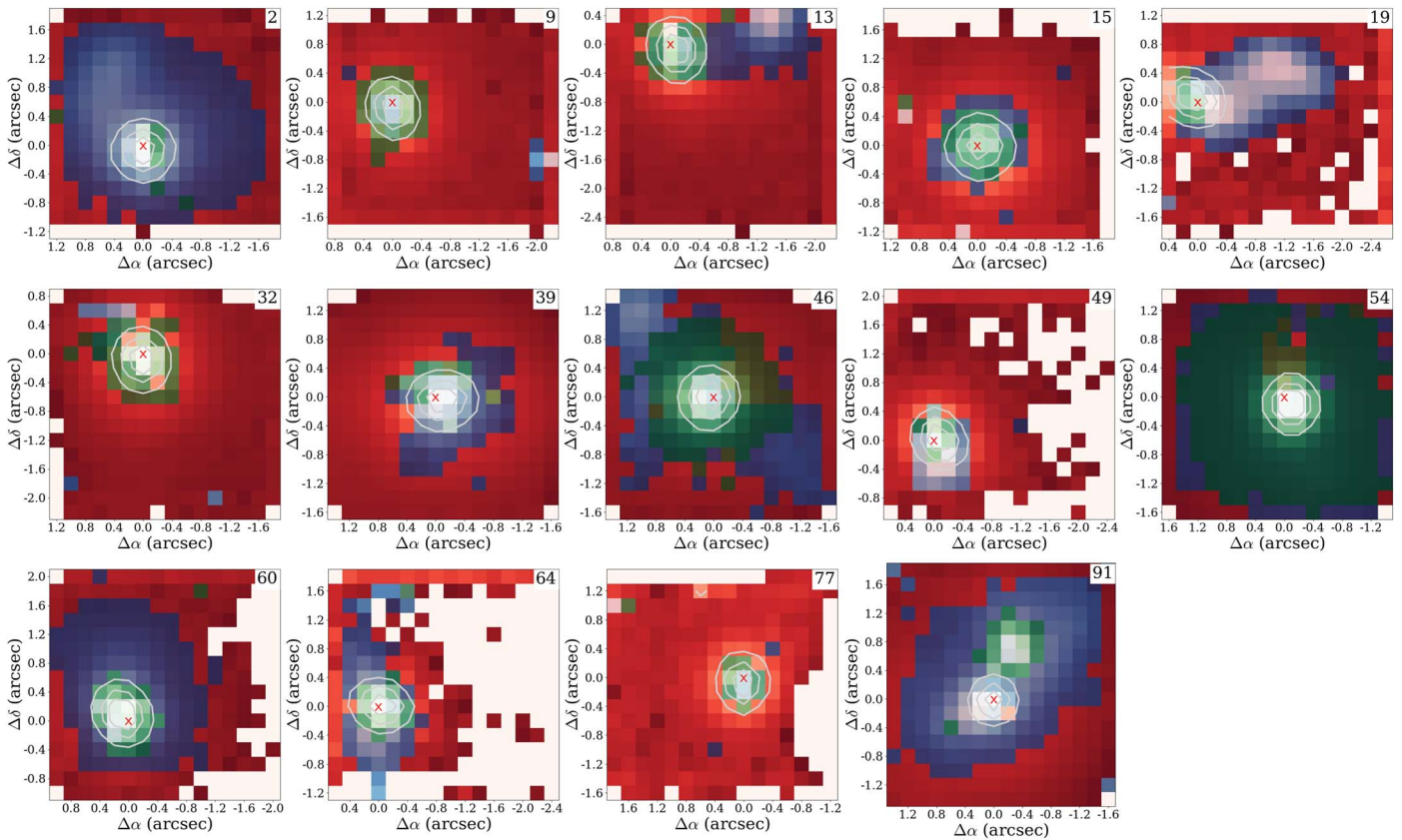


Figure 4. Three-color composite images of YSO candidates with $\geq 3\sigma$ detection in the H_2 line at 2.12 μm (in blue), $\text{Br}\gamma$ line at 2.17 μm (in green), and the K -band continuum (in red). In each image, white contours correspond to the K -band continuum emission with contour levels of 25%, 50%, and 75% of the continuum peak marked with the red “x” symbol. Source IDs are indicated in the upper right corners.

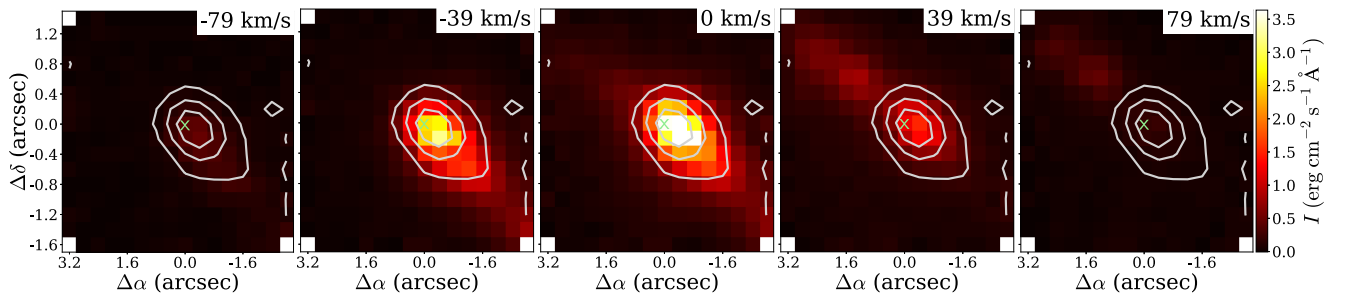


Figure 5. The H_2 1-0 S(1) channel maps for source No. 47. The velocities relative to the rest velocity of the H_2 line are shown in the upper right corners. The green “x” symbol shows the position of the K -band continuum peak.

proximity of the sources, they may be physically related. If they are binary systems, the multiplicity fraction defined as the ratio of the number of multiple systems to the total number of systems (both single and multiple) is 0.09 ± 0.01 .¹⁷ For comparison, the multiplicity fraction for separations between 100 and 1000 au is 0.15 ± 0.04 for protostars in Perseus (Tobin et al. 2016), and the fractions are 0.14 ± 0.01 for protostars and 0.13 ± 0.01 for pre-main-sequence (PMS) stars, respectively, in the Orion molecular clouds (Kounkel et al. 2016). Adopting the approximate range recovered by KMOS (180-1180 au), the multiplicity fraction of protostars would be ~ 0.09 in Perseus and 0.12 in Orion.

In summary, the binary star candidates in CMa- ℓ 224 have a multiplicity fraction that is consistent with YSOs in other molecular clouds, once we account for close binaries that are unresolved with KMOS. A more robust comparison requires an unbiased survey of YSOs at their earliest evolutionary stages and will be presented in the second paper in this series.

3.2. Spectral Line Detections

KMOS spectra contain several atomic and molecular lines emerging as a result of mass accretion and/or ejection in YSOs. Additionally, transitions of many atomic absorption lines that originate from a stellar photosphere are also detected and can be used to estimate spectral types and luminosity classes of YSOs (e.g., Luhman & Rieke 1998; Nisini et al. 2005).

Figure 3 shows the K -band spectra toward selected YSO candidates with diverse characteristics to illustrate the differences between the sources. For example, sources No. 47 and 19 show a strong H_2 emission, with only the latter showing also clear $\text{Br}\gamma$ and CO detections. Sources No. 12 and 25 both show CO bandhead in absorption. Yet, only source No. 12 is characterized also by a broad emission-line profile in $\text{Br}\gamma$. Source No. 92 shows very weak H_2 emission, and $\text{Br}\gamma$ line in absorption. The line detections are discussed further in the subsequent sections.

3.2.1. $\text{Br}\gamma$

The most commonly detected line is the $2.1655 \mu\text{m}$ $\text{Br}\gamma$ hydrogen line, seen in emission in 58 sources (47%) and in absorption in 16 sources (13%). Twenty-six sources with the $\text{Br}\gamma$ emission also show the CO lines in absorption. A similar

pattern but with higher detection rates of the $\text{Br}\gamma$ emission ($\sim 75\%$) was found toward a sample of 19 Class I protostars (Connelley & Greene 2010, 2014). In a recent KMOS survey of YSOs in Perseus, the $\text{Br}\gamma$ was indeed more commonly detected in emission toward Class I (59%) than Class II YSOs (36%; Fiorellino et al. 2021).

The $\text{Br}\gamma$ line emission in our sources is compact and associated with the continuum emission (Section 3.1; see also Figure 4 and Appendix C). In low-mass YSOs, $\text{Br}\gamma$ emission originates from the close vicinity of the young star and usually traces magnetospheric accretion columns, with possible contributions from winds (Kraus et al. 2008). Some emission may also arise along the outflows (Beck et al. 2010).

The spatial extent of atomic emission of $\text{Br}\gamma$ -emitting gas is often more compact than molecular gas, with the exception of source No. 54, a bright star with a K -band magnitude of 9.9 (Figure 4). Extended emission around a young star can be partially explained by an emerging H II region, but a broad line profile suggests that other physical processes might also contribute (Cooper et al. 2013). The physical extent of ~ 2350 au of $\text{Br}\gamma$ emission from the source No. 54 cannot be explained with disk winds. In the subsequent analysis, the line fluxes are extracted from the area covering the continuum source, where $\text{Br}\gamma$ emission is likely dominated by accretion.

3.2.2. H_2

H_2 is a homonuclear molecule that lacks a permanent dipole moment, and thus only quadrupole transitions may occur ($\Delta J = 0, \pm 2$). The extended distribution of the H_2 emission and its velocity structure indicate the origin in bipolar outflows (Section 3.4). H_2 emission is detected in 33 sources in CMa- ℓ 224 (27%), including 14 that also show a detection of the $\text{Br}\gamma$ line in emission, and only three with the CO rovibrational lines in absorption. A similar H_2 detection rate of 23% was reported in a pioneering survey by Carr (1990). Larger rates have been found toward Class I protostars (43%, Connelley & Greene 2014) and higher-mass YSOs (56%, Cooper et al. 2013; 76%, Varricatt et al. 2010). The line fluxes are reported in Appendix B in Table 5.

3.2.3. CO

The CO bandhead in absorption traces the atmosphere of a star or a disk. Among YSO candidates in CMa- ℓ 224, the CO first overtone is detected in absorption in 60% of YSO candidates, predominantly (78%) in those classified as Class II (Sewifo et al. 2019; see also Table 2). Among Class I YSOs,

¹⁷ We follow Tobin et al. (2016) to estimate the uncertainty of derived multiplicity and adopt a bimodal statistic: $\sigma_{\text{multi}} = (N_{\text{multi}} \cdot (1 - N_{\text{multi}}/N_{\text{sys}}))^{-0.5}/N_{\text{sys}}$, where N_{multi} is the number of multiple systems and N_{sys} is the total number of systems.

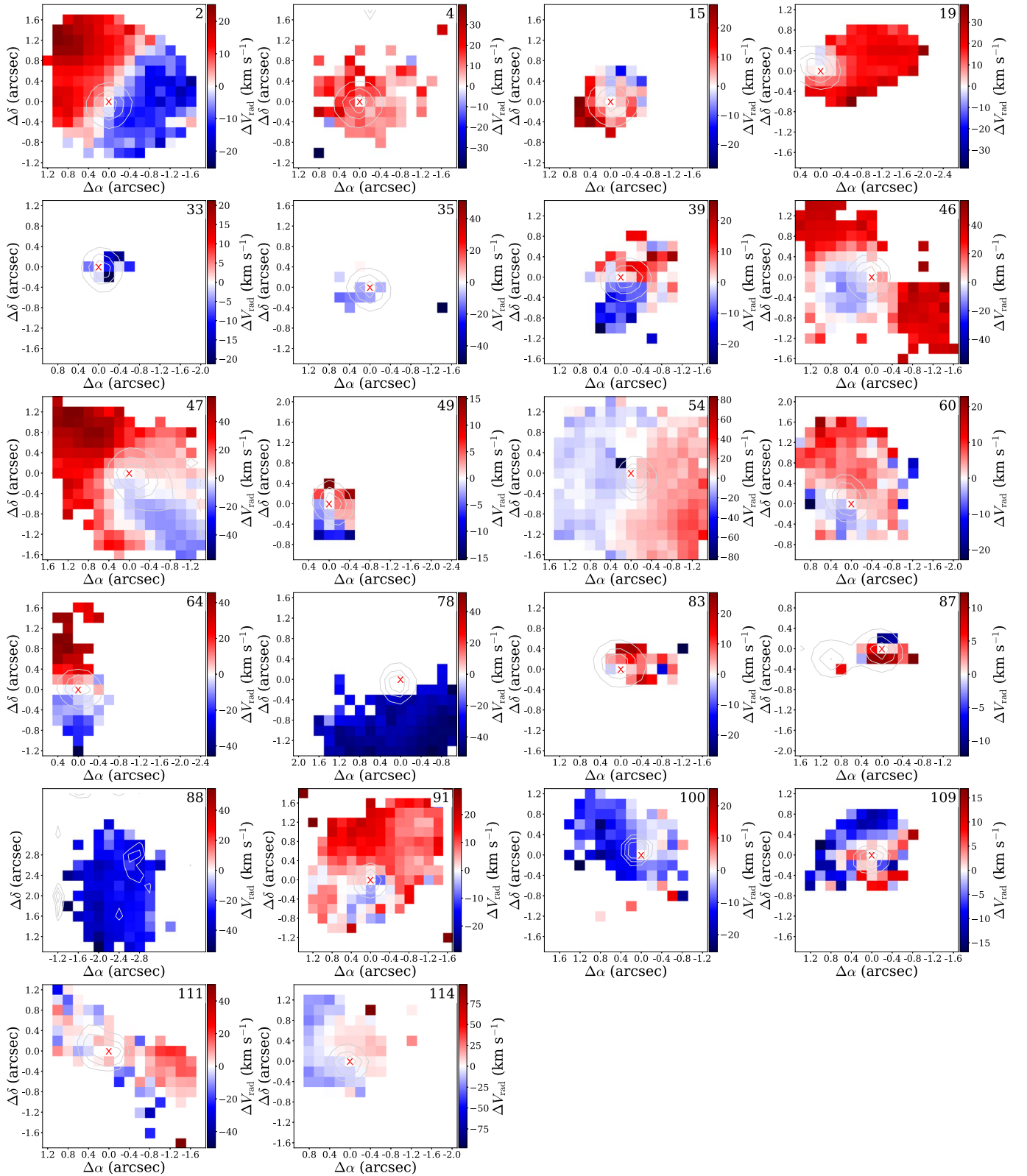


Figure 6. The H_2 1-0 S(1) velocity centroid maps for all YSOs associated with the H_2 emission; the velocities are calculated with respect to the radial velocity of the corresponding source. Only pixels with H_2 detections above 3σ are shown. The contours show the K -band continuum emission, and the red crosses the positions of the YSO candidates (the peak of the K -band continuum emission). The source names are indicated in the upper right corners. Radial velocities of the gas associated with sources No. 78 and 88 cannot be estimated, and here only the apparent radial velocities are shown. The KMOS spectral sampling at $2.12 \mu\text{m}$ corresponds to 39.67 km s^{-1} .

the CO absorption is detected in 43% of the sources, similar to the 57% detection rate in Connelley & Greene (2010), and >2.5 times more than in the Cooper et al. (2013) survey.

The CO bandhead in emission indicates high accretion rates onto the YSO disk, possibly also associated with an accretion burst (e.g., Lorenzetti et al. 2009; Guo et al. 2021).

Table 3
Accretion Properties of YSOs in CMa- ℓ 224

No.	$\text{Br}\gamma$ 10^{-16} (erg s $^{-1}$ cm $^{-2}$)	$\log(L_{\text{acc}})$ (L_{\odot})	$\log(\dot{M}_{\text{acc}})$ (M_{\odot} yr $^{-1}$)
2	13.00 ± 0.32	-1.30 $^{+0.76}_{-0.82}$...
3	13.89 ± 0.32	-1.26 $^{+0.72}_{-0.73}$...
5	-397.29 ± 0.55
6	19.08 ± 0.25	-1.09 $^{+0.79}_{-0.81}$...
9	341.80 ± 0.79	0.40 $^{+0.86}_{-0.86}$...
10	54.74 ± 0.45	-0.55 $^{+0.84}_{-0.86}$...
12	352.30 ± 1.35	0.41 $^{+0.89}_{-0.90}$...
13	28.33 ± 0.77	-0.89 $^{+0.79}_{-0.80}$...
15	521.01 ± 0.35	0.62 $^{+0.87}_{-0.88}$...
16	108.77 ± 1.57	-0.19 $^{+0.85}_{-0.87}$	-7.50 $^{+1.05}_{-1.07}$
18*	1.52 ± 0.34	-2.40 $^{+0.08}_{-0.10}$...
19	68.62 ± 0.21	-0.43 $^{+0.83}_{-0.84}$...
20	12.93 ± 0.85	-1.29 $^{+0.80}_{-0.84}$...
22*	1.63 ± 0.56	-2.36 $^{+0.13}_{-0.19}$...
23*	4.91 ± 1.36	-1.79 $^{+0.15}_{-0.19}$...
24	100.01 ± 0.29	-0.24 $^{+0.80}_{-0.80}$...
26	18.52 ± 0.33	-1.11 $^{+0.85}_{-0.93}$...
28	33.00 ± 0.60	-0.81 $^{+0.74}_{-0.75}$...
30	1.00 ± 0.20	-2.62 $^{+0.69}_{-0.74}$...
31*	1.16 ± 0.16	-2.54 $^{+0.02}_{-0.03}$...
32	27.83 ± 3.14	-0.90 $^{+0.82}_{-0.86}$...
33	17.17 ± 0.31	-1.15 $^{+0.80}_{-0.82}$...
34*	4.82 ± 0.34	-1.80 $^{+0.06}_{-0.06}$...
35	-20.72 ± 0.54
36A*	65.58 ± 2.41	-0.46 $^{+0.15}_{-0.15}$	-7.69 $^{+0.35}_{-0.35}$
38A*	2.36 ± 0.35	-2.17 $^{+0.06}_{-0.07}$...
38B*	0.36 ± 0.09	-3.15 $^{+0.03}_{-0.06}$...
39	33.48 ± 3.62	-0.80 $^{+0.88}_{-0.95}$	-8.10 $^{+1.08}_{-1.15}$
40	-2119.07 ± 12.85
41*	10.11 ± 0.59	-1.42 $^{+0.08}_{-0.08}$...
43	-1.29 ± 0.27
45	4.54 ± 0.27	-1.83 $^{+0.87}_{-1.09}$...
46	307.57 ± 5.92	0.34 $^{+0.86}_{-0.87}$	-6.97 $^{+1.06}_{-1.07}$
47	373.10 ± 0.37	0.44 $^{+0.86}_{-0.89}$...
48	1.37 ± 0.33	-2.45 $^{+0.73}_{-0.80}$...
49	119.13 ± 0.60	-0.15 $^{+0.87}_{-0.90}$...
50	94.51 ± 0.52	-0.27 $^{+0.78}_{-0.78}$...
52A*	2.38 ± 0.45	-2.17 $^{+0.08}_{-0.10}$...
52B*	1.56 ± 0.50	-2.39 $^{+0.12}_{-0.17}$...
53	-107.15 ± 0.76
54*	493.43 ± 19.10	0.59 $^{+0.24}_{-0.24}$...
55A	9.30 ± 1.35	-1.46 $^{+0.76}_{-0.79}$	-8.41 $^{+0.96}_{-0.99}$
56	19.69 ± 0.40	-1.08 $^{+0.82}_{-0.86}$...
57*	3.87 ± 0.93	-1.92 $^{+0.12}_{-0.15}$...
58	7.93 ± 1.03	-1.55 $^{+0.76}_{-0.79}$...
60	1163.21 ± 1.90	1.03 $^{+0.85}_{-0.87}$...
61	-3.22 ± 0.45
63	-34.89 ± 0.53
64	413.58 ± 0.40	0.50 $^{+0.71}_{-0.71}$...
68	2.63 ± 0.39	-2.12 $^{+0.76}_{-0.83}$...
71	-69.23 ± 0.25
72*	1.66 ± 0.58	-2.36 $^{+0.13}_{-0.20}$...
73	44.53 ± 0.30	-0.66 $^{+0.80}_{-0.81}$...
75	-58.02 ± 0.27
76	30.09 ± 0.38	-0.86 $^{+0.81}_{-0.84}$...
77	276.96 ± 0.21	0.29 $^{+0.85}_{-0.85}$...
79	9.33 ± 0.31	-1.46 $^{+0.75}_{-0.77}$	-8.48 $^{+0.95}_{-0.97}$
80*	2.65 ± 0.73	-2.11 $^{+0.12}_{-0.16}$...

Table 3
(Continued)

No.	$\text{Br}\gamma$ 10^{-16} (erg s $^{-1}$ cm $^{-2}$)	$\log(L_{\text{acc}})$ (L_{\odot})	$\log(\dot{M}_{\text{acc}})$ (M_{\odot} yr $^{-1}$)
81	65.21 ± 0.82	-0.46 $^{+0.87}_{-0.90}$	-7.74 $^{+1.07}_{-1.10}$
83	625.84 ± 0.35	0.71 $^{+0.78}_{-0.84}$...
84	-109.85 ± 0.87
85*	8.34 ± 0.50	-1.52 $^{+0.07}_{-0.08}$...
86B	1.10 ± 0.14	-2.57 $^{+0.68}_{-0.72}$...
89A*	0.81 ± 0.23	-2.72 $^{+0.07}_{-0.12}$...
89B*	0.24 ± 0.08	-3.36 $^{+0.04}_{-0.10}$...
91A*	-6.12 ± 1.11
91B*	6.90 ± 0.50	-1.62 $^{+0.07}_{-0.08}$...
92	-14.75 ± 0.51
93	115.79 ± 0.52	-0.16 $^{+0.83}_{-0.84}$...
94	-3.35 ± 0.25
96	-56.89 ± 0.71
97	29.29 ± 1.65	-0.87 $^{+0.84}_{-0.89}$...
98	4.91 ± 0.42	-1.80 $^{+0.73}_{-0.75}$...
99*	1.42 ± 0.25	-2.44 $^{+0.05}_{-0.07}$...
102	273.94 ± 3.28	0.28 $^{+0.84}_{-0.85}$...
104	-6.90 ± 0.81
109	716.77 ± 0.24	0.78 $^{+0.73}_{-0.73}$...
111	51.99 ± 0.37	-0.58 $^{+0.76}_{-0.76}$...
112A	9.55 ± 0.16	-1.45 $^{+0.71}_{-0.72}$...
112B	30.86 ± 0.14	-0.84 $^{+0.76}_{-0.76}$...
114	187.72 ± 0.76	0.09 $^{+0.97}_{-1.08}$	-7.06 $^{+1.17}_{-1.28}$
116	-3.91 ± 0.28
117	-4.64 ± 0.51
118	9.01 ± 0.43	-1.48 $^{+0.76}_{-0.78}$...

Notes. Negative flux values indicate absorption. Measurements for targets with asterisks have not been corrected for extinction. Flux uncertainties do not cover the extinction uncertainty of 10 mag, which is included in uncertainties of accretion luminosity and mass accretion rates. Uncertainties of $\log(L_{\text{acc}})$ and $\log(\dot{M}_{\text{acc}})$ do not include the systematic distance uncertainty.

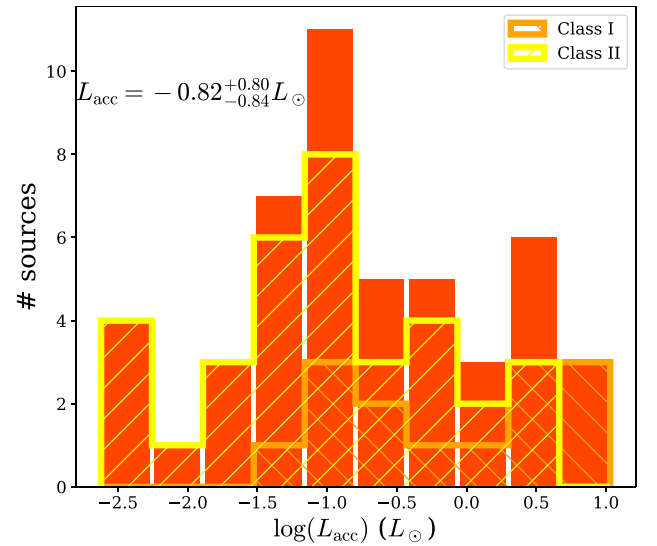


Figure 7. Histogram of the accretion luminosities (L_{acc}) based on $\text{Br}\gamma$ line luminosity (Table 3) measured toward YSOs in CMa- ℓ 224 (in dark orange). The median value of L_{acc} is indicated at the top of the plot. The orange and yellow hatched histograms show the distribution of L_{acc} for sources classified by Sewilo et al. (2019) as, respectively, Class I and Class II YSO candidates.

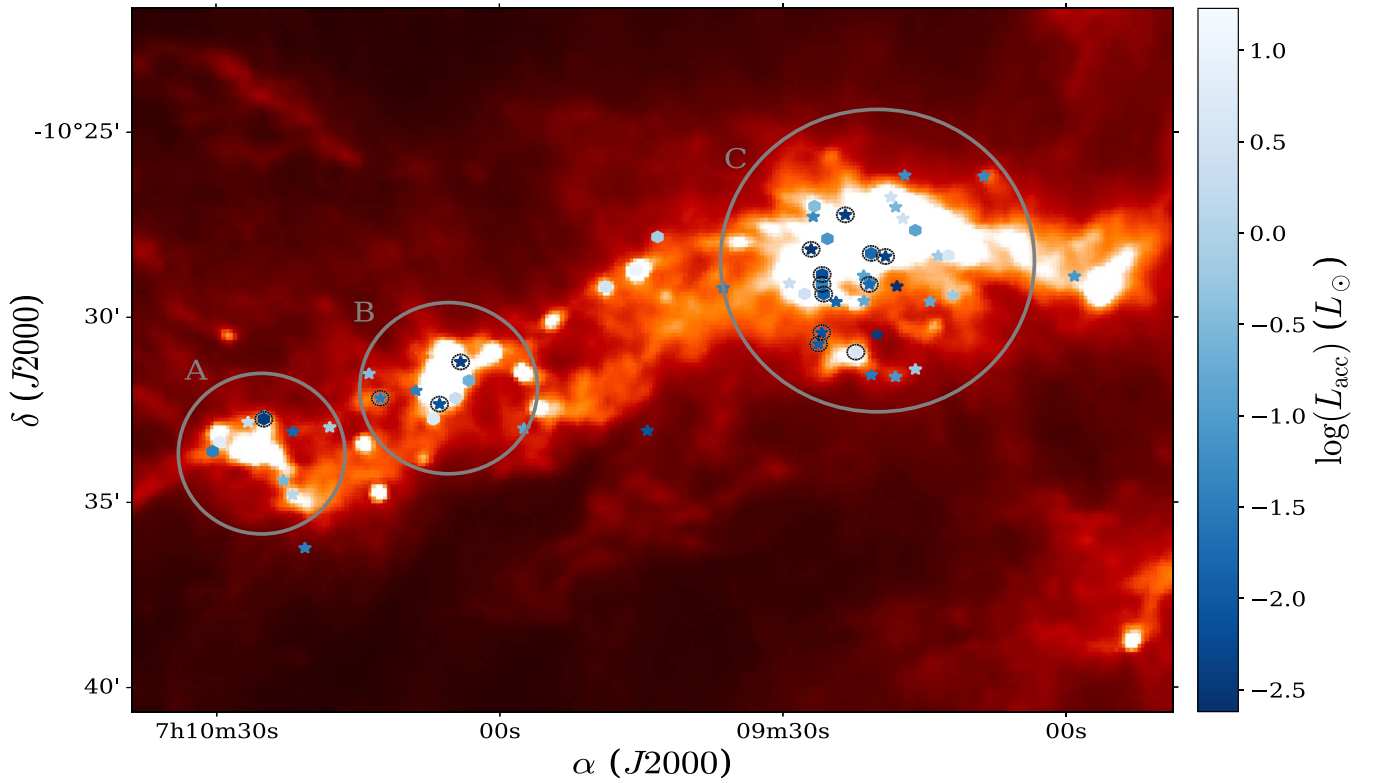


Figure 8. Distribution of accretion luminosity in the main filament in CMA- ℓ 224 (blue color scale). Class I sources are marked with hexagon and Class II sources with star symbols. Black circles mark targets without A_V estimation. The three regions identified by Sewilo et al. (2019) are marked with gray circles.

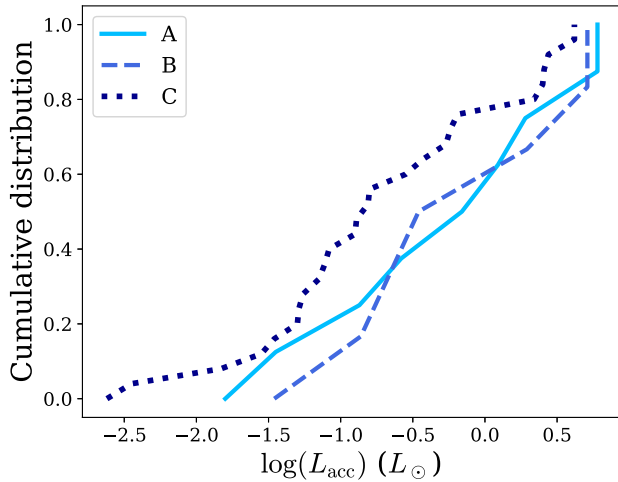


Figure 9. Cumulative distributions of accretion luminosities for clusters A (solid), B (dashed), and C (dotted line), as defined in Sewilo et al. (2019). Sources without A_V estimates are excluded.

The CO bandhead emission requires high temperatures (2500–4000 K) and densities ($n_H > 10^{10} \text{ cm}^{-3}$) to excite the upper levels (e.g., Carr 1989; Casali & Eiroa 1996). In CMA- ℓ 224, only 5% of the sources detected with KMOS show the CO bandhead in emission (4 Class I and 2 Class II YSOs). This detection rate is a factor of 4–5 lower than in the Carr (1989) and Connelley & Greene (2010) surveys, likely due their focus on Class I protostars. All of our sources with the CO bandhead emission also show the H_2 and $\text{Br}\gamma$ emission, and in four out of six sources the H_2 emission is extended, suggesting intensive mass accretion and subsequent ejection.

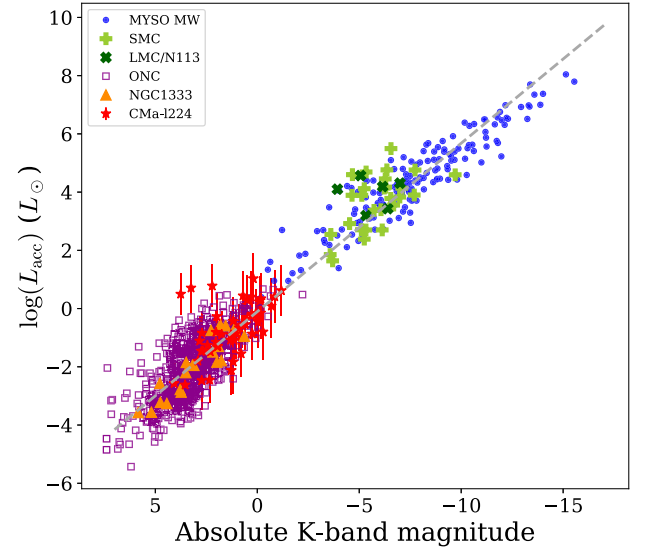


Figure 10. Accretion luminosity vs. absolute K -band magnitude. Red stars show YSOs in CMA- ℓ 224, blue circles show MYSOs (Cooper et al. 2013), light green “+” symbols show MYSOs from SMC (Ward et al. 2017), green crosses show MYSOs from LMC (Ward et al. 2016), violet open squares show YSOs in Orion (Manara et al. 2012), and orange triangles show low-mass YSOs in Perseus (Fiorellino et al. 2021). The dashed lines show linear fits separately for each of the data sets with the same colors. The gray line shows a linear fit to all data points. All luminosities have been corrected for extinction.

3.2.4. Other Lines

Spectra of 11 YSO candidates show multiple atomic lines, e.g., He I, Mg I, Ca I, Na I, K I, or Si I typical for late spectral types (K–M, Nisini et al. 2005); however, they do not reveal the presence of the $\text{Br}\gamma$, H_2 , and CO lines. The confirmation of

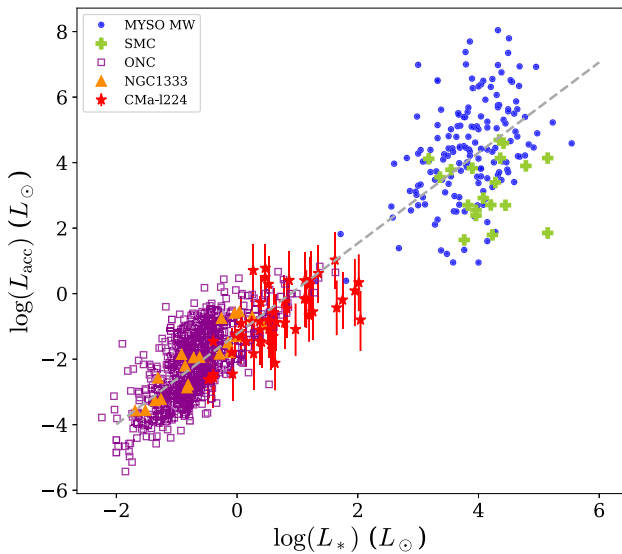


Figure 11. Accretion luminosity vs. star luminosity. The symbols are the same as in Figure 10. The dashed line shows a linear fit to the data. All luminosities have been corrected for extinction.

their YSO status would require careful spectral typing and further analysis, which will be presented in the future work in this series. Appendix B shows spectra of all those sources and the information about the detection of the key spectral lines.

3.3. Extinction

The line fluxes in the near-IR are affected by extinction. We adopt the values of A_V obtained from the spectral energy distribution (SED) modeling by Sewiło et al. (2019) for 85 sources in our sample. Our K -band observations cover several H_2 lines that are often used to estimate A_V ; however, after assessing the quality of our H_2 data, we decided against using this method, due to the small separation between the two lines ($\sim 0.2 \mu\text{m}$), uncertainty in telluric corrections near the Q-branch H_2 emission, and the small number of sources for which this method can be used.

We assess the uncertainty of extinction estimated from the SED fitting using the work by Furlan et al. (2016). There, the R statistics were used to calculate a mode—the value with the highest frequency within a certain range from the best-fit R value (see their Figure 48). Almost all their A_V uncertainties are consistent with a 1:1 correlation within a 10 mag error. We adopt this conservative value in the subsequent analysis, in particular in the calculation of the mass accretion (Section 3.5).

We note that extinction is expected to differ between the position of the infrared continuum source and the outflow (Yoon et al. 2022). The ratios of the hydrogen $\text{Br}\gamma$ and $\text{Pa}\alpha$ lines are routinely used to estimate A_V toward the accretion region (Fiorellino et al. 2021), but the latter line is located in the H -band and not covered by our observations. Because SED modeling provides the estimate of A_V toward the central star and H_2 emission is often extended, such an A_V estimate is likely not representative for the true reddening of the H_2 lines. Therefore, we do not apply it for those lines. Thus, Table 5 shows the H_2 line fluxes, which are not corrected for extinction.

3.4. Gas Spatial Distribution and Kinematics

The spatial distribution of the line emission varies significantly between different species detected with KMOS

(Figure 4). The $\text{Br}\gamma$ emission is spatially unresolved for the majority of the sources, in line with the origin in the inner disk. Similarly, the CO bandhead emission is also compact and cospatial with the continuum emission. In contrast to the $\text{Br}\gamma$ and CO bandhead emission, the H_2 emission is usually extended.

The extended distribution of the H_2 emission resembles the structure of the molecular outflows from Class 0/I protostars for 14 out of 33 sources with the H_2 line detection (42% or 11% of the entire sample; see Figure 4). In five sources, the extended H_2 emission is not associated with the targeted source (see Table 2) and likely originates from an outflow from another YSO. Those five cases often show only one lobe within the field of view. Among other sources with the detection of H_2 , the emission pattern does not show two prominent outflow lobes. The lack of the bipolar pattern might be due to insufficient spatial resolution or the projection effects. In general, a contribution from a photodissociation region is unlikely among the low-mass YSOs found in CMA- ℓ 224. The emission maps for the $\text{Br}\gamma$, H_2 , and CO bandhead lines for the entire KMOS YSO sample in CMA- ℓ 224 are presented in Appendix C.

We use the brightest and spectroscopically well-resolved H_2 line in K band, the 1-0 S(1) transition at $2.12 \mu\text{m}$, to calculate radial velocities of the emitting gas. Figure 5 shows selected channel maps for an example source (No. 47) associated with an extended H_2 emission. Here, the blueshifted emission transitions into a redshifted one on the other side of the central source, which is a clear signature of a bipolar ejection. The images reveal a velocity structure consistent with an outflow with velocities up to 50 km s^{-1} . A similar kinematic structure has been detected toward most of the other sources with the extended H_2 emission (Nos. 2, 15, 19, 46, 47, 54, 60, 64, 91, and 114; see Figure 6). The large spatial scales of those structures cannot be due to the emission from protoplanetary disks, because they are too cold at such large distances from the central star to excite H_2 .

The H_2 emission structure associated with sources No. 78 and 88 resembles the single outflow lobes; however, the continuum source is not seen in the map of the YSO candidate No. 88, while for No. 78, the H_2 emission does not seem to be physically connected to the source. Additional observations with a larger field of view are needed to identify sources responsible for the extended H_2 emission in these fields.

The estimated relative velocities do not exceed $\sim 50 \text{ km s}^{-1}$, with velocities increasing toward lobe ends, typical for outflow-driven shock waves. The moderate spectral resolution of KMOS does not allow for a detailed study on outflow kinematics, including any minor variations in kinematic patterns. The spatial extent of the H_2 gas supports the origin in outflow shocks. The limited wavelength coverage of our spectra, however, does not allow us to properly estimate extinction as a function of position along the outflow (see Section 3.3).

Finally, we note that the bipolar structure in several H_2 lines toward source No. 47 (Appendix C) is consistent with its classification as a Class I source using SED models (Sewiło et al. 2019). The prominent H_2 outflow suggests that the source might be one of the youngest in our sample. It would be a suitable candidate for a detailed spectral modeling using shock models; however, this is outside of the scope of this paper.

3.5. Gas Accretion

Gas accretion onto Class II YSOs is typically measured using UV continuum excess or line emission in e.g., H, He, or Ca II at optical wavelengths (e.g., Alcalá et al. 2014; Nisini et al. 2018). In more embedded Class I YSOs, the accretion is more often quantified using hydrogen lines in the near-IR, which are less affected by dust extinction (Muzerolle et al. 1998; Natta et al. 2004).

We estimate the accretion luminosity (L_{acc} in units of L_{\odot}) for YSOs in CMA- ℓ 224 by measuring the flux of the hydrogen Br γ line. As illustrated in Figure 3, the Br γ emission arises from the same area as the continuum source; we therefore assume it traces primarily the unresolved accretion region (see also Section 3.2.1). We use the relation between $L_{\text{Br}\gamma}$ and L_{acc} for low- and intermediate-mass YSOs from Alcalá et al. (2017) to estimate L_{acc} :

$$\log(L_{\text{acc}}) = (1.19 \pm 0.10) \cdot \log L_{\text{Br}\gamma} + (4.02 \pm 0.51). \quad (1)$$

The mass accretion rates, \dot{M}_{acc} , are then calculated using the formula:

$$\dot{M}_{\text{acc}} = L_{\text{acc}} \times \left(1 - \frac{R_*}{R_{\text{in}}}\right)^{-1} \frac{R_*}{GM_*}, \quad (2)$$

where R_* and M_* are the stellar radius and mass, respectively, and R_{in} is the inner-disk radius; typically, R_{in} is assumed to equal $5R_*$ (Gullbring et al. 1998). Although the relation was found for Class II objects, it is a specific case of the general formula describing efficiency of converting kinetic energy of falling matter onto a stellar photosphere into radiation and can be applied to Class I sources as well (see the review of Hartmann et al. 2016 or the recent paper by Fiorellino et al. 2022).

To calculate the mass accretion rates, knowledge of stellar masses and radii is needed. Stellar parameters for 17 sources from our sample have been estimated from the SED fitting¹⁸ (Sewiło et al. 2019); only half of them are associated with the Br γ emission. The typical masses are $\sim 2 M_{\odot}$ and the typical radii are $\sim 3 R_{\odot}$. The median logarithm of the accretion luminosity is $-0.82^{+0.80}_{-0.84} L_{\odot}$, and the median logarithm of the accretion rate is $-7.92^{+1.06}_{-1.09} M_{\odot} \text{ yr}^{-1}$ for sources with A_V estimates.

All accretion luminosities, and where available, mass accretion rates and associated uncertainties, are listed in Table 3. The uncertainties of mass accretion rates account for the uncertainties in line fluxes, $L_{\text{Br}\gamma}$ - L_{acc} relation, extinction (A_V of 10 mag, corresponding to ~ 1 mag in K -band), and 0.1 dex for both M_* and R_* . We do not include, however, the uncertainty of the distance to the region, which is systematic. The adopted value of 0.92 kpc from Sewiło et al. (2019) is consistent with those from stellar studies (1.05 ± 0.15 kpc, 0.99 ± 0.05 kpc, and 1.15 ± 0.06 kpc in Shevchenko et al. 1999, Kaltcheva & Hilditch 2000, and Lombardi et al. 2011, respectively), and recent estimates using ALMA observations (a median of 0.92 kpc for cores within our pointings; Olmi et al. 2023).

¹⁸ The spatial resolution of SED data points does not allow us to resolve visually multiple systems on the KMOS maps. We therefore adopted the same stellar parameters for the two stars in a binary candidate, source 55 (Sewiło et al. 2019). Proper characterization of binaries is beyond the scope of this paper.

We also cross-checked the distance to CMA- ℓ 224 with the results from the 3D dust maps using photometry from Pan-STARRS 1 and 2MASS, as well as the Gaia parallaxes¹⁹ (Green et al. 2019). The median distance estimated this way for several targets in our study yields 1.26 kpc. The value exceeds our adopted distance of 0.92 kpc, with a difference that is larger than the uncertainties of previous studies and the dispersion of individual distance values. Thus, we consider 0.34 kpc as the uncertainty of the distance; it corresponds to the uncertainty of 0.27 dex in accretion luminosity and mass accretion rate.

Figure 7 shows the distribution of accretion luminosities among Class I and II YSOs, which range from -2.5 to $0.6 L_{\odot}$ in logarithm. The distributions of L_{acc} are similar for both Class I and II YSOs, but the number of Class II YSOs in this sample is 2 times higher than Class I YSOs. We do not find any correlation between accretion luminosity and stellar mass, but the number of mass measurements is too small and the mass measurements are too uncertain to draw reliable conclusions. Accretion rate estimations are feasible only for eight Class II YSOs (including one binary candidate) with available mass and radius estimates; their logarithmic values range from -8.4 to $-7.0 M_{\odot} \text{ yr}^{-1}$.

4. Discussion

4.1. Star Formation in CMA- ℓ 224

Star formation in Canis Majoris is closely linked with a supernova explosion ~ 1.5 Myr ago (Herbst & Assoua 1977; Comeron et al. 1998). The expanding shell, coincident with CMA- ℓ 224, might have compressed the interstellar medium in a turbulent flow and triggered the filament formation (Fischer et al. 2016; Sewiło et al. 2019). The main filament in the region is highly supercritical (Olmi et al. 2016), which leads to gravitational fragmentation and the formation of clumps and cores (André 2017). Overall, the filament is associated with ~ 700 starless cores and ~ 250 prestellar cores (Elia et al. 2013), and the largest concentration of Class I YSOs in the entire Canis Major star-forming region (Fischer et al. 2016; Sewiło et al. 2019).

Integral Field Spectroscopy in K band at high angular resolution provides unique insights into star formation processes on scales of individual YSOs in the main filament of CMA- ℓ 224. As shown in Section 3, the compact emission in the Br γ line traces the ongoing accretion onto the young stars, whereas the spatial distribution and kinematics of H $_2$ pinpoint molecular outflows and mass ejection. The question remains: to what extent are the mass accretion and ejections rates in YSOs linked with the properties of the filament and its possible evolution?

Figure 8 shows the distribution of accretion luminosity in the main filament in CMA- ℓ 224 (Section 3.5). YSOs are preferentially located within three “clusters” associated with bright far-IR continuum emission. Following the nomenclature introduced in Sewiło et al. (2019), cluster C is known to coincide also with C¹⁸O 2-1 emission and the peak of ¹³CO 1-0, with the latter encompassing the entire filament (Olmi et al. 2016). The ¹³CO and C¹⁸O line observations revealed a velocity gradient along the main filament, which extends from cluster C to A (Olmi et al. 2016) and is likely responsible for the formation of YSOs at the ridge connecting clusters B and C. Another

¹⁹ See the interactive web interface at <http://argonaut.skymaps.info/>.

velocity gradient was identified from a secondary filament that is roughly perpendicular to the main one at the position of cluster B (Olmi et al. 2016). Sewiło et al. (2019) suggest that this smaller filament has provided the molecular gas reservoir necessary to initiate the star formation for cluster B, as evidenced by the most evolved YSO population in this cluster.

To investigate this scenario, we calculate cumulative distributions of accretion luminosities, L_{acc} , for the three clusters (Figure 9). The distributions of accretion luminosity are similar for clusters A and B, whereas cluster C seems to be shifted toward lower values. The observed similarity between the accretion distributions of clusters A and B is confirmed by the two-sample Kolmogorov–Smirnov (K-S) test that yields a statistic of 0.2 and p -value of 0.99. The K-S test for clusters A and C, and clusters B and C, yield statistics of 0.30–0.35 and p -values of 0.55–0.47, not allowing us to statistically distinguish the two distributions. The median accretion luminosities also gradually increase from Cluster C ($-0.89 \log(L_{\odot})$) to B ($-0.56 \log(L_{\odot})$) and A ($-0.37 \log(L_{\odot})$). Higher accretion rates are expected from less evolved stars, assuming similar masses. Thus, the evolutionary stages of Clusters A and B could be earlier than those of Cluster C, contrary to earlier works (Sewiło et al. 2019).

However, the distributions can be affected by the number of targets within the Clusters, i.e., the small number of statistics. Adopting the YSO classification from Sewiło et al. (2019), Cluster C contains five Class I YSOs and 20 Class II YSOs for which we calculated accretion luminosities. In Cluster A, we measured L_{acc} in two Class I and six Class II YSOs. Similarly, in Cluster B, three Class I and three Class II YSOs have accretion estimates. Thus, Cluster C contains significantly more YSOs with measured accretion luminosities (25) than the two other clusters combined (14). As a result, it has the most representative sample of sources, characterized by a broad range of accretion properties.

4.2. A Possible Impact of Low Metallicity

Observations of star formation in external galaxies suggest that subsolar metallicity has a clear impact on the physical and chemical conditions in molecular clouds (e.g., Madden et al. 2013; Roman-Duval et al. 2014). In particular, a lower dust content in the low-metallicity environments reduces the shielding from ultraviolet radiation and translates to a decrease of molecular abundances due to photodissociation (“CO-dark gas”; see, e.g., Wolfire et al. 2010). The formation rate of molecules on the dust grains also decreases, which is the main reason for the reduction of H_2 abundances in the low-metallicity clouds (Glover & Clark 2012).

The Large and Small Magellanic Clouds, with Z of ~ 0.3 – $0.5 Z_{\odot}$ (LMC; Russell & Dopita 1992; Westerlund 1997; Rolleston et al. 2002) and $0.2 Z_{\odot}$ (SMC; Russell & Dopita 1992), are routinely used as laboratories for studying star formation in low-metallicity environments. Observations show a decrease of molecular gas cooling in YSO envelopes, UV radiation penetrating deeper into the clouds, and an increase in average dust temperatures with respect to those in local star-forming regions (e.g., van Loon et al. 2010a, 2010b; Oliveira et al. 2019). However, the distances of 50.0 ± 1.1 kpc (LMC, Pietrzyński et al. 2013) and 62.1 ± 2.0 kpc (SMC, Graczyk et al. 2014) hinder characterization of individual low-mass YSOs.

The outer Galaxy also consists of star-forming regions with subsolar metallicities, and so offers the opportunity to study the impact of low metal content on star formation (Sodroski et al. 1997). The metallicity of CMa- ℓ 224 has not been measured, so here we adopt the O/H Galactocentric radial gradients obtained from the observations of HII regions across the Milky Way. Depending on the adopted survey, the metallicity of CMa- ℓ 224 would be 0.55 – $0.58 Z_{\odot}$ (Esteban & García-Rojas 2018), $0.68 Z_{\odot}$ (Fernández-Martín et al. 2017), or 0.67 – $0.73 Z_{\odot}$ (Balsler et al. 2011). The O/H and Fe/H gradients obtained using the observations of Cepheids suggest much higher metallicities of 1.11 – $1.17 Z_{\odot}$ (Maciel & Andrievsky 2019) or 1.13 – $1.27 Z_{\odot}$ (Luck & Lambert 2011), yet they are not representative for star-forming regions. Therefore, we assume that the metallicity of CMa- ℓ 224 is intermediate between the metallicity of the LMC and the metallicity in the solar neighborhood.

A possible effect of metallicity on YSO accretion has been investigated in the LMC and SMC based on the near-IR observations of massive YSOs (Ward et al. 2016, 2017) and optical observations with $\text{H}\alpha$ in YSOs with a wide range of masses (De Marchi et al. 2011, 2017; Biazzo et al. 2019). The $\text{Br}\gamma$ luminosities for Magellanic YSOs seem higher than those found in the Galactic high-mass YSOs from the rms survey for the same absolute magnitudes (Cooper et al. 2013). Here, we extend the measurements toward lower-mass YSOs, which are located in CMa- ℓ 224 and more nearby star-forming regions (Figures 10 and 11). We adopt the same empirical relations between the $\text{Br}\gamma$ luminosity and accretion luminosities for various samples (Alcalá et al. 2017); however, L_{acc} from Orion has been calculated using $\text{H}\alpha$ and two-color diagrams (Manara et al. 2012). The K -band magnitudes of YSOs from Orion are adopted from Robberto et al. (2010).

Figures 10 and 11 show the increase of L_{acc} with both the absolute K -band magnitude and L_{*} , with the YSOs from CMa- ℓ 224 located between the least massive YSOs in the NGC 1333 cluster in Perseus (Fiorellino et al. 2021) and in Orion (Manara et al. 2012), and the high-mass YSOs both in the Milky Way (Cooper et al. 2013) and the Magellanic Clouds (Ward et al. 2016, 2017). The Pearson coefficient of $|r| = 0.96$ (30σ) is obtained for the absolute K -band magnitude versus L_{acc} relation, reflecting a strong correlation (Figure 10). Similarly, the Pearson coefficient of $|r| = 0.93$ (30σ) characterizes the L_{*} versus L_{acc} relation.

Accretion luminosities in CMa- ℓ 224 are consistent with those in the solar neighborhood (e.g., Perseus and Orion) and do not show a clear enhancement of accretion luminosity expected in the low-metallicity environments (Ward et al. 2016, 2017). Most of the $\text{Br}\gamma$ emitters are, however, Class II sources, characterized by lower L_{acc} with respect to less evolved, Class I sources. The metallicity of CMa- ℓ 224 (~ 0.6 – $0.7 Z_{\odot}$; Balsler et al. 2011; Fernández-Martín et al. 2017; Esteban & García-Rojas 2018) might be too similar to that of the solar neighborhood to exhibit a clear, measurable difference in accretion properties. Follow-up observations of additional clouds in the outer Galaxies, spanning a broad range of metallicities and sufficient number of sources, would be critical in order to draw robust conclusions about the impact of the lower metallicity on accretion rates in the outer Galaxy.

5. Conclusions

We presented VLT/KMOS near-IR spectroscopy of YSOs in CMa- ℓ 224, illustrating the instrument capability to study

low-mass star formation, and where applicable, to detect molecular outflows in the outer Galaxy. We summarize the findings as follows:

1. The Br γ line is detected in emission toward 47% and in absorption toward 13% of the sources. The H₂ 1-0 S(1) line is detected on-source in 33 sources, including 27 sources where the emission is extended. The CO bandhead at 2.3 μ m is detected in emission in 5% of YSOs and in absorption in 60% of YSOs.
2. The extent and velocity structures of H₂ emission suggest an origin of the emission in outflows and shocks. Follow-up observations are necessary, however, to estimate the extinction along the outflows.
3. We find a gradual increase in accretion luminosities from Cluster C to A and B with median values of -0.89 , -0.56 , and $-0.37 \log L_{\odot}$, respectively. Cluster C might be the most evolved part of CMa- ℓ 224.
4. Accretion luminosities do not show the impact of subsolar metallicity in the CMa- ℓ 224. It is likely due to insufficient difference in metallicity between the region and the solar neighborhood.

Large-scale Galactic surveys, such as the Outer Galaxy High Resolution Survey (Colombo et al. 2021), are starting to provide a complete census of molecular clouds and star-forming filaments spanning a range of metallicities. IFU observations of YSOs in those regions, either with ground-based facilities or the James Webb Space Telescope, will be critical to confirm the impact of metallicity on low-mass star formation within our Galaxy.

Acknowledgments

The authors thank the referee for a careful reading of the manuscript. D.I., A.K., M.K., and N.L. acknowledge support

from the First TEAM grant of the Foundation for Polish Science No. POIR.04.04.00-00-5D21/18-00. This work was supported by the Polish National Science Center grants 2014/15/B/ST9/02111 and 2016/21/D/ST9/01098. The material is based upon work supported by NASA under award number 80GSFC21M0002 (M.S.). This article has been supported by the Polish National Agency for Academic Exchange under grant Nos. PPI/APM/2018/1/00036/U/001 and BPN/BEK/2021/1/00319/DEC/1. D.I. was partly funded by the European Research Council (ERC) via the ERC Synergy Grant *ECOGAL* (grant 855130). The research of LEK is supported by a research grant (19127) from VILLUM FONDEN. G.J.H. is supported by general grant 12173003 awarded by the National Natural Science Foundation of China. W.R.M.R. thanks the Leiden Observatory for providing financial support. Based on observations made with ESO Telescopes at the La Silla Paranal Observatory under program ID 0102.C-0914(A).

Facility: VLT:Antu.

Software: astropy²⁰ (Astropy Collaboration et al. 2013; Price-Whelan et al. 2018), matplotlib²¹ (Hunter 2007), numpy²² (Oliphant 2006; Van Der Walt et al. 2011), esorex,²³ KARMA.²⁴

Appendix A KMOS K-band Continuum Maps

Figure A1 shows the K-band continuum flux density maps for YSO candidates in CMa- ℓ 224 without stellar companions. Similar maps for the fields with the detection of two sources (the binary star candidates) are shown in Figure 2. Figure A2 shows the integrated continuum maps for YSO candidates with the very weak K-band continuum.

²⁰ <http://www.astropy.org>

²¹ <https://matplotlib.org/>

²² <https://numpy.org/>

²³ <https://www.eso.org/sci/software/cpl/esorex.html>

²⁴ <https://www.eso.org/sci/observing/phase2/SMGuidelines/KARMA.html>

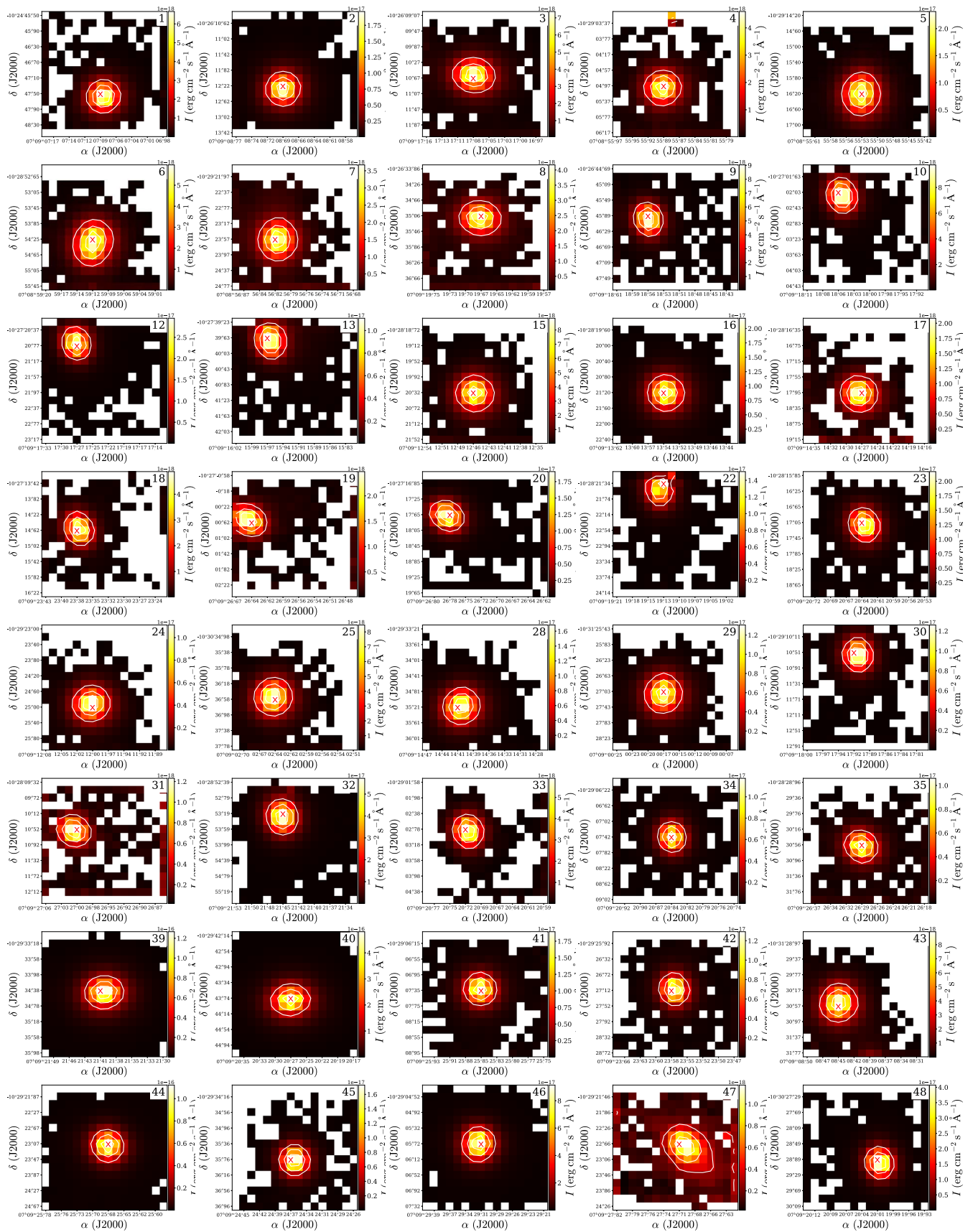


Figure A1. KMOS K -band continuum maps for single YSO candidates. Source names are provided in the upper right corners (No. in Table 2). The contour levels are 0.25, 0.5, and 0.75 \times the K -band continuum peak. Only pixels with a continuum flux density above 3σ are shown.

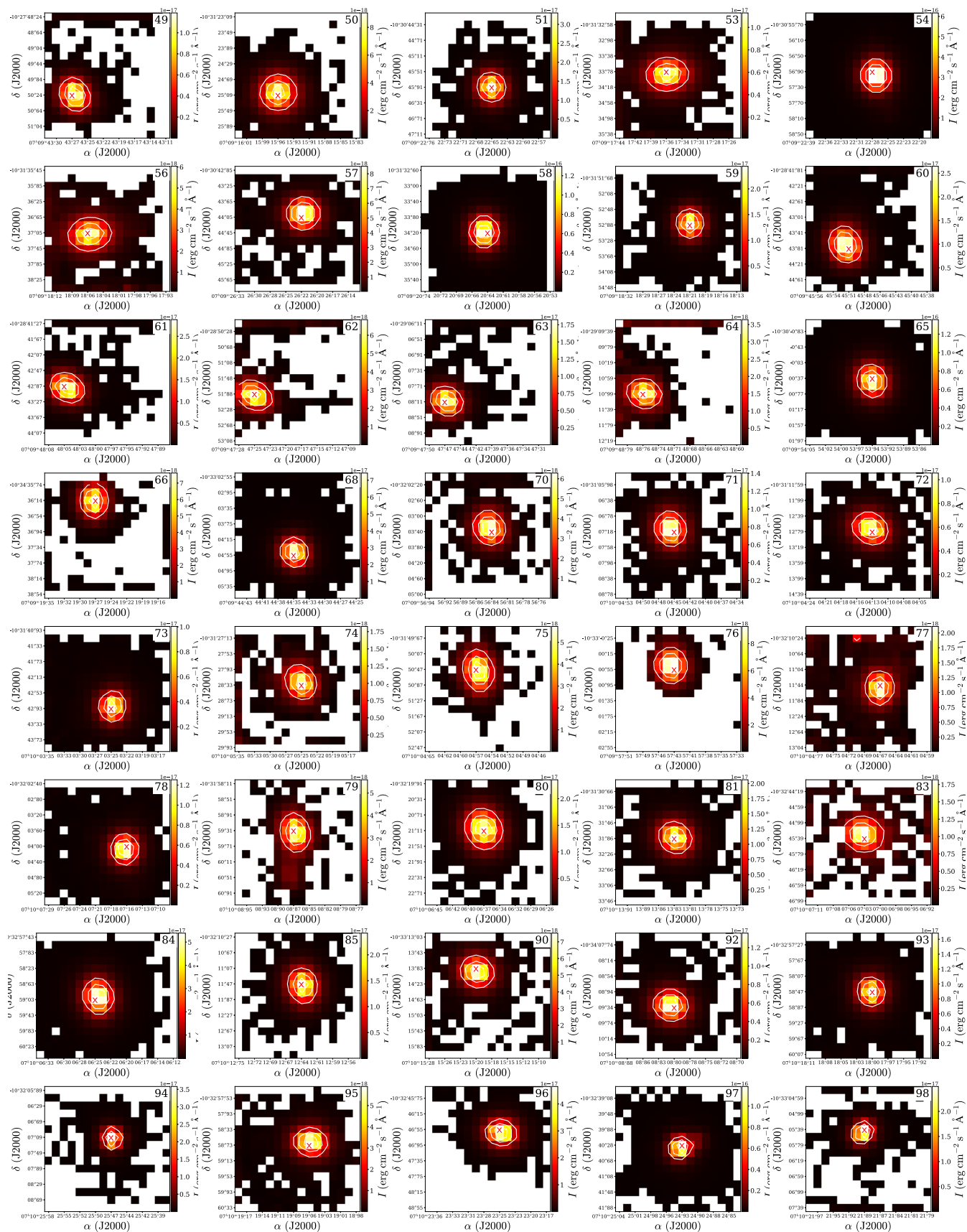


Figure A1. (Continued.)

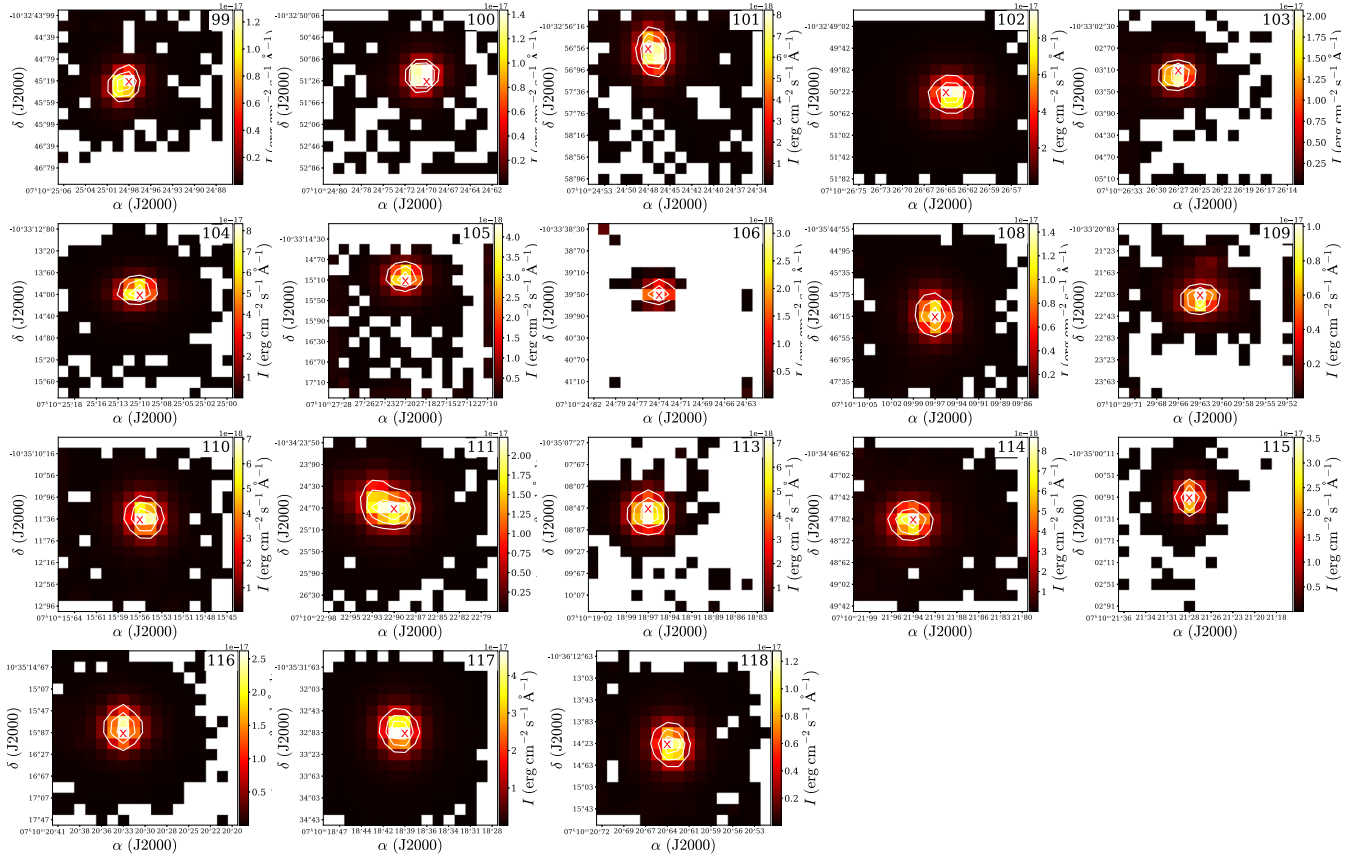
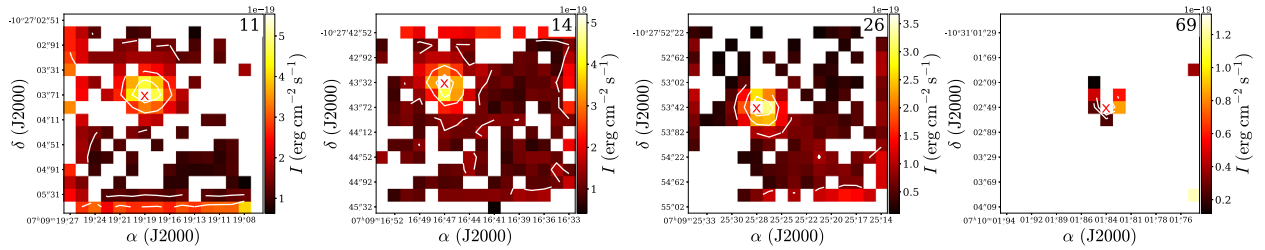


Figure A1. (Continued.)


 Figure A2. Similar to Figure A1, but for the faintest sources in the sample: Nos. 11, 14, 26, and 69 (see Table 2). The continuum was integrated over the entire K -band spectrum in every pixel to increase the signal-to-noise ratio.

Appendix B Spectra

Figures B1–B10 show the K -band spectra of all YSO candidates in CMA- ℓ 224 observed with KMOS. The spectra are presented in subgroups having similar characteristics—line detections and their profiles. In particular, Figure B1 shows spectra of sources with the $\text{Br}\gamma$ line in emission, as represented by source No. 12 in Figure 3. Figure B2 presents spectra of sources with detections of both the $\text{Br}\gamma$ and H_2 at $2.12\ \mu\text{m}$ lines in emission, but a lack of the CO bandhead emission. Figure B3 shows spectra of two sources with strong H_2 emission from outflows, but a lack of the $\text{Br}\gamma$ or CO bandhead lines. Figure B4 shows spectra of three sources with the $\text{Br}\gamma$ and H_2 lines in emission, and the CO bandhead lines in absorption. Figure B5 features spectra of presumably more evolved objects without the

H_2 emission lines, but with the $\text{Br}\gamma$ line in emission and the CO bandhead lines in absorption. Figure B6 shows spectra of sources with the H_2 emission and the CO bandhead absorption lines, but a lack of the $\text{Br}\gamma$ emission. Figure B7 shows spectra of sources with detections of $\text{Br}\gamma$ in absorption, and Figure B8, the only five single sources with spectra characterized by the CO bandhead in emission. Figure B9 shows spectra of sources with CO in absorption, but nondetections of the H_2 or $\text{Br}\gamma$ lines. Finally, Figure B10 shows spectra of YSO candidates that do not show any signatures of accretion or ejection, and which require follow-up observations to confirm their status.

Spectra of the individual components of the binary YSO candidates are presented in Figure B11–B12. While all spectra of single objects were extracted from the spectral cubes within the aperture of radius of 3 pixels, due to their proximity, a different approach has been followed for double stars. For the

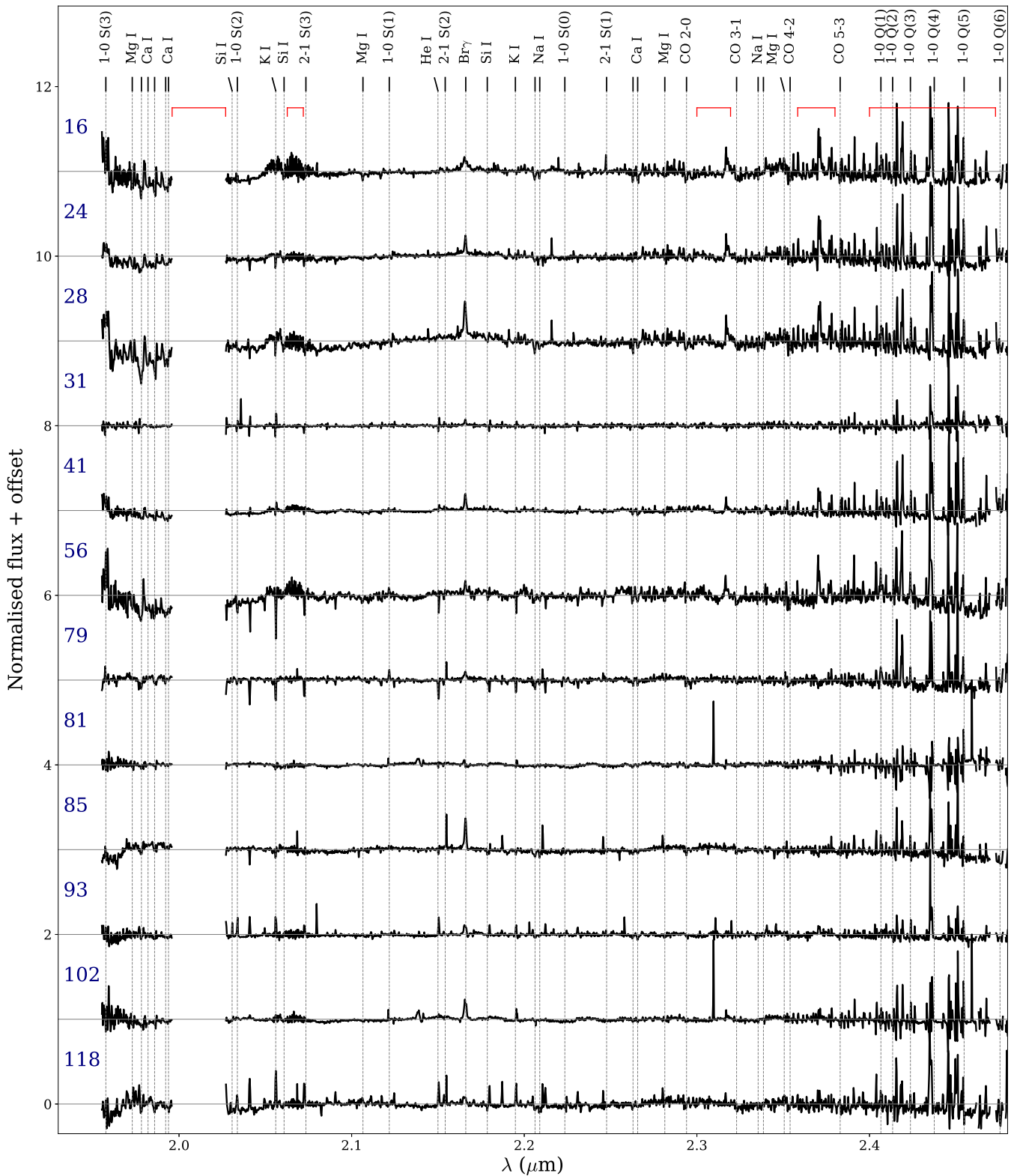


Figure B1. *K*-band spectra of YSO candidates in the CMa-ℓ224 star-forming region, which show the H Br γ line in emission. All spectra are continuum subtracted and normalized to the peak flux density in the range from 1.97 to 2.47 μm . Red horizontal lines show spectral ranges most affected by telluric lines; the range at 2.0 μm has been removed for clarity.

most distant pairs (sources No. 21, 38, 38, 86, and 87), the same aperture radius was used. For sources No. 82, 91, and 112, we used the radius of 2 pixels. To maximize the collected signal, we used the radius of 1.5 pixels for pairs No. 52 and 55. Spectra of the barely resolved binary, source No. 89, were

extracted using the 1 pixel radius. Their signal can be contaminated.

Table 4 provides an inventory of the key line detections in all sources, while Table 5 lists the measured H₂ line fluxes not corrected for extinction. We include only detections above 3 σ .

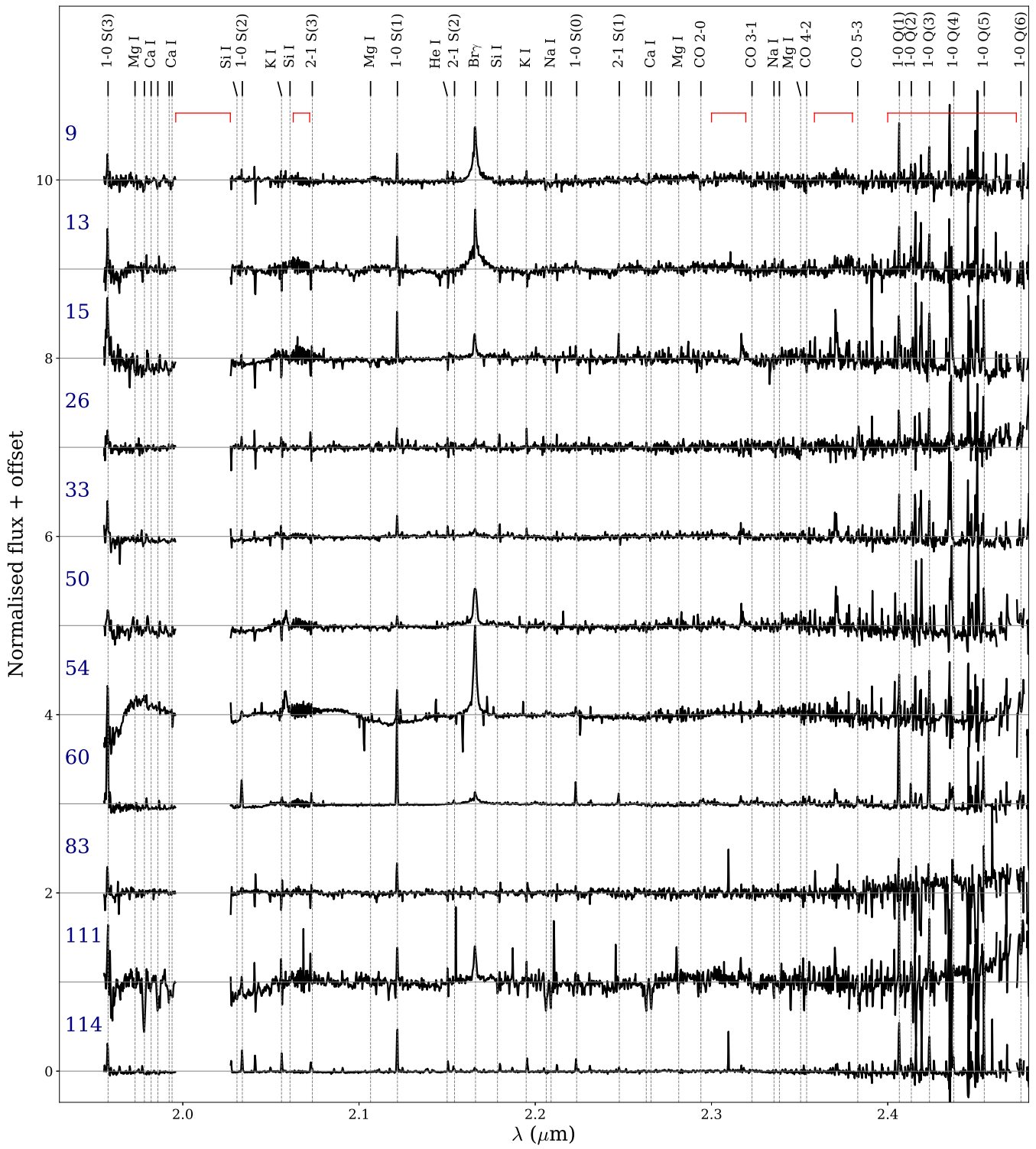


Figure B2. Spectra with Br γ and H $_2$ emission lines.

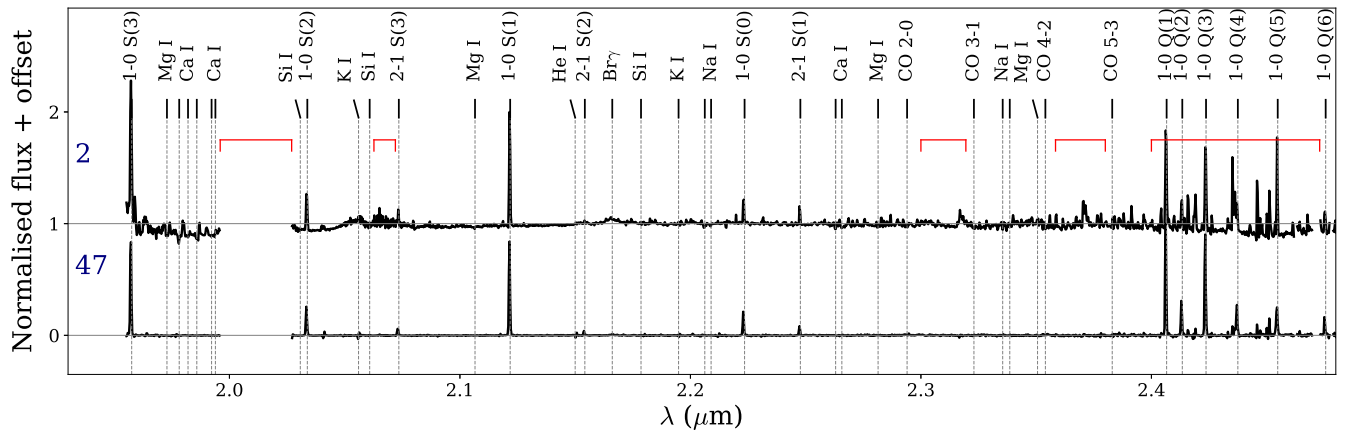


Figure B3. Spectra with only H₂ emission lines.

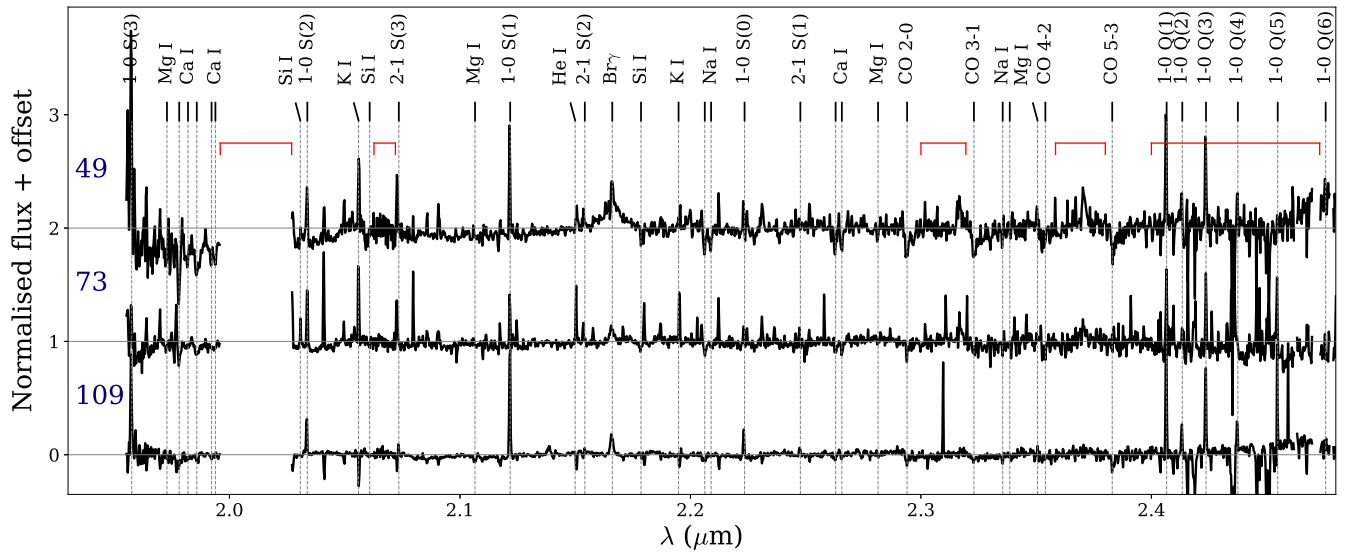


Figure B4. Spectra with Br_γ and H₂ emission lines and CO bandhead in absorption.

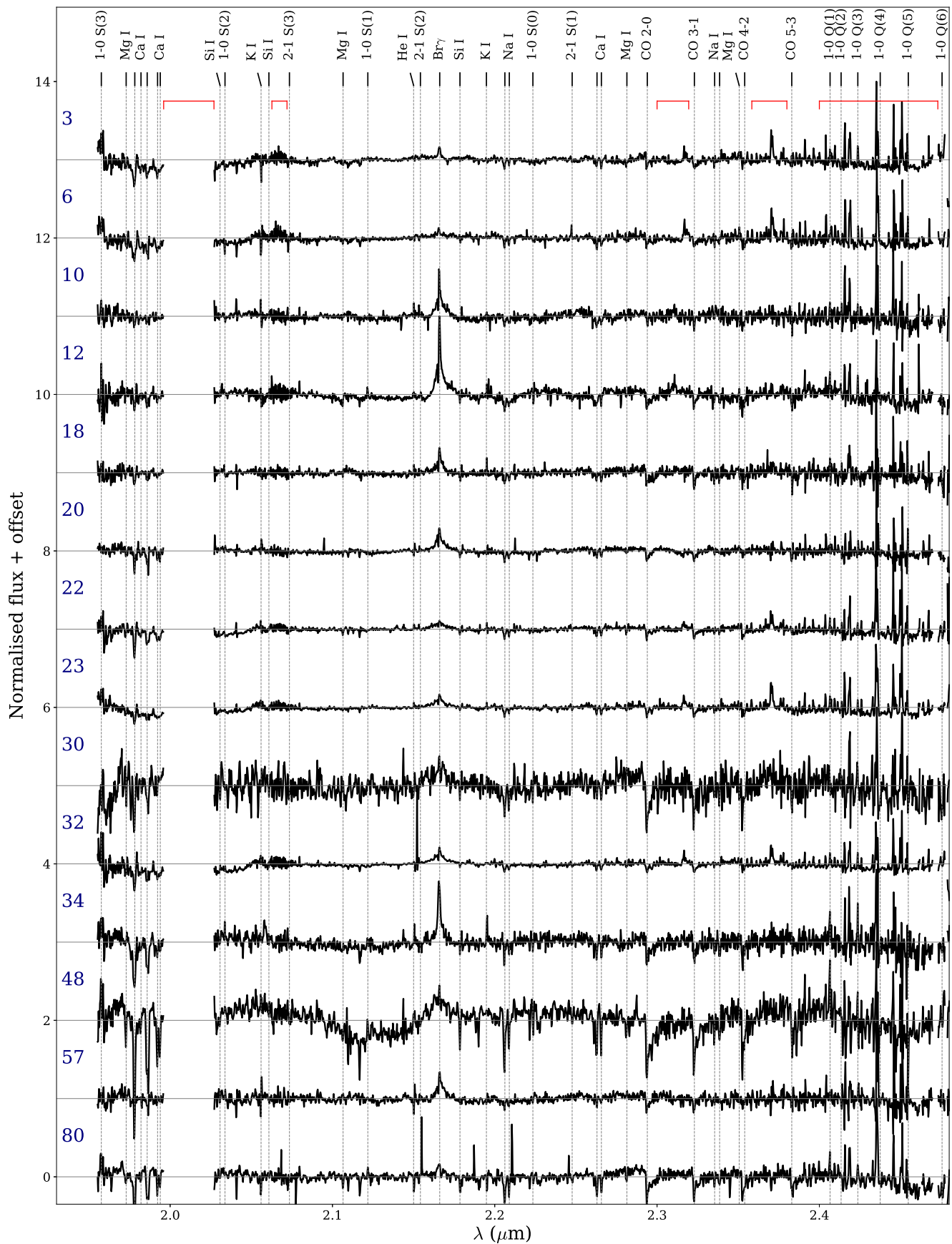


Figure B5. Spectra with Br γ emission line and CO bandhead in absorption.

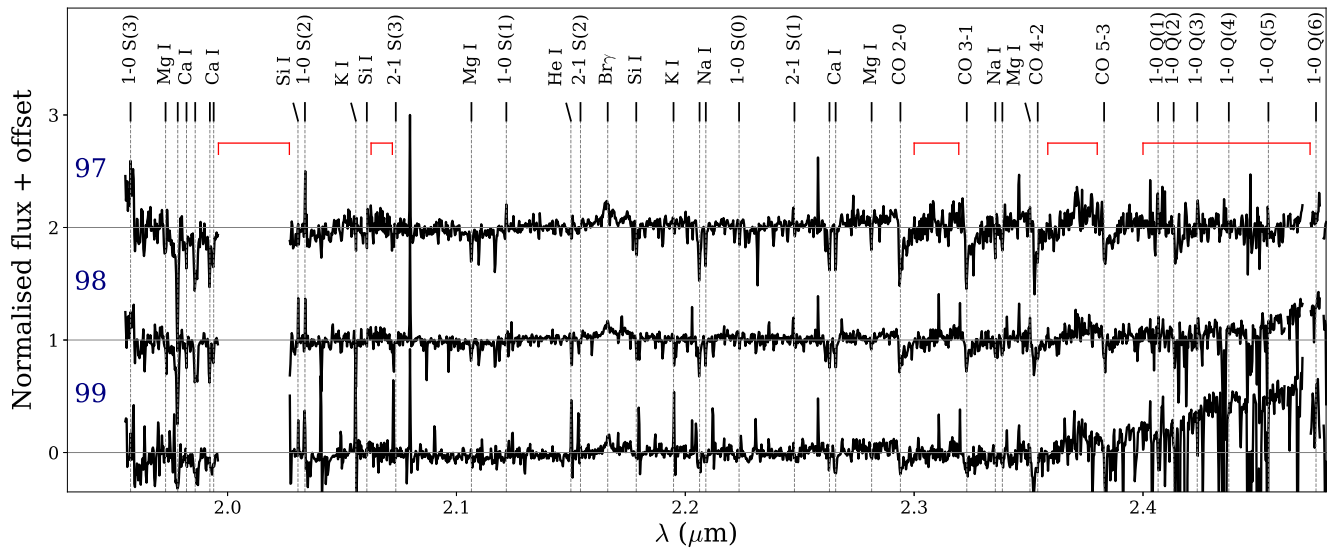


Figure B5. (Continued.)

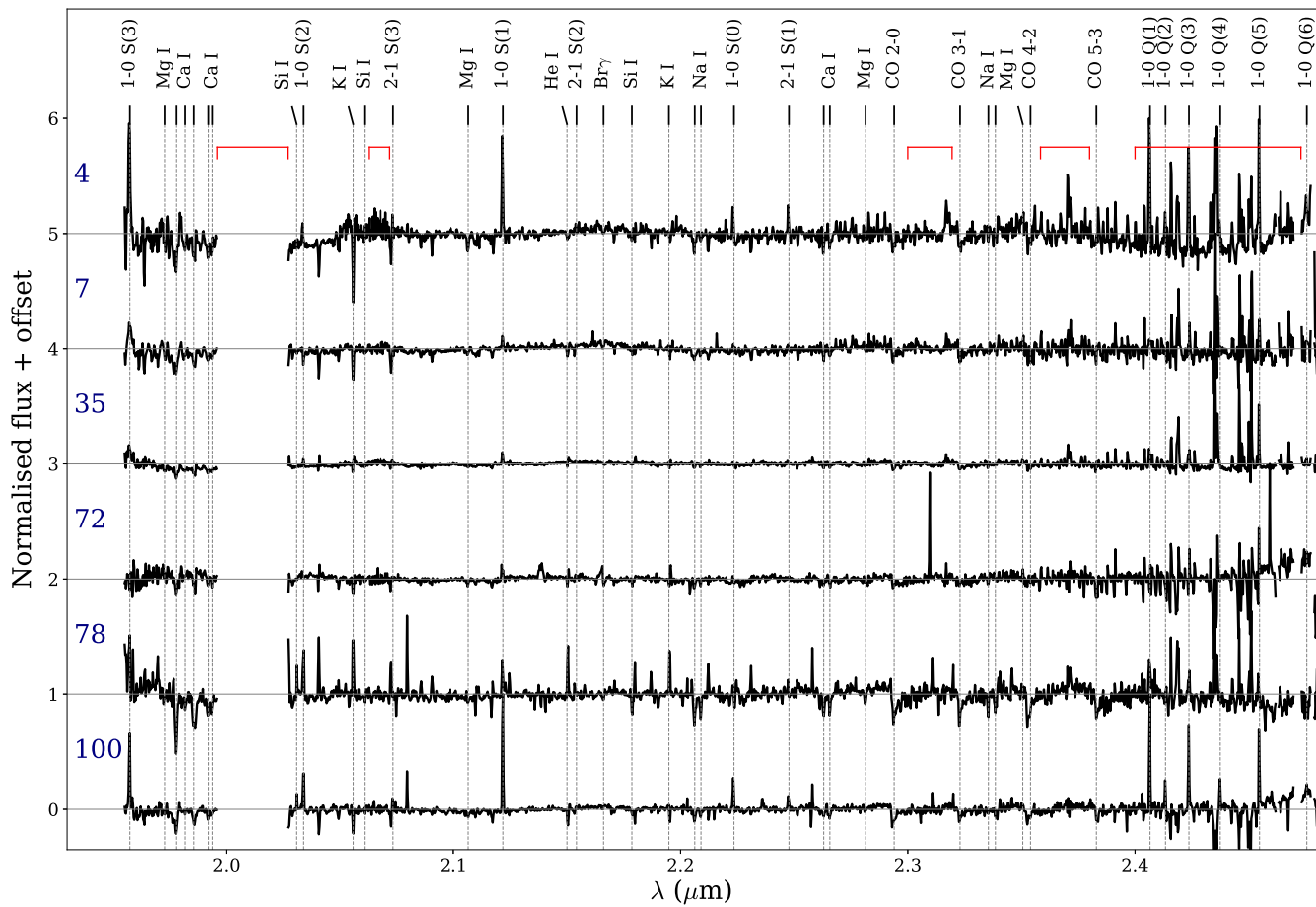


Figure B6. Spectra with H₂ emission lines and CO bandhead in absorption.

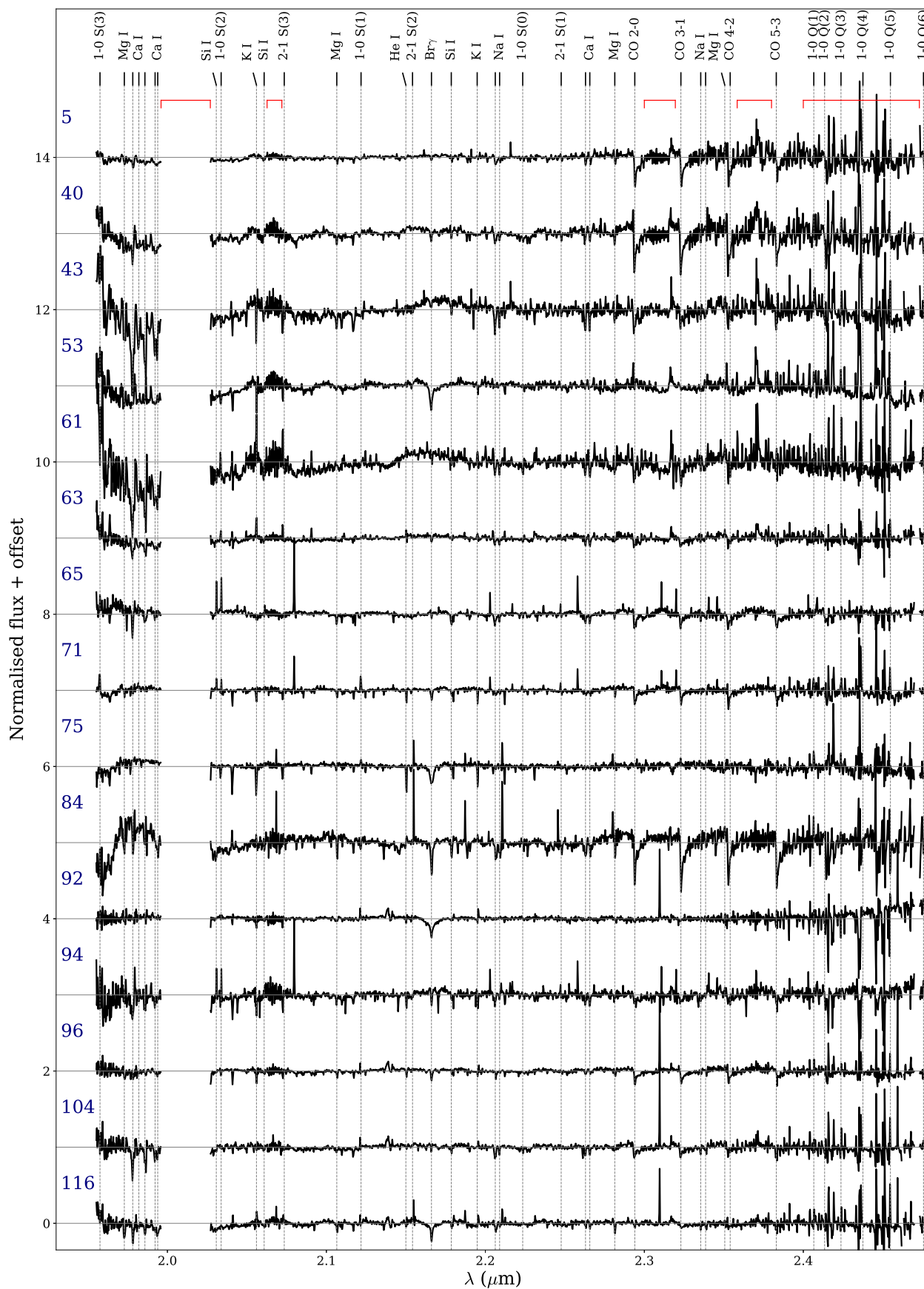


Figure B7. Spectra with Br γ absorption line.

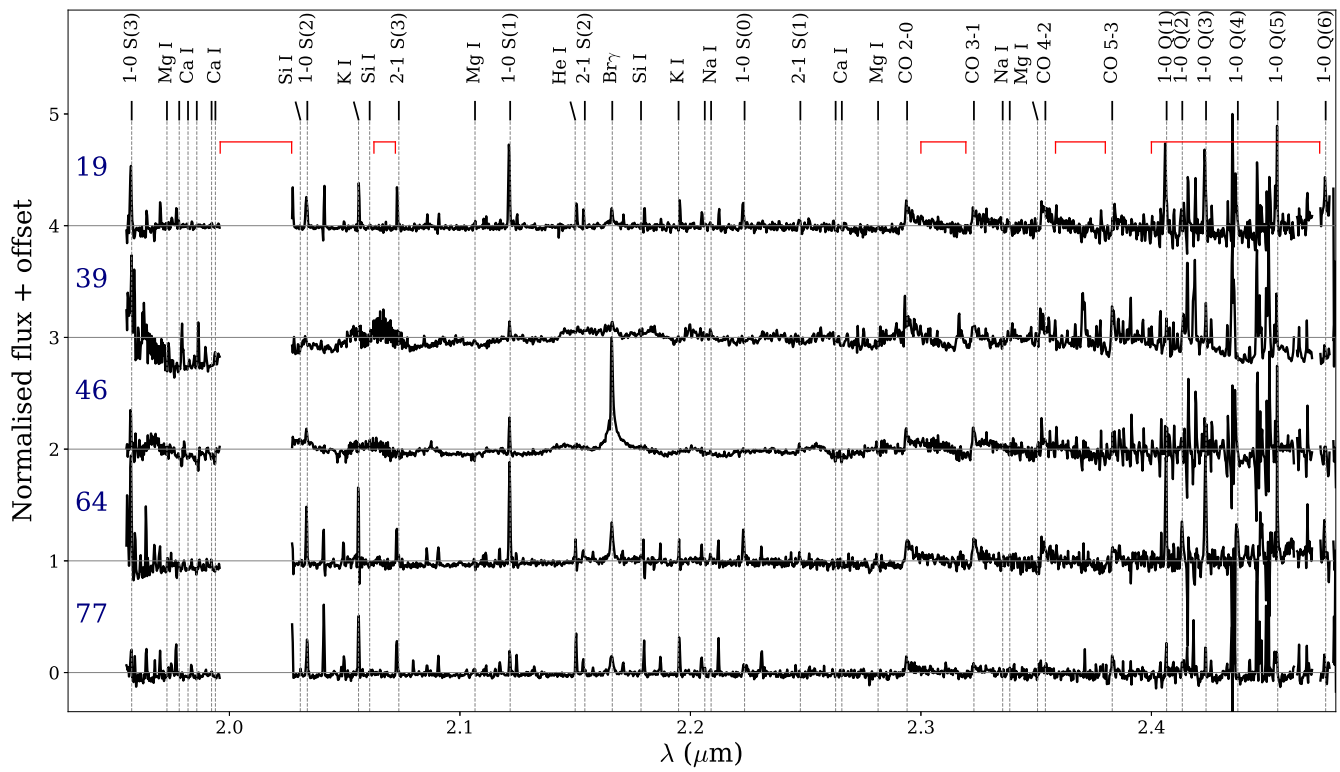


Figure B8. Spectra with CO bandhead in emission.

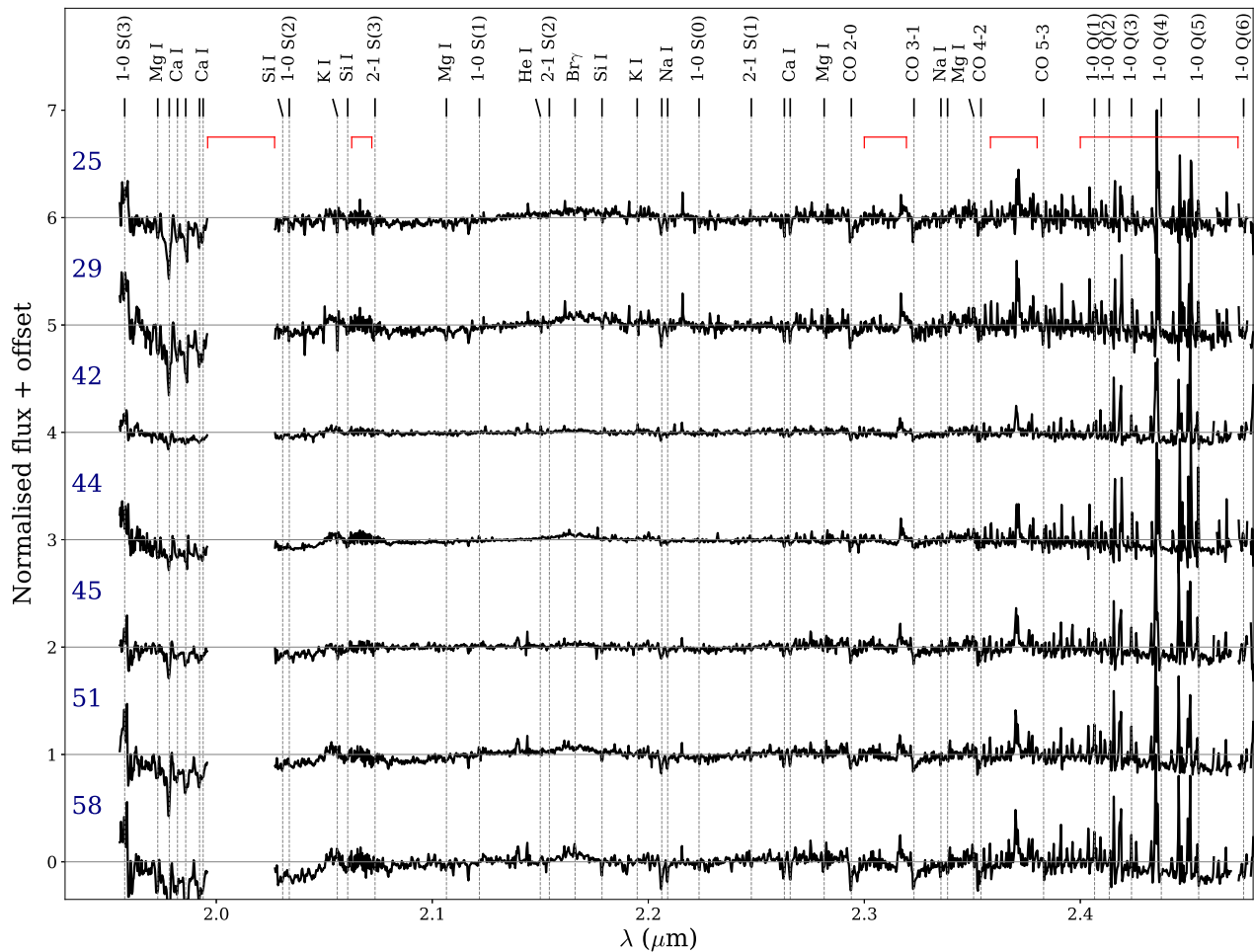


Figure B9. Spectra with CO bandhead in absorption.

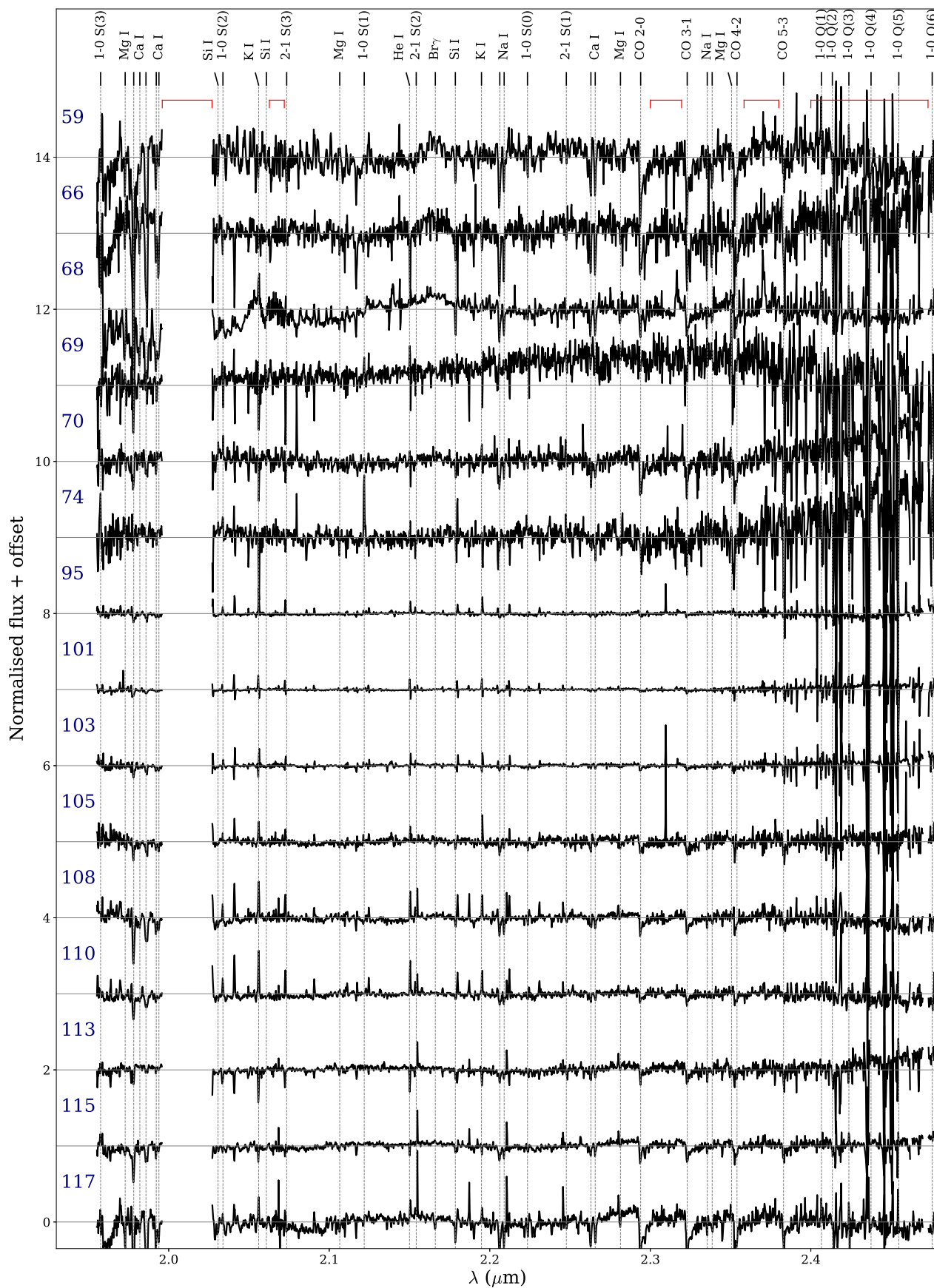


Figure B9. (Continued.)

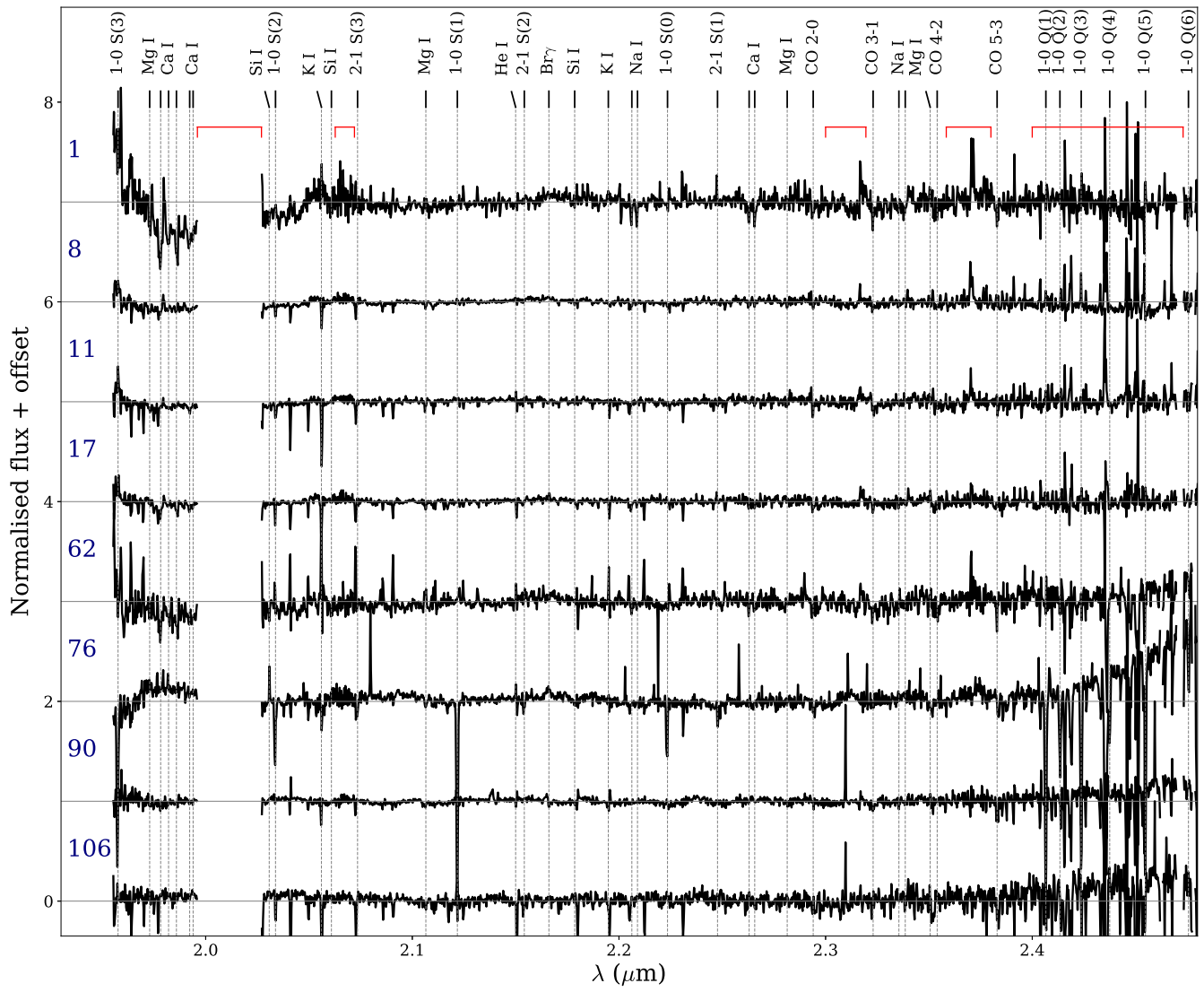


Figure B10. Spectra with no emission lines and no CO or Br γ absorption lines.

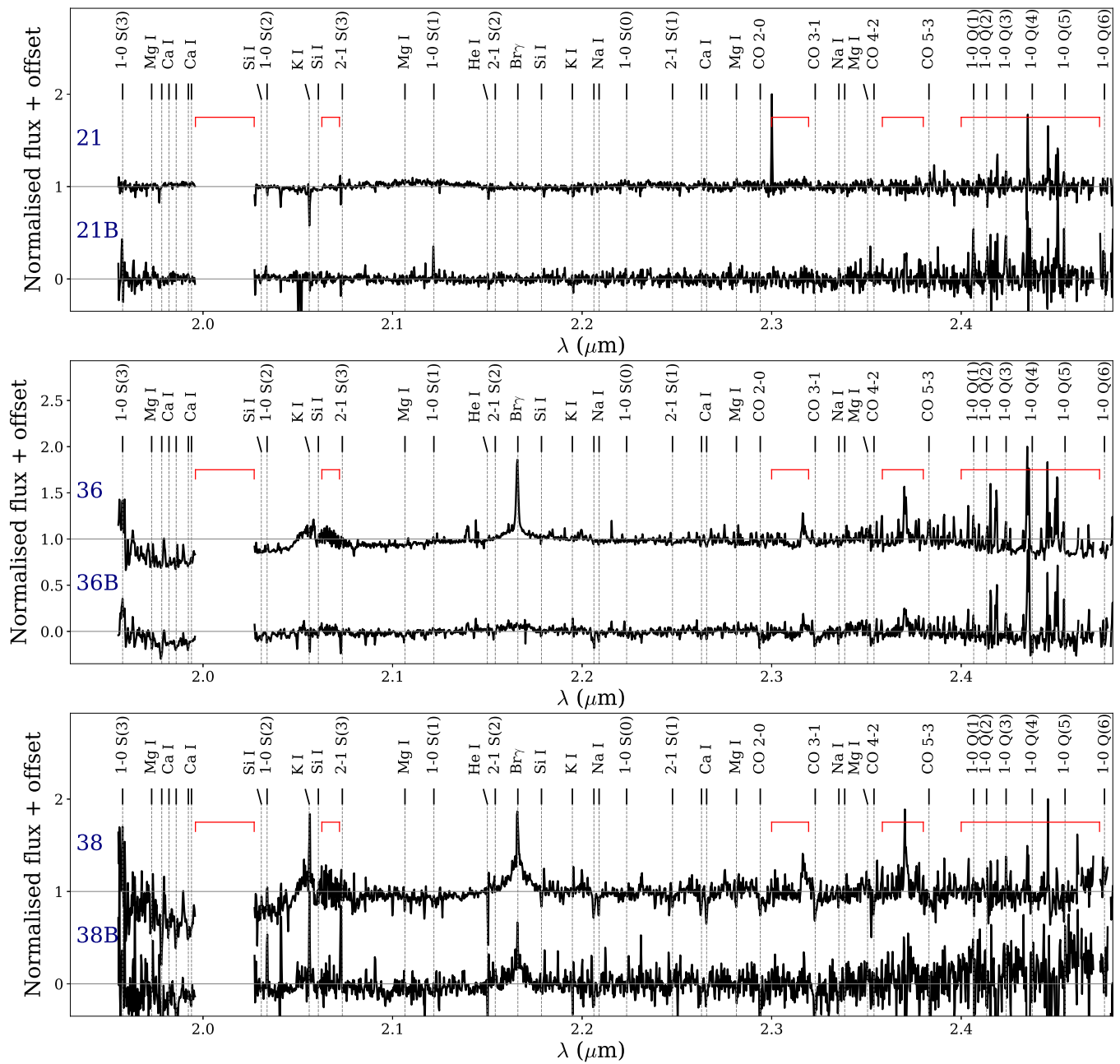


Figure B11. Spectra from three pairs of double sources.

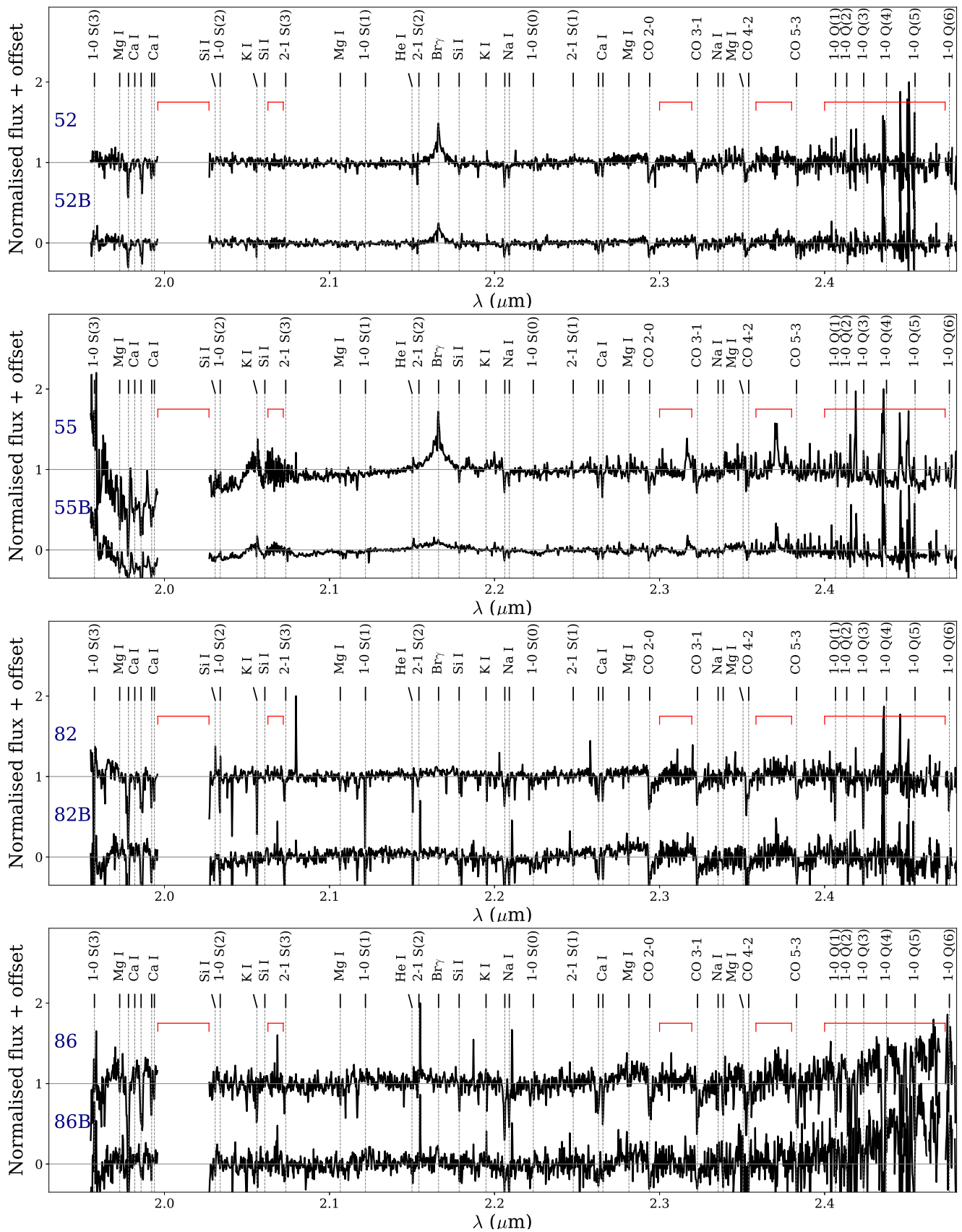


Figure B12. Spectra from double sources—continuation.

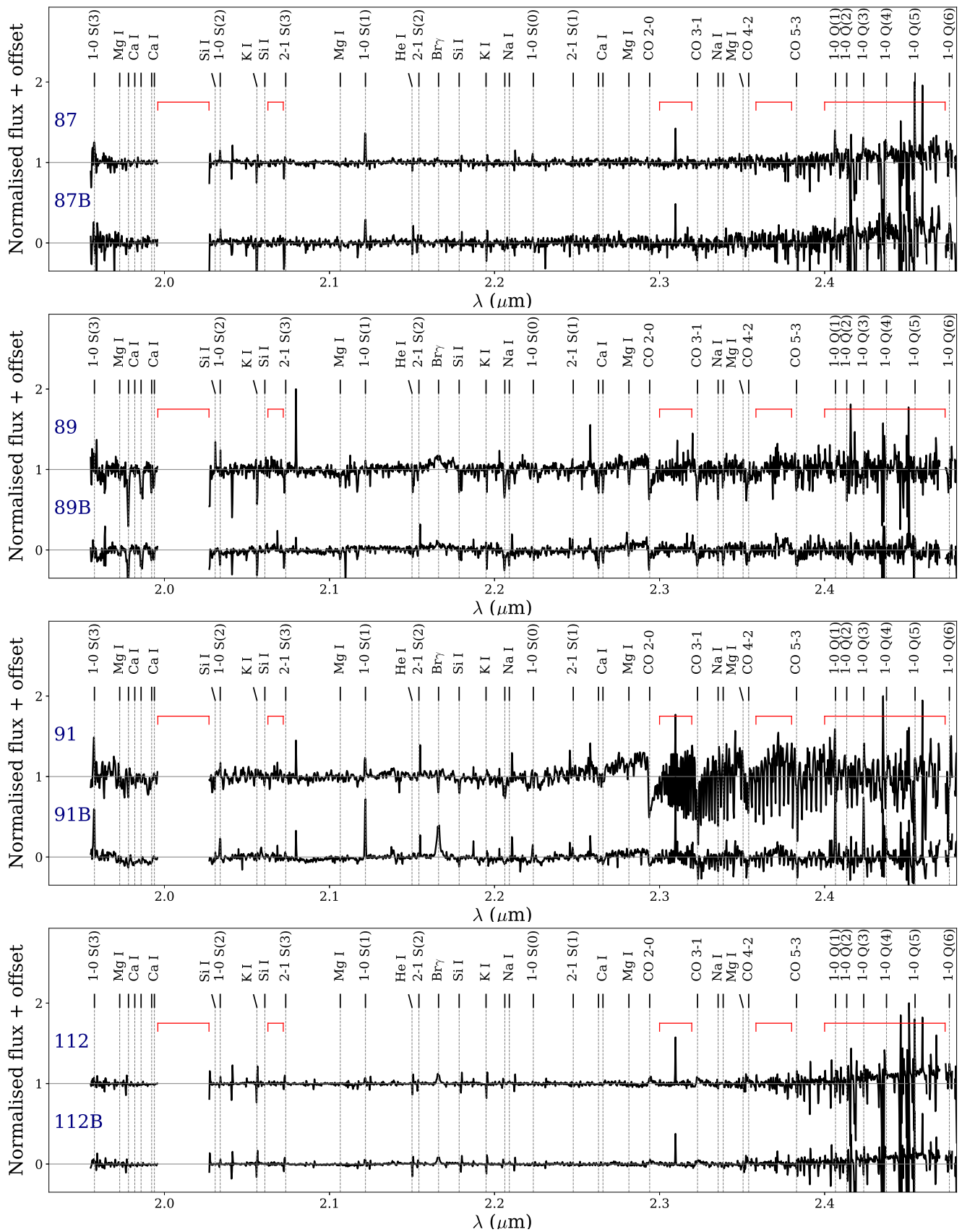


Figure B12. (Continued.)

Table 4
Detections

No.	H ₂	Br _γ	He I	Ca I	Mg I	Na I	Si I	K I	CO
2	E	N	N	A	A	A	N	N	N
47	E	N	N	N	N	N	N	N	N
87A	E	N	A	A	N	N	N	A	N
87B	E	N	A	A	A	A?	N	A	N
9	E	E	E	A	A	A	N	N	N
13	E	E	A	A?	N	N	N	A	N
15	E	E	A	A	A	A	N	A	N
26	E	E	?	A?	N	A	N	E	N
33	E	E	E	A	N	N	N	E	N
50	E	E	A	A	A	A	A?	A	N
54	E	E	N	A	?	N	N	A	N
60	E	E	E?	A	N	N	N	E?	N
83	E	E	A	A?	A?	N	?	A	N
111	E	E	E?	A	A	A	A?	E	N
112B	E?	E	A	?	N	N	N	A	N
114	E	E	E	?	N	A?	N	E	N
4	E	N	A?	A	A	A	N	A	A
7	E	N	A	A	A	A	A?	A	A
35	E	N	?	A	A	A	N	A	A
72	E	?	A?	A	A	A	A?	A	A
78	E	N	E	A	A	A	A	E	A
100	E	N	A	A	A	A	?	A	A
49	E	E	E	A	A	A	A?	E	A
73	E	E	E	A	A	A	E	E	A?
91B	E	E	N	A	A?	A	A	?	A
109	E	E	A	A	A	A	N	A	A
16	N	E	N	A	A	A	A?	N	N
24	N	E	N	A	A	A	N	A	N
28	N	E	N	A	A	A	A	A	N
31	N	E	?	A	N	N	N	A?	N
36A	N	E	N	A	A	A	A	N	N
41	N	E	N	A	A	N	N	A	N
56	N	E	A	A	A	A	N	A	N
79	N	E	A	A	N	A	N	A	N
81	N	E	A	A	A	A?	N	A?	N
85	N	E	A	A	A	A	N	A	N
93	N	E	E	A	N	A	E?	E	N
102	N	E	N	A	A	A	N	N	N
118	N	E	E	A	A	A	A?	E	N
3	N	E	N	A	A	A	A?	A	A
6	N	E	N	A	A	A	A?	A	A
10	N	E	E	A	A	A	N	E?	A?
12	N	E	E?	A	A	A	A?	N	A
18	N	E	E	A	A	A	A	E	A
20	N	E	A?	A	A	A	A	N	A
22	N	E	E	A	A	A	A?	E	A
23	N	E	E	A	A	A	A?	E?	A
30	N	E?	E?	A	A	A	A?	N	A
32	N	E	N	A	A	A	A	N	A
34	N	E	E	A	A	A	A	E?	A
38A	N	E	A	A	A	A	A?	E	A
38B	N	E	A	A	A	A?	A?	E	A
48	N	E	E?	A	A	A	A	N	A
52A	N	E	A	A	A	A	A	A	A
52B	N	E	A	A	A	A	A	A	A
55A	N	E	E?	A	A	A	A	E?	A
57	N	E	A?	A	A	A	N	A?	A
80	N	E	A	A	A	A	A	A	A
89A	N	E?	A	A	A	A	A?	A	A
97	N	E	A	A	A	A	A?	A?	A
98	N	E	A	A	A	A	A?	A	A
99	N	E	E	A	?	A	E?	E?	A

Table 4
(Continued)

No.	H ₂	Br _γ	He I	Ca I	Mg I	Na I	Si I	K I	CO
5	N	A	N	A	A	A	A	N	A
40	N	A	N	A	A	A	A	N	A
43	N	A	N	A	A	A	A	A?	A
53	N	A	N	A	A	N	N	A	N
61	N	A	E?	A	A	A	A	E	A
63	N	A	E?	A	A	A	A	E	A
65	N	A	N	A	A	A	A	N	A
71	N	A	A	A	A	A?	?	A	A
75	N	A	A	A?	A	N	A?	A	N
84	N	A	N	A	A	A	A	E?	A
91A	E	A	A?	A	A	A	A	E?	A
92	N	A	A	A	A	N	N	A	N
94	N	A	A	A	A	A	A?	A?	A
96	N	A	A	A	A	A	A?	A	A
104	N	A	A?	A	A	A	A	E?	A
116	N	A	A	A	A	A	A	E	A?
19	E	E	E	N	N	N	N	E	E
39	E?	E	N	A	A	A	N	N	E
46	E	E	N	A	A	N	N	N	E
64	E	E	E	A	A?	N	N	E	E
77	E	E	E	A?	A?	A?	E?	E	E
112A	E?	E	A	?	N	N	N	A	E
25	N	N	N	A	A	A	A	A	A
29	N	N	A?	A	A	A	A	A	A
42	N	N	E?	A	A	A	N	E?	A
44	N	N	N	A	A	A	A?	A?	A
45	N	N	N	A	A	A	N	N	A
51	N	N	N	A	A	A	A	N	A
55B	N	N	E	A	A	A	A?	E?	A
58	N	N	E?	A	A	A	A?	N	A
59	N	N	?	A	A	A	A?	N	A
66	N	N	A	A	A	A	A	N	A
68	N	N	N	A	A	A	A	E?	A
69	N	N	E?	A	A?	A?	N	A	A?
70	N	N	A	A	A	A	A?	A	A
74	N	N	E?	A	A	A	?	A	A
82A	N	N	A	A	A	A	A?	A	A
82B	N	N	A	A	A	A	A?	A	A
86A	N	N	N	A	A	A	A?	A	A
86B	N	N	?	A	A?	A	A?	A?	A
89B	N	N	?	A	A	A	A?	A	A
95	N	N	E	A	A	A	N	E	A?
101	N	N	E?	A	N	A	E?	E	A
103	N	N	A?	A	A	A	A?	E	A
105	N	N	E	A	A	A	A	E	A
108	N	N	E	A	A	A	A	E	A
110	N	N	E	A	A	A	A?	E	A
113	N	N	A	A	A	A	A	A	A
115	N	N	A	A	A	A	A	A	A
117	N	N	E	A	A	A	A	E	A
1	N	N	?	A	A	A	A	E?	N
8	N	N	N	A	A?	A?	N	A	N
11	N	N	E	A	A	N	N	A	N
14	N	N	E	A?	A	N	E?	E	N
17	N	N	A	A	A	A	N	A	N
21A	N	N	A?	?	N	N	N	A	N
21B	N	N	A?	?	A	N	N	A	N
62	N	N	E	A	A	A	N	E	N
76	N	N	?	N	A?	N	?	A?	N
90	N	N	A	A?	A?	N	N	A	N
106	N	N	A	A	N	A?	N	A	N

Note. E indicates emission line, A—absorption, N—no detection, and ?—possible detection.

Table 5
H₂ Emission-line Fluxes

No.	1-0 S(0)	1-0 S(1)	1-0 S(2)	1-0 S(3)	2-1 S(1)	2-1 S(2)	2-1 S(3)	No.	1-0 Q(1)	1-0 Q(2)	1-0 Q(3)	1-0 Q(4)	1-0 Q(5)	1-0 Q(6)
				(10 ⁻¹⁶ erg s ⁻¹ cm ⁻²)							(10 ⁻¹⁶ erg s ⁻¹ cm ⁻²)			
2	5.35 ± 0.33	25.61 ± 0.58	10.18 ± 0.38	36.90 ± 3.39	2.24 ± 0.87	2	25.77 ± 1.54	5.97 ± 1.86	22.60 ± 1.10	...	16.72 ± 1.14	5.40 ± 1.37
4*	1.55 ± 0.16	3.36 ± 0.20	0.85 ± 0.11	6.27 ± 1.19	0.97 ± 0.26	4*	5.38 ± 0.84	...	4.99 ± 0.65	...	2.98 ± 0.56	...
7*	...	0.87 ± 0.15	7*	2.57 ± 0.76	...
9	...	1.62 ± 0.12	...	1.83 ± 0.51	9
13	...	2.33 ± 0.56	...	3.26 ± 0.93	13
15	...	4.42 ± 0.27	...	7.84 ± 2.26	1.91 ± 0.31	15	5.70 ± 1.22	...	6.59 ± 1.45	...	4.21 ± 0.92	...
19	1.52 ± 0.25	5.30 ± 0.22	2.62 ± 0.24	5.14 ± 0.84	1.21 ± 0.31	19	6.21 ± 0.83	...	6.71 ± 0.90	...	3.62 ± 1.02	2.24 ± 0.67
26	...	1.51 ± 0.20	0.86 ± 0.20	26
33	0.94 ± 0.30	2.17 ± 0.16	0.83 ± 0.15	5.43 ± 1.39	33	3.53 ± 0.75	...	3.30 ± 1.00
35	...	3.24 ± 0.31	35
39	...	12.53 ± 1.57	39	22.78 ± 2.78
46	...	12.92 ± 0.60	6.16 ± 0.81	46
47	17.48 ± 0.52	69.91 ± 1.05	22.15 ± 0.51	76.05 ± 2.38	7.43 ± 0.40	3.09 ± 0.36	6.19 ± 0.34	47	85.63 ± 2.80	24.76 ± 0.95	76.93 ± 2.74	20.75 ± 3.33	26.15 ± 1.24	10.96 ± 2.36
49	...	4.65 ± 0.34	3.14 ± 0.47	3.30 ± 0.59	49	6.04 ± 0.53	...	4.87 ± 0.53
50	...	1.47 ± 0.18	0.49 ± 0.17	4.37 ± 1.22	50	2.09 ± 0.56	...	4.97 ± 1.02	...
54*	23.05 ± 6.16	75.32 ± 14.15	...	123.66 ± 27.71	54*
60	14.58 ± 0.69	60.13 ± 0.47	23.57 ± 0.71	99.90 ± 13.36	7.30 ± 0.79	2.74 ± 0.36	5.84 ± 1.29	60	65.22 ± 3.30	12.80 ± 1.80	58.16 ± 2.53	39.66 ± 9.77	24.78 ± 5.70	13.01 ± 4.73
64	3.11 ± 0.42	9.67 ± 0.45	4.86 ± 0.23	0.79 ± 0.25	2.45 ± 0.77	64	10.93 ± 1.08	4.87 ± 1.14	11.93 ± 0.62	3.51 ± 1.05
73	...	1.64 ± 0.32	2.45 ± 0.26	0.69 ± 0.13	...	73	2.78 ± 0.58	...	2.49 ± 0.33	...	2.37 ± 0.53	...
77	...	1.37 ± 0.14	2.43 ± 0.26	...	0.40 ± 0.14	77	1.64 ± 0.46
83	...	2.88 ± 0.26	...	3.25 ± 1.01	83
87A	0.49 ± 0.17	2.11 ± 0.19	87A	1.52 ± 0.52	...	1.17 ± 0.33
87B	...	0.66 ± 0.08	87B	0.40 ± 0.17
91A*	...	11.73 ± 1.70	...	17.49 ± 4.68	...	5.43 ± 1.05	...	91A*	20.27 ± 6.68	...	17.11 ± 4.79
91B*	1.21 ± 0.32	4.84 ± 0.26	1.93 ± 0.32	4.14 ± 0.56	0.79 ± 0.23	91B*	5.87 ± 0.50	...	4.77 ± 0.25
100*	2.56 ± 0.28	10.07 ± 0.25	3.77 ± 0.54	6.33 ± 0.92	1.40 ± 0.25	100*	8.61 ± 0.48	2.63 ± 0.67	6.22 ± 0.38
109	2.12 ± 0.18	9.18 ± 0.46	2.61 ± 0.27	7.89 ± 1.44	0.80 ± 0.14	109	9.26 ± 0.42	2.91 ± 0.56	6.85 ± 0.66
111	...	3.93 ± 0.90	2.14 ± 0.49	111
112A	0.27 ± 0.03	0.79 ± 0.16	112A	1.73 ± 0.34
112B	...	0.58 ± 0.15	0.25 ± 0.09	112B
114	2.64 ± 0.31	10.46 ± 0.65	4.93 ± 0.19	6.72 ± 1.08	0.83 ± 0.25	1.69 ± 0.40	2.97 ± 0.69	114	12.57 ± 1.00	...	9.87 ± 0.79

Notes. H₂ line fluxes have not been corrected for extinction. Only fluxes with detection significance above 3σ are reported. Targets with asterisks do not have estimated extinctions from SED models.

Appendix C Line Emission Maps

Figures C1–C5 show the emission maps of the most commonly detected H₂ lines in the *K*-band range: 1-0 S(1) at 2.1218 μ m (Figure C1), 1-0 S(0) at 2.2235 μ m (Figure C2),

1-0 Q(1) line at 2.4066 μ m (Figure C3), 1-0 Q(3) line at 2.4237 μ m (Figure C4), and 2-1 S(1) line at 2.2477 μ m (Figure C5). Figure C6 shows the spatial extent of several transitions of H₂ toward source No. 47, which has the most molecular-rich spectrum at *K*-band. Source No. 47 has a *K*-band magnitude of 15.2 based on our KMOS observations, and thus it is one of the

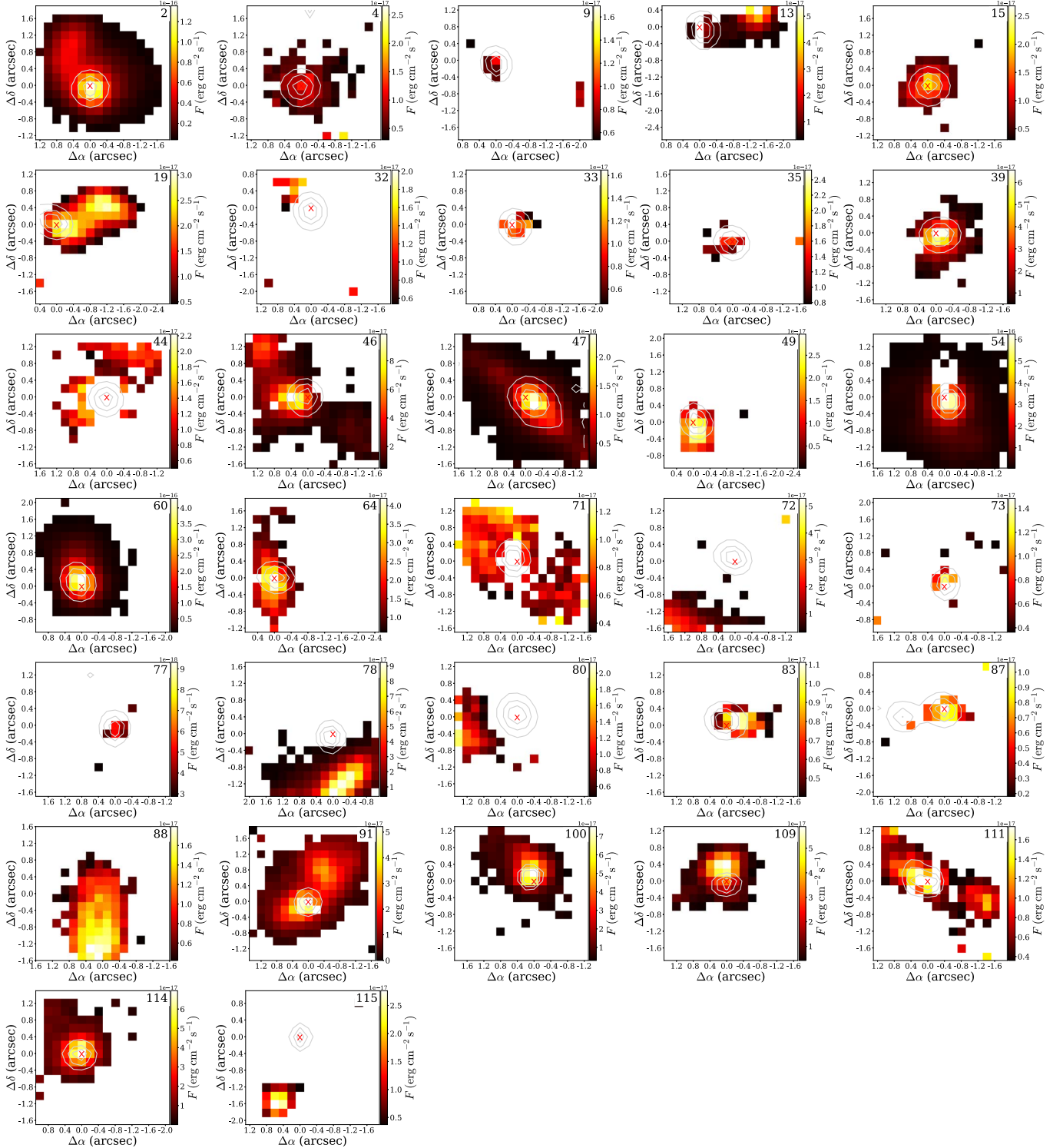


Figure C1. Integrated maps of the H₂ 1-0 S(1) line at 2.1218 μ m for a subsample of sources where the extended H₂ emission is detected (see Table 2). Colors correspond to the line fluxes at each pixel (detections above 3σ), and white contours correspond to the continuum emission in *K* band (see also Appendix A). Source names are provided in the upper right corners (No. in Table 2). We note that source No. 88 (G224.4514–00.7054) has a nondetection of the continuum emission at 2.1218 μ m.

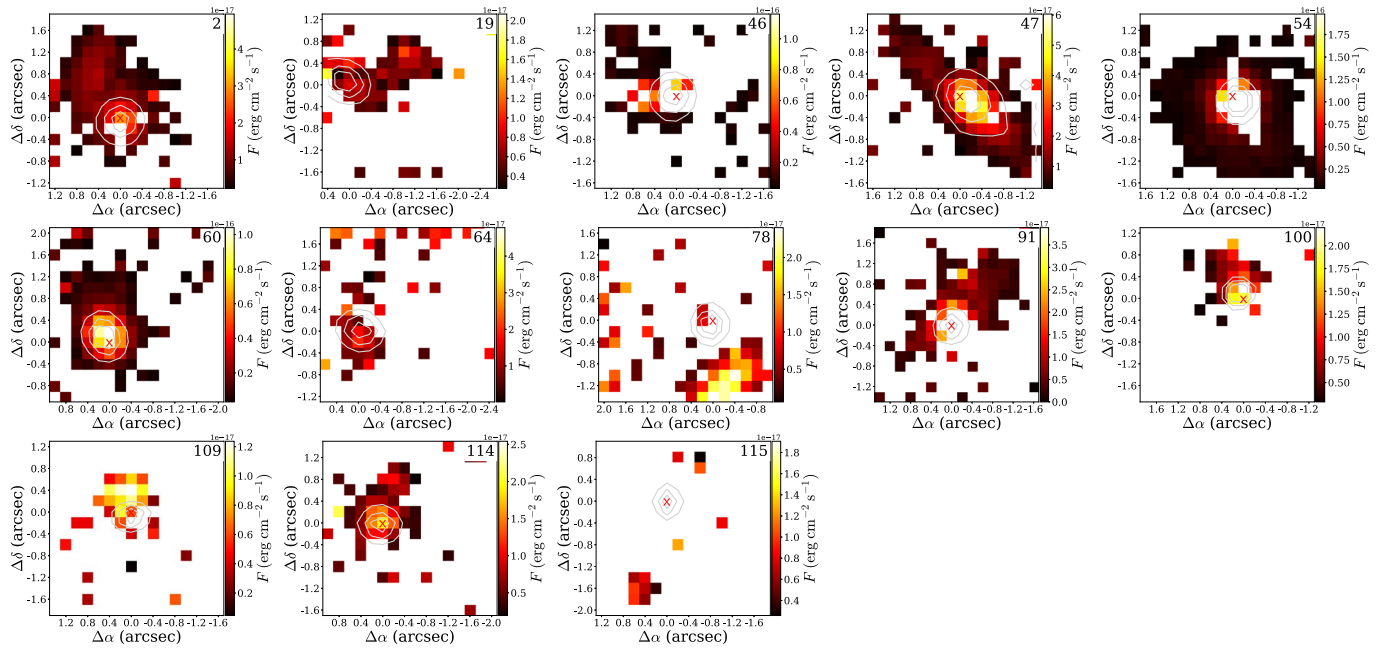


Figure C2. Similar to Figure C1, but for the H₂ 1-0 S(0) line at 2.2235 μm. Only emission above 2σ is shown.

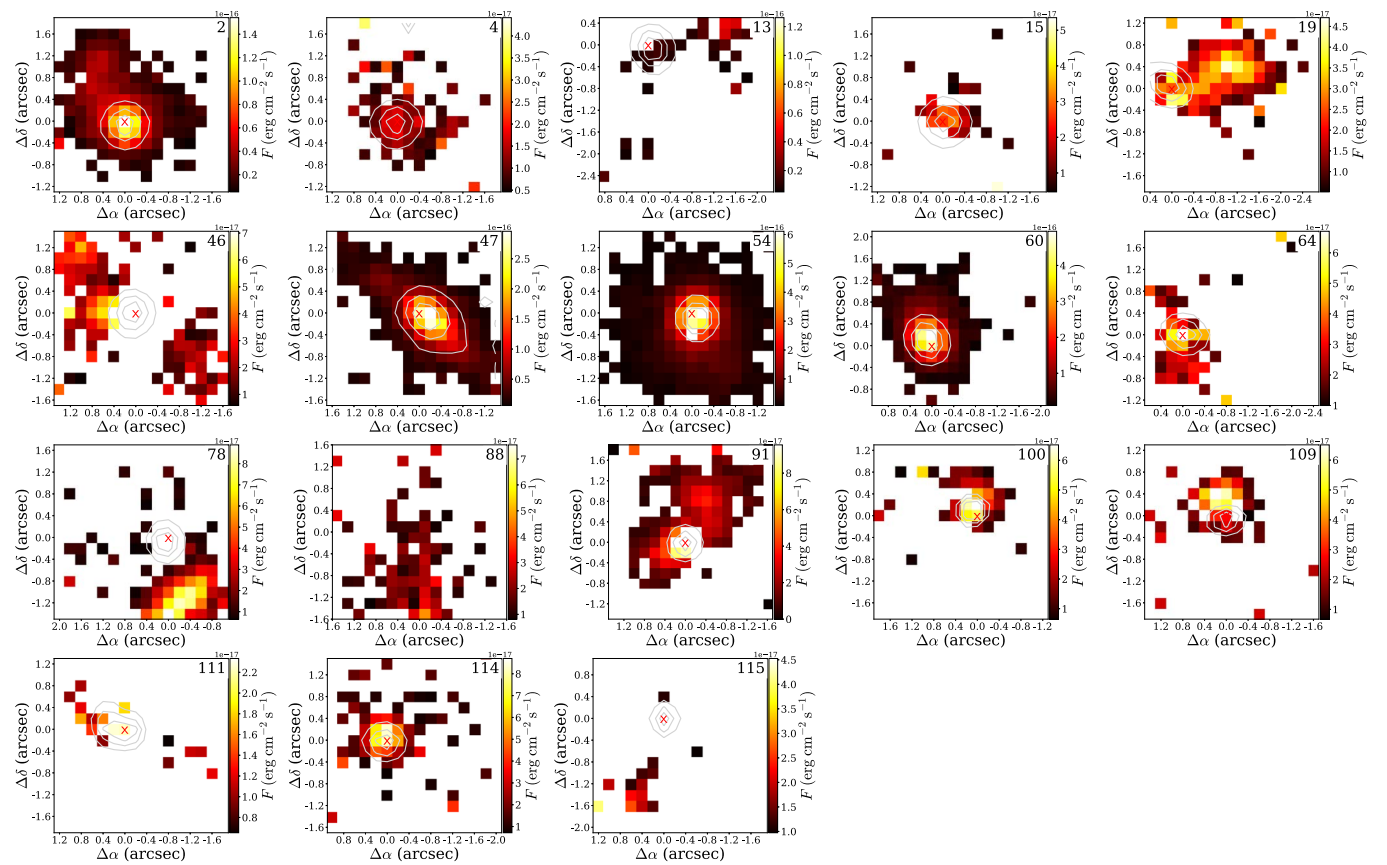


Figure C3. Similar to Figure C1, but for the H₂ 1-0 Q(1) line at 2.4066 μm. Only emission above 2σ is shown.

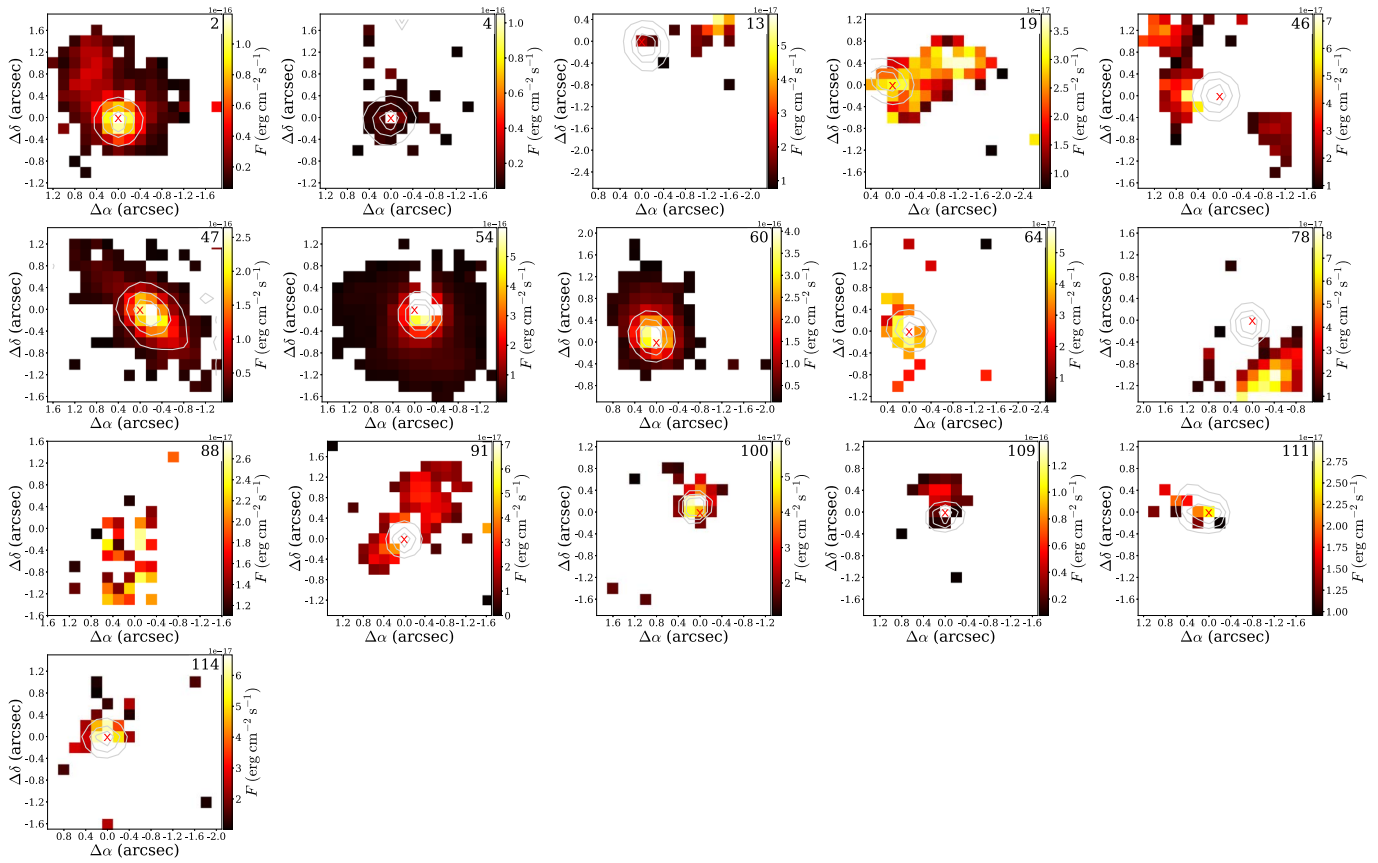


Figure C4. Similar to Figure C1, but for the H₂ 1-0 Q(3) line at 2.4237 μm . Only emission above 2σ is shown.

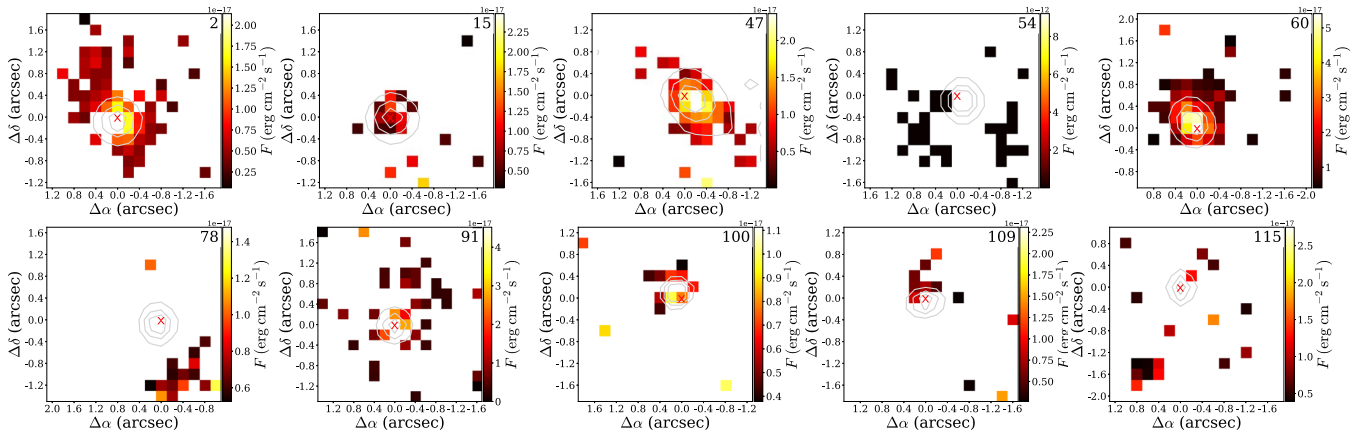


Figure C5. Similar to Figure C1, but for the H₂ 2-1 S(1) line at 2.2477 μm . Only emission above 2σ is shown.

faintest sources in the sample. Sewilo et al. (2019) classified it as a Class I YSO. The young evolutionary stage of the source is confirmed by strong bipolar outflows. This source is an interesting case for detailed follow-up studies.

Figure C7 shows the hydrogen Br γ 2.17 μm emission maps. Figures C8, C9, C10, and C11 show the emission maps for several CO bandhead transitions—CO 2-0, 3-1, 4-2, and CO 5-3, respectively.

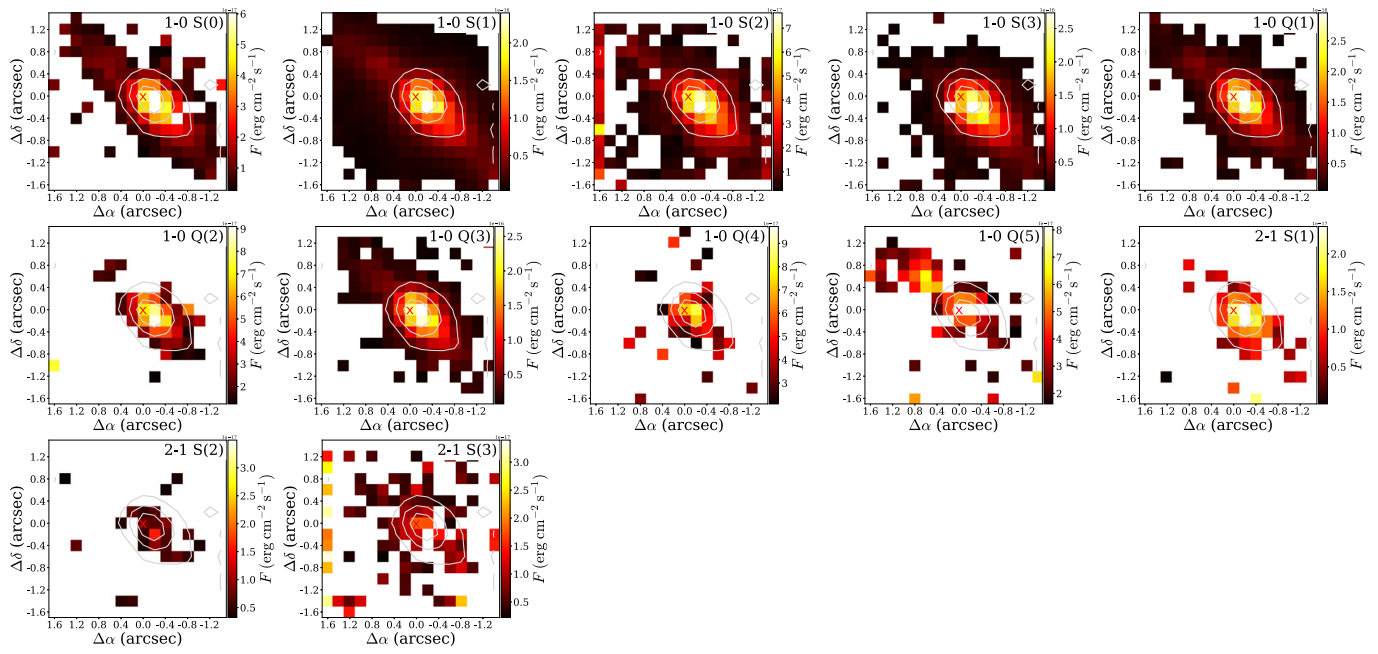


Figure C6. Maps in several H₂ lines in source No. 47, which shows detections of the most highly excited H₂ lines in the entire sample (see Table 2).

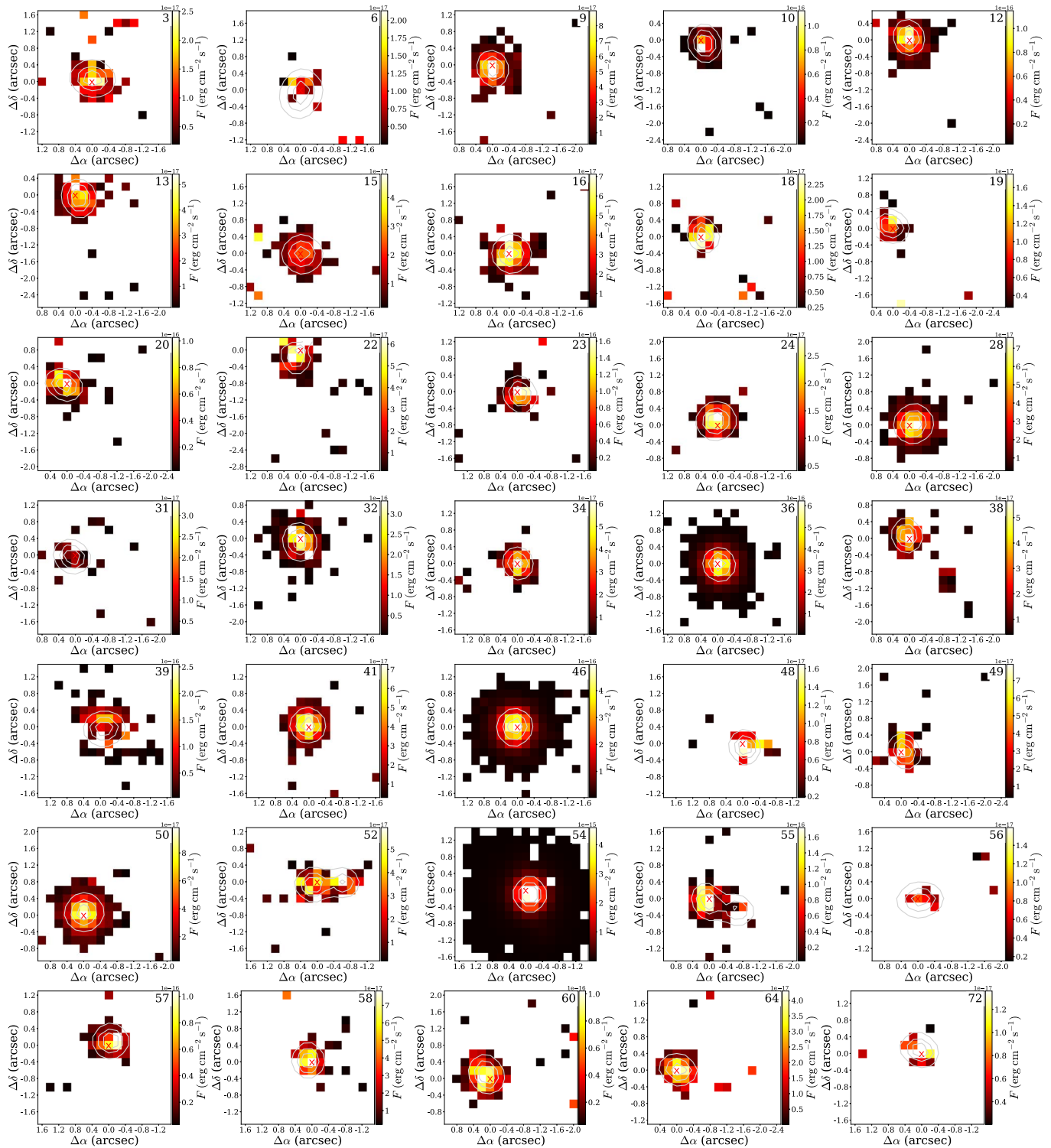


Figure C7. Integrated maps for the H Br γ line at $2.1661 \mu\text{m}$. Colors correspond to the line fluxes at each pixel (detections above 2σ), and white contours show the continuum emission in K band (see also Appendix A).

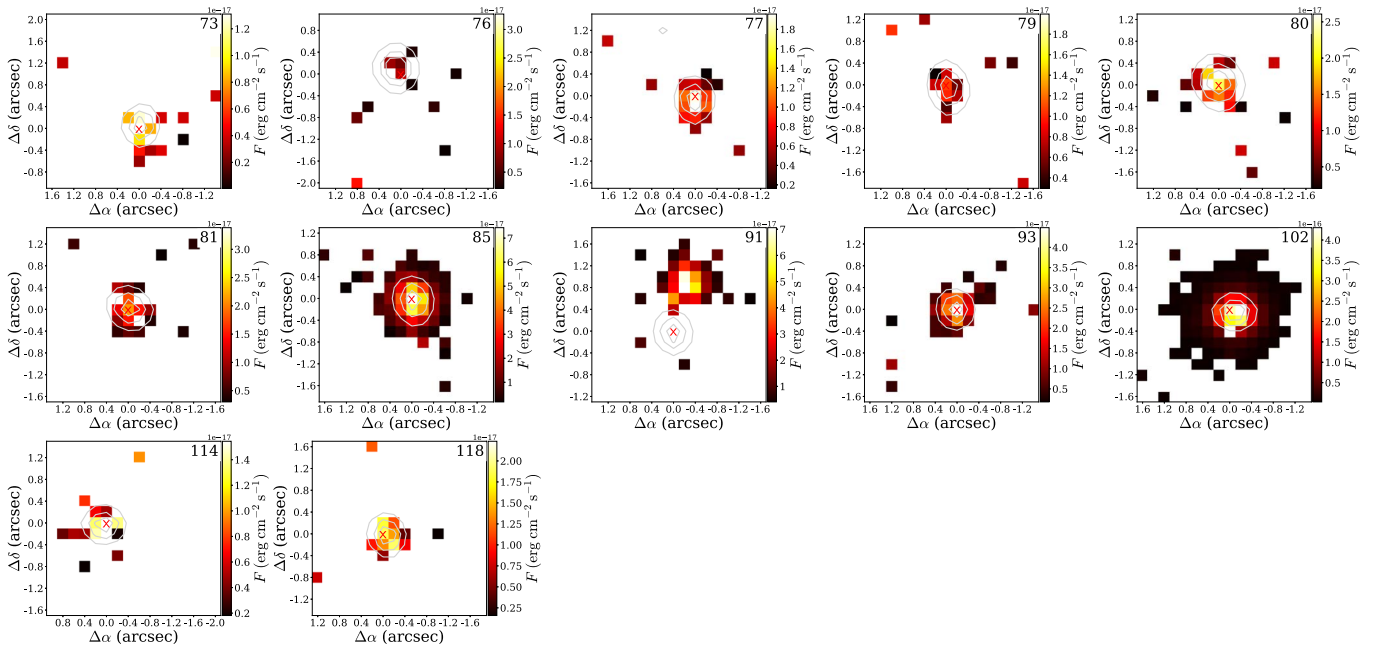


Figure C7. (Continued.)

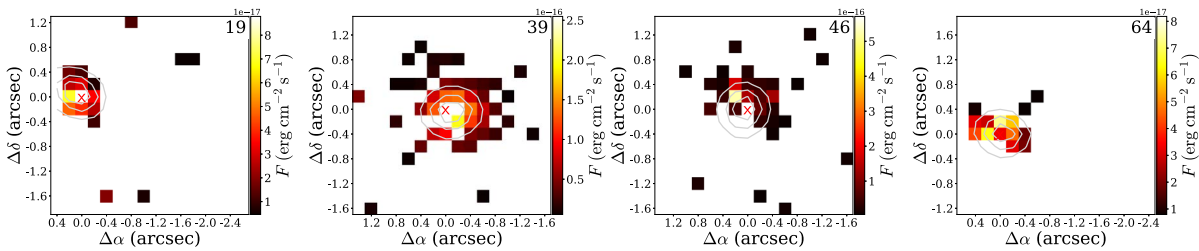


Figure C8. Integrated maps of the CO $\nu = 2-0$ line at $2.29 \mu\text{m}$. Colors correspond to the line fluxes at each pixel (detections above 2σ), and white contours show the continuum emission in K band (see also Appendix A).

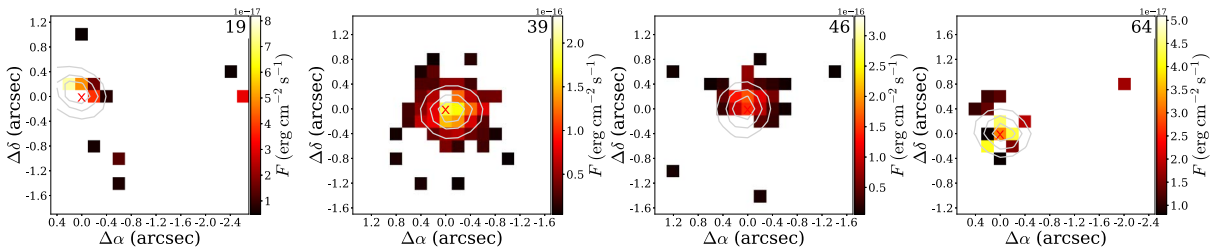


Figure C9. Similar to Figure C8, but the maps show the CO $\nu = 3-1$ line at $2.32 \mu\text{m}$.

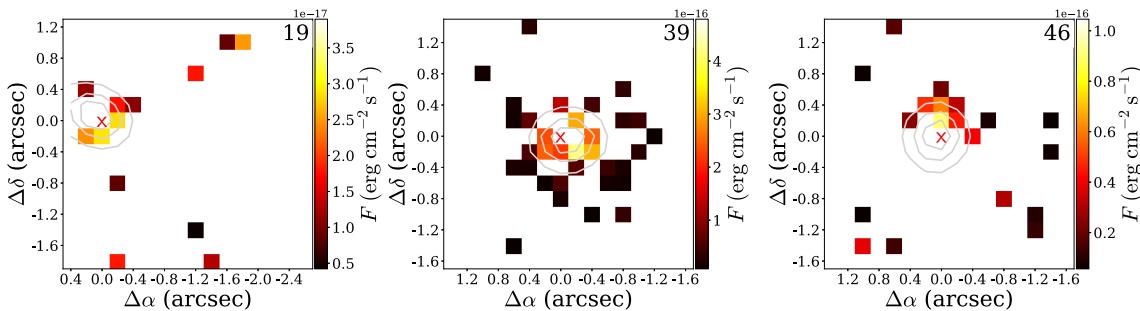


Figure C10. Similar to Figure C8, but the maps show the CO $\nu = 4-2$ line at $2.35 \mu\text{m}$.

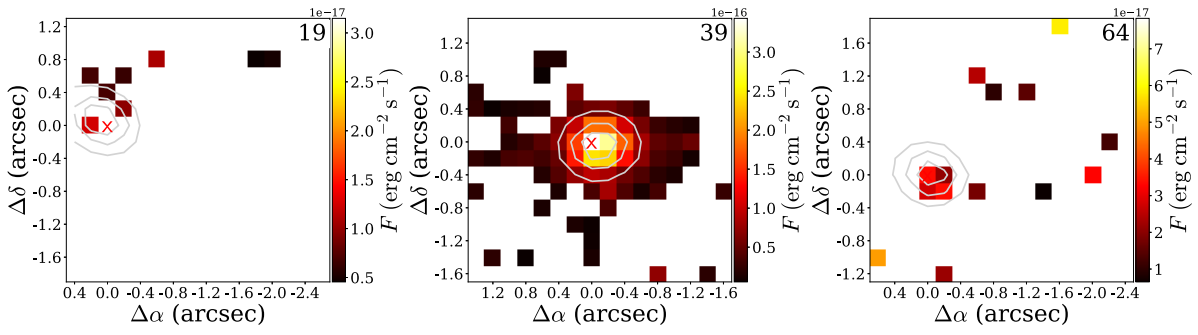


Figure C11. Similar to Figure C8, but the maps show the CO $\nu = 5-3$ line at $2.38 \mu\text{m}$.

Appendix D Extinction within Stellar Envelopes

The extinction values from SED modeling incorporate only the interstellar extinction to the source. Some of our stars were identified to be embedded in the envelope. Thus, to complete the estimations of extinction, we investigate the level of extinction due to the envelope. We consider only the targets for which best-fit SED models included the envelope component (Sewiło et al. 2019). For simplicity, we assume that the spherical envelope can be described well by the power-law density profile (Robitaille 2017, Equation (3)):

$$\rho(r) = \rho_0 \cdot (r/R_0)^\gamma, \quad (\text{D1})$$

where ρ_0 is the volume mass density at the radius R_0 and γ represents the slope of the relation. We do not include outflow cavities, which were considered in the original models.

To calculate column densities, we integrate the density profile along the line of sight, between the inner and outer radii of the envelope. We assume a mean molecular weight of 2.8 and a gas-to-dust ratio of 100. For calculations, we adopt parameter values from SED modeling of Sewiło et al. (2019) and set the outer radius to be at 5000 au (the maximum value considered in models of Robitaille 2017). In cases where the inner radius was not available, we assume a value of 50 au. For target No. 47, we also assume the $R_0 = 100$ au, which is within the parameter range adopted in the SED modeling (Robitaille 2017). Some of our sources were originally fitted by a broken power-law density profile (Robitaille 2017, Equation (4)) and therefore they lack the value of γ . We assume a slope of $-1/2$ for $r < R_0$ and $-3/2$ for $r > R_0$, following the description in Section 3.2.3 of Robitaille (2017).

We estimate the visual extinction due to the envelope of YSOs based on derived column densities. We follow the formula from Predehl & Schmitt (1995):

$$A_V = 1.086 \cdot N \cdot \pi a_g^2 \cdot Q_{\text{ext}}, \quad (\text{D2})$$

where N is the column density in 10^{21} cm^{-2} , a_g is the radius of a spherical grain in $0.1 \mu\text{m}$, and Q_{ext} is the extinction

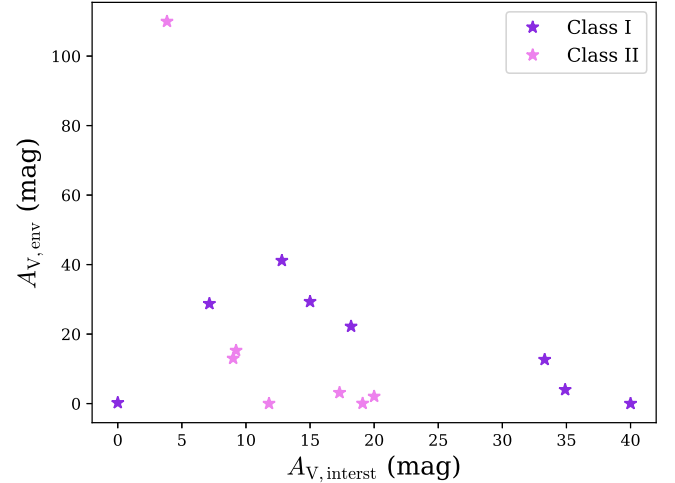


Figure D1. Comparison between the total visual extinction $A_{V,\text{total}}$ (Sewiło et al. 2019) and the extinction within the envelope $A_{V,\text{env}}$. The latter was estimated assuming spherical envelope and a power-law density profile. See the text for details.

efficiency. We adopted $a_g = 0.1 \mu\text{m}$ and $Q_{\text{ext}} = 0.5$. The resulting estimates are shown in Figure D1 as a function of a total A_V obtained from the SED models. $A_{V,\text{env}}$ is higher for most Class I than for Class II sources, indicating that envelope is being dissipated with time, in line with evolutionary predictions. The only outlier, Class II star No. 65, is characterized by high $\rho_0 = 1.8 \times 10^{-18} \text{ g cm}^{-3}$, which leads to the very high value of the envelope extinction. This source is very bright, has relatively low A_V , and has no emission lines, which are signposts of ongoing accretion or ejection. Clear detection of the CO bandhead in absorption suggests that this target might be a foreground contamination, possibly a red giant. Table 6 shows the values of interstellar and envelope extinction for all sources with SED models.

Table 6
Interstellar and Envelope Extinction Values from SED Modeling








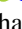
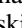

No.	$A_{V,interst}$	$A_{V,env}$
1	8.04	...
2	9.0	12.99
3	11.9	...
5	34.9	3.98
6	23.4	...
8	25.3	...
9	30.8	...
10	27.6	...
12	31.0	...
13	15.4	...
15	40.0	...
16	21.3	...
19	33.9	...
20	12.2	...
24	27.0	...
26	25.9	...
28	9.92	...
30	2.84	...
32	6.84	...
33	21.7	...
35	20.0	2.06
39	10.2	...
40	28.6	...
42	26.2	...
43	2.29	...
45	19.3	...
46	14.0	...
47	33.3	12.65
48	3.03	...
49	32.0	...
50	15.7	...
53	22.4	...
55A	3.37	...
55B	3.37	...
56	22.0	...
58	5.03	...
59	2.9	...
60	18.2	22.21
61	8.51	...
62	17.3	...
63	22.6	...
64	7.15	28.74
65	3.84	109.96
68	7.19	...
70	10.6	...
71	27.8	...
73	26.2	...
75	23.1	...
76	24.2	...
77	40.0	0.00
79	15.1	...
81	25.7	...
82A	11.8	0.01
82B	11.8	0.01
83	12.8	41.15
84	17.3	3.13
86A	6.14	...
86B	6.14	...
87A	30.3	...
87B	30.3	...
88	0.0	0.23
92	9.37	...
93	28.5	...
94	8.96	...

Table 6
(Continued)

No.	$A_{V,interst}$	$A_{V,env}$
95	4.49	...
96	19.1	0.04
97	13.9	...
98	7.47	...
102	15.4	...
104	7.78	...
105	28.1	...
108	7.74	...
109	15.0	29.33
110	16.9	...
111	17.0	...
112A	25.1	...
112B	25.1	...
113	21.7	...
114	39.4	...
115	9.23	15.27
116	2.43	...
117	5.11	...
118	12.7	...

Notes. All values are given in magnitudes. $A_{V,interst}$ is the value adopted from Sewilo et al. (2019) based on the SED modeling; we assume an uncertainty of 10 mag of their measurements (see text for details). The $A_{V,env}$ is the extinction within the envelope estimated based on the results of the SED modeling.

ORCID iDs

Dominika Itrich  <https://orcid.org/0000-0002-9051-1781>
 Agata Karska  <https://orcid.org/0000-0001-8913-925X>
 Marta Sewilo  <https://orcid.org/0000-0003-2248-6032>
 Lars E. Kristensen  <https://orcid.org/0000-0003-1159-3721>
 Gregory J. Fischer  <https://orcid.org/0000-0002-7154-6065>
 William J. Fischer  <https://orcid.org/0000-0002-3747-2496>
 Benoît Tabone  <https://orcid.org/0000-0002-1103-3225>
 Will R. M. Rocha  <https://orcid.org/0000-0001-6144-4113>
 Maciej Koprowski  <https://orcid.org/0000-0001-5785-1154>
 Ngân Lê  <https://orcid.org/0000-0003-1990-1717>

References

- Agra-Amboage, V., Cabrit, S., Dougados, C., et al. 2014, *A&A*, **564**, A11
 Alcalá, J. M., Manara, C. F., Natta, A., et al. 2017, *A&A*, **600**, A20
 Alcalá, J. M., Natta, A., Manara, C. F., et al. 2014, *A&A*, **561**, A2
 André, P. 2017, *CRGeo*, **349**, 187
 Ansdell, M., Williams, J. P., Manara, C. F., et al. 2017, *AJ*, **153**, 240
 Astropy Collaboration, Robitaille, T. P., Tollerud, E. J., et al. 2013, *A&A*, **558**, A33
 Bally, J. 2016, *ARA&A*, **54**, 491
 Balser, D. S., Rood, R. T., Bania, T. M., & Anderson, L. D. 2011, *ApJ*, **738**, 27
 Beck, T. L., Bary, J. S., & McGregor, P. J. 2010, *ApJ*, **722**, 1360
 Benedettini, M., Molinari, S., Baldeschi, A., et al. 2020, *A&A*, **633**, A147
 Biazzo, K., Beccari, G., De Marchi, G., & Panagia, N. 2019, *ApJ*, **875**, 51
 Bloemen, J. B. G. M., Caraveo, P. A., Hermsen, W., et al. 1984, *A&A*, **139**, 37
 Carr, J. S. 1989, *ApJ*, **345**, 522
 Carr, J. S. 1990, *AJ*, **100**, 1244
 Casali, M. M., & Eiroa, C. 1996, *A&A*, **306**, 427
 Claria, J. J. 1974, *AJ*, **79**, 1022
 Coccato, L., Freudling, W., Smette, A., et al. 2019, *Msngr*, **177**, 14
 Colombo, D., König, C., Urquhart, J. S., et al. 2021, *A&A*, **655**, L2
 Comeron, F., Torra, J., & Gomez, A. E. 1998, *A&A*, **330**, 975
 Connelley, M. S., & Greene, T. P. 2010, *AJ*, **140**, 1214
 Connelley, M. S., & Greene, T. P. 2014, *AJ*, **147**, 125
 Cooper, H. D. B., Lumsden, S. L., Oudmaijer, R. D., et al. 2013, *MNRAS*, **430**, 1125

- Cyganowski, C. J., Brogan, C. L., Hunter, T. R., Churchwell, E., & Zhang, Q. 2011, *ApJ*, **729**, 124
- Cyganowski, C. J., Whitney, B. A., Holden, E., et al. 2008, *AJ*, **136**, 2391
- Davies, R. I., Agudo Berbel, A., Wiezorrek, E., et al. 2013, *A&A*, **558**, A56
- Davis, C. J., & Eisloffel, J. 1995, *A&A*, **300**, 851
- De Marchi, G., Panagia, N., & Beccari, G. 2017, *ApJ*, **846**, 110
- De Marchi, G., Panagia, N., Romaniello, M., et al. 2011, *ApJ*, **740**, 11
- Djordjevic, J. O., Thompson, M. A., Urquhart, J. S., & Forbrich, J. 2019, *MNRAS*, **487**, 1057
- Elia, D., Molinari, S., Fukui, Y., et al. 2013, *ApJ*, **772**, 45
- Esteban, C., & García-Rojas, J. 2018, *MNRAS*, **478**, 2315
- Fernández-Martín, A., Pérez-Montero, E., Vílchez, J. M., & Mampaso, A. 2017, *A&A*, **597**, A84
- Fiorellino, E., Tychoniec, Ł., Manara, C. F., et al. 2022, *ApJL*, **937**, L9
- Fiorellino, E., Manara, C. F., Nisini, B., et al. 2021, *A&A*, **650**, A43
- Fischer, W. J., Padgett, D. L., Stapelfeldt, K. L., & Sewilo, M. 2016, *ApJ*, **827**, 96
- Frank, A., Ray, T. P., Cabrit, S., et al. 2014, in *Protostars and Planets VI*, ed. H. Beuther et al. (Tucson, AZ: Univ. Arizona Press), 451
- Furlan, E., Fischer, W. J., Ali, B., et al. 2016, *ApJS*, **224**, 5
- Glover, S. C. O., & Clark, P. C. 2012, *MNRAS*, **426**, 377
- Graczyk, D., Pietrzyński, G., Thompson, I. B., et al. 2014, *ApJ*, **780**, 59
- Green, G. M., Schlafly, E., Zucker, C., Speagle, J. S., & Finkbeiner, D. 2019, *ApJ*, **887**, 93
- Gullbring, E., Hartmann, L., Briceño, C., & Calvet, N. 1998, *ApJ*, **492**, 323
- Guo, Z., Lucas, P. W., Contreras Peña, C., et al. 2021, *MNRAS*, **504**, 830
- Hartmann, L., Herczeg, G., & Calvet, N. 2016, *ARA&A*, **54**, 135
- Hawkins, K. 2023, *MNRAS*, in press
- Herbst, W., & Assousa, G. E. 1977, *ApJ*, **217**, 473
- Heyer, M., & Dame, T. M. 2015, *ARA&A*, **53**, 583
- Hunter, J. D. 2007, *CSE*, **9**, 90
- Kaltcheva, N. T., & Hilditch, R. W. 2000, *MNRAS*, **312**, 753
- Karska, A., Kaufman, M. J., Kristensen, L. E., et al. 2018, *ApJS*, **235**, 30
- Kennicutt, R. C., & Evans, N. J. 2012, *ARA&A*, **50**, 531
- Kounkel, M., Megeath, S. T., Poteet, C. A., Fischer, W. J., & Hartmann, L. 2016, *ApJ*, **821**, 52
- Kraus, S., Hofmann, K. H., Benisty, M., et al. 2008, *A&A*, **489**, 1157
- Kristensen, L. E., Ravkilde, T. L., Field, D., Lemaire, J. L., & Pineau Des Forêts, G. 2007, *A&A*, **469**, 561
- Kristensen, L. E., van Dishoeck, E. F., Mottram, J. C., et al. 2017, *A&A*, **605**, A93
- Lépine, J. R. D., Cruz, P., Scarano, S. J., et al. 2011, *MNRAS*, **417**, 698
- Lin, Z., Sun, Y., Xu, Y., Yang, J., & Li, Y. 2021, *ApJS*, **252**, 20
- Lombardi, M., Alves, J., & Lada, C. J. 2011, *A&A*, **535**, A16
- Lorenzetti, D., Larionov, V. M., Giannini, T., et al. 2009, *ApJ*, **693**, 1056
- Luck, R. E., & Lambert, D. L. 2011, *AJ*, **142**, 136
- Luhman, K. L., & Rieke, G. H. 1998, *ApJ*, **497**, 354
- Maciel, W. J., & Andrievsky, S. 2019, arXiv:1906.01686
- Madden, S. C., Rémy-Ruyer, A., Galametz, M., et al. 2013, *PASP*, **125**, 600
- Mainzer, A., Grav, T., Bauer, J., et al. 2011, *ApJ*, **743**, 156
- Manara, C. F., Robberto, M., Da Rio, N., et al. 2012, *ApJ*, **755**, 154
- Meade, M., Whitney, B., & Babler, B. 2016, SMOG IRAC Data Description, v1.1, IPAC, https://irsa.ipac.caltech.edu/data/SPITZER/GLIMPSE/doc/smog_dataproduct_v1.1.pdf
- Molinari, S., Swinyard, B., Bally, J., et al. 2010, *A&A*, **518**, L100
- Mottram, J. C., van Dishoeck, E. F., Kristensen, L. E., et al. 2017, *A&A*, **600**, A99
- Muzerolle, J., Hartmann, L., & Calvet, N. 1998, *AJ*, **116**, 2965
- Natta, A., Testi, L., Muzerolle, J., et al. 2004, *A&A*, **424**, 603
- Nisini, B., Antonucci, S., Alcalá, J. M., et al. 2018, *A&A*, **609**, A87
- Nisini, B., Antonucci, S., Giannini, T., & Lorenzetti, D. 2005, *A&A*, **429**, 543
- Nisini, B., Santangelo, G., Giannini, T., et al. 2015, *ApJ*, **801**, 121
- Offner, S. S. R., Lee, E. J., Goodman, A. A., & Arce, H. 2011, *ApJ*, **743**, 91
- Oliphant, T. E. 2006, *A Guide to NumPy*, Vol. 1 (Austin, TX: Trelgol Publishing)
- Oliveira, J. M., van Loon, J. T., Sewilo, M., et al. 2019, *MNRAS*, **490**, 3909
- Olmi, L., Brand, J., & Elia, D. 2023, *MNRAS*, **518**, 1917
- Olmi, L., Cunningham, M., Elia, D., & Jones, P. 2016, *A&A*, **594**, A58
- Pietrzyński, G., Graczyk, D., Gieren, W., et al. 2013, *Natur*, **495**, 76
- Predehl, P., & Schmitt, J. H. M. M. 1995, *A&A*, **293**, 889
- Price-Whelan, A. M., Sipőcz, B. M., Günther, H. M., et al. 2018, *AJ*, **156**, 123
- Robberto, M., Soderblom, D. R., Scandariato, G., et al. 2010, *AJ*, **139**, 950
- Robitaille, T. P. 2017, *A&A*, **600**, A11
- Rolleston, W. R. J., Trundle, C., & Dufton, P. L. 2002, *A&A*, **396**, 53
- Roman-Duval, J., Gordon, K. D., Meixner, M., et al. 2014, *ApJ*, **797**, 86
- Roman-Duval, J., Jackson, J. M., Heyer, M., Rathborne, J., & Simon, R. 2010, *ApJ*, **723**, 492
- Russell, S. C., & Dopita, M. A. 1992, *ApJ*, **384**, 508
- Schisano, E., Rygl, K. L. J., Molinari, S., et al. 2014, *ApJ*, **791**, 27
- Sewilo, M., Whitney, B. A., Yung, B. H. K., et al. 2019, *ApJS*, **240**, 26
- Sharples, R., Bender, R., Agudo Berbel, A., et al. 2013, *Msngr*, **151**, 21
- Shevchenko, V. S., Ezhkova, O. V., Ibrahimov, M. A., van den Ancker, M. E., & Tjin A Dje, H. R. E. 1999, *MNRAS*, **310**, 210
- Skrutskie, M. F., Cutri, R. M., Stiening, R., et al. 2006, *AJ*, **131**, 1163
- Sodroski, T. J., Odegard, N., Arendt, R. G., et al. 1997, *ApJ*, **480**, 173
- Stanke, T., McCaughrean, M. J., & Zinnecker, H. 2002, *A&A*, **392**, 239
- Testi, L., Natta, A., Manara, C. F., et al. 2022, *A&A*, **663**, A98
- Tobin, J. J., Looney, L. W., Li, Z.-Y., et al. 2016, *ApJ*, **818**, 73
- van der Marel, N., Kristensen, L. E., Visser, R., et al. 2013, *A&A*, **556**, A76
- Van Der Walt, S., Colbert, S. C., & Varoquaux, G. 2011, *CSE*, **13**, 22
- van Kempen, T. A., Kristensen, L. E., Herczeg, G. J., et al. 2010, *A&A*, **518**, L121
- van Loon, J. T., Oliveira, J. M., Gordon, K. D., et al. 2010b, *AJ*, **139**, 68
- van Loon, J. T., Oliveira, J. M., Gordon, K. D., Sloan, G. C., & Engelbracht, C. W. 2010a, *AJ*, **139**, 1553
- Varricatt, W. P., Davis, C. J., Ramsay, S., & Todd, S. P. 2010, *MNRAS*, **404**, 661
- Visser, R., Kristensen, L. E., Bruderer, S., et al. 2012, *A&A*, **537**, A55
- Ward, J. L., Oliveira, J. M., van Loon, J. T., & Sewilo, M. 2016, *MNRAS*, **455**, 2345
- Ward, J. L., Oliveira, J. M., van Loon, J. T., & Sewilo, M. 2017, *MNRAS*, **464**, 1512
- Westerlund, B. E. 1997, *The Magellanic Clouds* (Cambridge: Cambridge University Press)
- Wolfire, M. G., Hollenbach, D., & McKee, C. F. 2010, *ApJ*, **716**, 1191
- Wright, E. L., Eisenhardt, P. R. M., Mainzer, A. K., et al. 2010, *AJ*, **140**, 1868
- Yoon, S.-Y., Herczeg, G. J., Lee, J.-E., et al. 2022, *ApJ*, **929**, 60